Nanophotonics in Diamond

Nanophotonics in Diamond

a dissertation presented
by
Birgit Judith Maria Hausmann
to
The School of Engineering and Applied Sciences

in partial fulfillment of the requirements
for the degree of
Doctor of Philosophy
in the subject of
Applied Physics

Harvard University
Cambridge, Massachusetts
May 2013

Thesis advisor: Marko Lončar Birgit Judith Maria Hausmann

Nanophotonics in Diamond

Abstract

Diamond nanophotonics have evolved tremendously from the study of color centers in bulk single crystals and nanocrystals to their characterization in nanostructured environments. This development was facilitated by the ability to generate monolithic, sophisticated nanodevices in high quality single crystal diamond. This thesis presents some recent contributions to the field of diamond nanophotonics: Increase in single photon collection from NV centers embedded in diamond nanowires, broadband spontaneous emission enhancement of single NV centers in plasmonic resonators, and coupling of single NV centers to planar resonators on-chip such as ring resonators and photonic crystal cavities.

In addition, the generation of high quality integrated diamond devices allows for the exploration of nonlinear processes in diamond. Here, we show for the first time optical parametric oscillations in diamond resonators.

Contents

1 Outline **1**

I First part: Diamond nanophotonics using color centers 4

2 Introduction **5**
- 2.1 Diamond and its color centers 5
- 2.2 Outline 18

3 Diamond fabrication and Implantation **20**
- 3.1 Materials and Methods 20
- 3.2 Results and discussion 24
- 3.3 Implantation 36

4 Diamond nanowires for improved collection efficiency of photons **42**
- 4.1 Design and Modeling 44
- 4.2 Conclusion and applications of diamond nanowires . . . 58

5 Enhanced NV center spontaneous emission in diamond-silver apertures **68**
- 5.1 Design and fabrication 70

5.2 Results 74

6 Coupling NV centers to integrated diamond ring resonators **90**
6.1 Diamond ring resonators as representative planar network 91

7 NV centers coupled to photonic crystal cavities **104**
7.1 Introduction to photonic crystal cavities 105
7.2 Photonic Crystal Design & Fabrication 109
7.3 Experimental 115
7.4 Tuning of cavity modes 118
7.5 Results: ZPL Enhancement 122
7.6 Conclusions and Outlook 124

II Second part: Integrated Nonlinear Optics in Diamond 127

8 The platform for nonlinear optics: Integrated diamond ring resonators **130**
8.1 Introduction to ring resonators and their design 131
8.2 Bare ring measurements using tapered fibers 137
8.3 Initial results of waveguide integrated ring and racetrack resonators 139
8.4 Split modes and nonlinear bistability signatures 143

9 Optical Parametric Oscillations **148**
9.1 Introduction 149
9.2 Design and fabrication of ring resonators 150
9.3 Results 156

III Third part: Le fin **167**

10 Summary and outlook **168**

References **174**

Meinen Eltern Marianne und Helmut gewidmet.

Acknowledgments

My time as a grad student was both challenging and scientifically enriching, but being in a group like Marko Lončar's helped me tremendously. Additionally, I particularly enjoyed the environment at a school like Harvard, meeting so many different people with all kinds of backgrounds, as well as being in Boston that offers so much to do and is located at the sea.

This dissertation would not exist were it not for my advisor Marko Lončar who has been an extraordinary mentor. Marko invested a lot of time in meeting and mentoring me, every time bursting with new ideas, while still providing me the freedom to try my own ideas and to collaborate with people. Furthermore, he had huge patience towards improving my writing skills and practicing talks for conferences. He has also allowed me to visit many conferences in great places which I am grateful for. Having seen you growing through tenure, along with all its challenges has been insightful. You also enjoyed teasing me a lot from the start, but I think I've finally reached your level fairly closely - I dare say as good as the master himself in the end. Marko, I'd like to gratefully thank you for being my mentor and my friend and I hope you can continue the group with as much enthusiasm for science as when you started the group.

Besides Marko, I had the fortunate luck of working and interacting

with a lot of other great professors at Harvard doing research with diamond. I'm deeply grateful towards Misha Lukin who took me in to his lab for experiments and mentorship. His scientific knowledge, insight and approach I found both intimidating and extraordinary, reaching beyond most physicists I have met. Unfortunately we didn't make it to strong coupling (yet) even though you promised us a visit to a beer garden in Munich, including the flight. I also enjoyed collaborating with Amir Yacoby and his diamond team, who are extremely friendly, mutually exchanging, and very helpful. Amir was always very trusting, and a great motivation. With Evelyn Hu I have not only enjoyed a great mentor while being a teaching fellow for her class, but also someone with whom I could openly speak about academic life and its challenges. Besides Evelyn, Marko, and Misha, I would also like to thank Ken Crozier for being part of my committee. Additionally I would like to thank Ron Walsworth, Isaac Silvera and Phil Hemmer for helpful discussions. Markus Greiner helped me and Marko initially with organizational and administrative challenges when I was starting as a diploma student. At the same time, I would also like to thank Jonathan Finley and Anna Fontcuberta i Morral for helping and advising my diploma thesis which eventually led to my Ph.D. work.

My stay in the group was enlightened and facilitated by the presence of fantastic postdocs and grad students. When starting in the group, Mughees Khan and Murray McCutcheon taught me how to do fabrication. Mughees, being wise and calm, has been guiding me with patience through the initial project of the nanowires and had to endure my initial trials of writing a paper. Murray was always pleasant to have around with his joyful and open presence and also very helpful with tapered fiber experiments later on. Irfan Bulu, who is always radiating with enthusiasm for science, has been the greatest influence for me, scientifically, and he with him I have a forged a

long-lasting friendship. His abilities in theoretical physics combined with his drive and support for our projects always buoyed us, especially in scientific drought times. More recently, I also had the pleasure to work with Vivek Venkataram, who is extremely knowledgable in nonlinear optics, life and philosophical questions. Working with Vivek has been most enjoyable and simply wonderful as he is counterbalancing my more impatient nature. I particularly admire his modesty and approachability in any questions, and he always invites discussions.

If I were asked to say who is a super friend with great scientific knowledge and one of the largest work ethics, I would respond with Jen Choy, who has always been supportive and helpful with all of the questions I have directed her way. I am extremely grateful that we got a chance to work especially closely together during the plasmonics project. We worked side by side all the time and I remember one of these rare extremely lucky and happy moments in science that we shared when we had a breakthrough in that project. Parag Deotare was a particularly good friend to me, like an elder brother. He has been very supportive in difficult times and has always had an open ear for questions with fabrication and experiments. I would also like to thank Tom Babinec who has an exceptional work ethic combined with a deep scientific understanding and with whom I worked on my first experimental project in the group.

Later, I was fortunate to work with Brendan Shields from the Lukin group on two projects. He taught me a lot about optics and NV centers in general. With him, I was lucky enough to share another of these rare moments in science when suddenly something starts to work, which is still so surprising even when one knows it has to. During the second challenging project, Brendan continued to be wonderful to work with. In the Lukin group, I also admire Yiwen Chu, who is one of these rare people I met at Harvard with extreme

knowledge and skill combined with a lively and life-loving nature despite spending so much time in the lab. I'd like to also acknowledge Nathalie de Leon who joined in and is continuing the difficult photonic crystal project with great scientific enthusiasm. She has also always helped me when I had scientific questions.

In the Lončar group, Yinan Zhang and Raji Shankar have also been great friends throughout grad school. Yinan has been both a helpful master in modeling as well as a distributor of wisdom, having a mind full of novel ideas and spreading so many laughters. Raji is also a distributor of unheard-of broad knowledge, often about things I never knew existed, words, anecdotes (also of the unknown words), politics and culture. Moreover she shared her secrets of great indian cuisine with us and was great company in the lab and office. Qimin Quan has been tremendously helpful with modeling but was also a charming and funny fellow in the office. Ian Burgess is not only scientifically great but also has a great nature of interacting with everyone on the same level without being judgmental. Moreover, I'd like to thank collaborators in the Yacoby group: Patrick Maletinsky, Mike Grinolds and Sungkun Hong. I truly enjoyed the friendly and fruitful interactions, their great knowledge and team spirit.

I would also like to acknowledge the cool kids of our lab, Michael Burek and Haig Atikian, the "knower of all truth", as well as Ian Frank. Additionally, I was glad to have had great office and lab mates like Khadijeh Bayat, Daniel Floyd, Dan Ramos, Wallace Hui, Young-Ik Sohn, Anna Shneidman, Srujan Meesala, Leonard Kogos and Julia Sokol. I would also like to thank the newer generation of students and postdocs.

I also enjoyed working and helpful discussions with Ruffin Evans, Alexander Kubanek with whom I also fancied sailing, Sasha Zibrov, Alexey Akimov and Orad Reshef. Furthermore, I'd like to thank Kristiaan de Greve, Mark Warner, Yuliya Dovzhenko and Lan Luan as

well as Jero Maze who helped us a lot during our overlap at Harvard.

During my Ph.D. I was fortunate to collaborate with a lot of groups inside and outside of Harvard. For instance, I enjoyed visiting the Stuttgart group of Prof. Joerg Wrachtrup where I also met Fedor Jelezko and Helmut Fedder who are all extraordinary scientists. Moreover I had the pleasure of interacting with Gopi Balasubramanian, Christoph Becher, Elke Neu as well as Chih-Hsun Hsu and Jeffrey Shainline from Jimmy Xu's lab at Brown University. In addition I appreciate the great interactions and scientific discussions with Daniel Twitchen and Matthew Markham from Element Six as well as Pete Morton form DDK.

At this point I'd like to also thank Kathy Masse, Xio Forbez and Hetchen Ehrenfeld for the support with any organizational questions. My Ph.D. would not have been possible were it not for the great facilities of CNS at Harvard and the constant great support by JD, Steve Paolini, Ling Xie, Yuan Lu, Noah Clay among others, whom I all would like to gratefully thank. I'd like to also thank Zac and Mike from FAS IT for great help with computers.

In addition I would like to thank those who became closer over time and were great friends without whom I would probably not have endured grad school. In particular, I enjoyed spending time with Jen, Raji, Yinan, Parag and Mikhail Kats. I was fortunate to have met a great friend in Anna Shneidman, whom I have met as a very honest, lovely and caring friend both in and out of the lab. I enjoyed going out and running with Julijana Gjorgjieva, Shanying Cui and Erika Janitz. In the last months I was fortunate to spend time with Susanne Mueller. At Harvard, the options of things to do are mind-blowing, hence I was lucky to play with the Dudley Orchestra and I'd like to thank Aaron Kuan and the flautists, especially Katherine Phillips. I took the best class ever with Ericka Knudson in French and would like to thank her for the great time and fun I had

while learning so much. Moreover, I'd like to thank Stephanie Young of the ceramics program for simply awesome classes in pottery.

I would also like to thank my loving and awesome friends at home, especially Nicole Stangl, Leo Gall, Lena Lendzian, Beatrice von Hagen, Meike Ballon, Raimund Strauss, Hubi Ceeh, Alex Baust, Jinming Lu, Claudi and Stephie Langenwalter and Eva Haberland who were always a great motivation. I'd like to thank them for constant Skype & call support, visits and many emails during the last years. Above all, I will never take for granted meinen Tuzi, Hund & Lion. Boy, I'm on a grand train!

More than anything, I'd like to thank my family for their help and support during my Ph.D. My parents Marianne and Helmut, as well as my sisters Christine and Monika, have always stood behind me in whatever I was pursuing with great joy and loving support while never pushing me in academic or career related decisions. Without their patience, visits and phone calls I would have not reached a Ph.D.

A Diamond is forever.

Frances Gerety

1 Outline

This thesis comprises two parts, the first part addresses diamond nanophotonics in the visible with Nitrogen Vacancy (NV) color centers while the second part covers the generation of parametric oscillations on chip at telecom wavelengths.

The first part is based in parts on reference [80] and is structured as

follows:

- Chapter 2 gives an overview on the NV center and diamond in general.
- Fabrication techniques are presented in chapter 3 along with material considerations [72, 80]. Techniques that were developed during my time as diploma student are reviewed.
- In chapter 4 work on diamond nanowires during my diploma thesis is reviewed, which was continued and extended during my Ph.D. Especially, the fabrication in this thesis builds upon these early developments. This chapter gives an overview of our diamond nanowire publications [11, 72, 73, 80].
- The broadband spontaneous emission enhancement of the NV center's decay rate in a plasmonic resonator is considered in chapter 5 which has been published with minor changes in [38].
- Chapter 6 introduces a planar diamond platform on insulator, which is exemplified in the integration of NV centers in diamond ring resonators along with the on-chip routing of their single photons. This chapter has been published with some changes in [76].
- Building upon the single crystal diamond on insulator (DOI) platform, the coupling and enhancement of single NV centers

coupled to suspended photon crystal cavities are demonstrated in chapter 7. This chapter has been published (in this corrected version of the thesis) in [77].

The second part presents nonlinear optics in diamond ring resonators and is organized as follows:

- In chapter 8 waveguide integrated ring resonators as device of choice are introduced. Most of this chapter has been published in [79].
- Results on parametric oscillations are presented in chapter 9. A publication based on this chapter has been accepted to Nature Photonics at the state of the corrected version of the thesis [78]

The thesis ends with a conclusion and outlook in chapter 10.

Part I

First part: Diamond nanophotonics using color centers

Il n'y a réellement ni beau style, ni beau dessin, ni belle couleur : il n'y a qu'une seule beauté, celle de la vérité qui se révèle.

Auguste Rodin

2

Introduction

2.1 Diamond and its color centers

Researchers have long been attracted to diamond for its many unique properties. For example, diamond's large refractive index (n=2.4) and the presence of color centers, such as the silicon vacancy (SiV) [173]

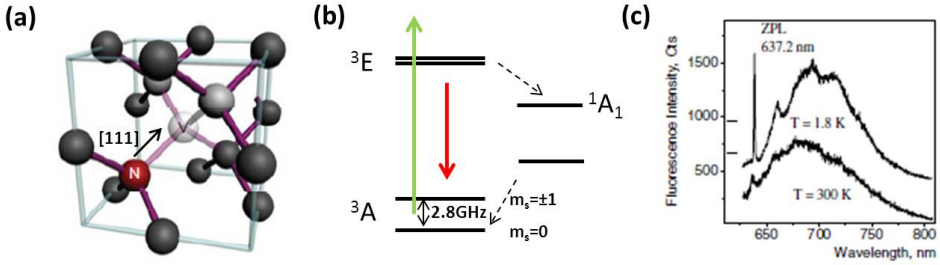

Figure 1: **(a)** Schematic of an NV center in the diamond carbon lattice. **(b)** Electronic level scheme of the negatively charged NV center, and **(c)** spectra of the NV center emission both at room and low temperature. Figures **(a), (c)** with courtesy of [14] [87].

and nitrogen vacancy (NV) centers [20, 101, 186], that can be addressed individually using optical excitations, are of particular interest to the field of quantum optics and photonics. Other light-emitting defects in diamond based on Carbon [127], Nickel [64], and Chromium [2] impurities have also been shown to generate non-classical states of light and emit single photons at room temperature, which is a critical resource for quantum optical communication systems. Efforts to identify other outstanding color centers in diamond are on-going [178]. Notably, the negatively charged NV center has been in the focus of diamond photonics research for more than 50 years [186] as a promising platform for the realization of robust, room temperature, single-photon sources. Due to its stability, long electron-spin coherence time, and optical read-out capabilities as well as its possible formation via ion implantation, it is among the most appealing color centers in diamond. The NV center is

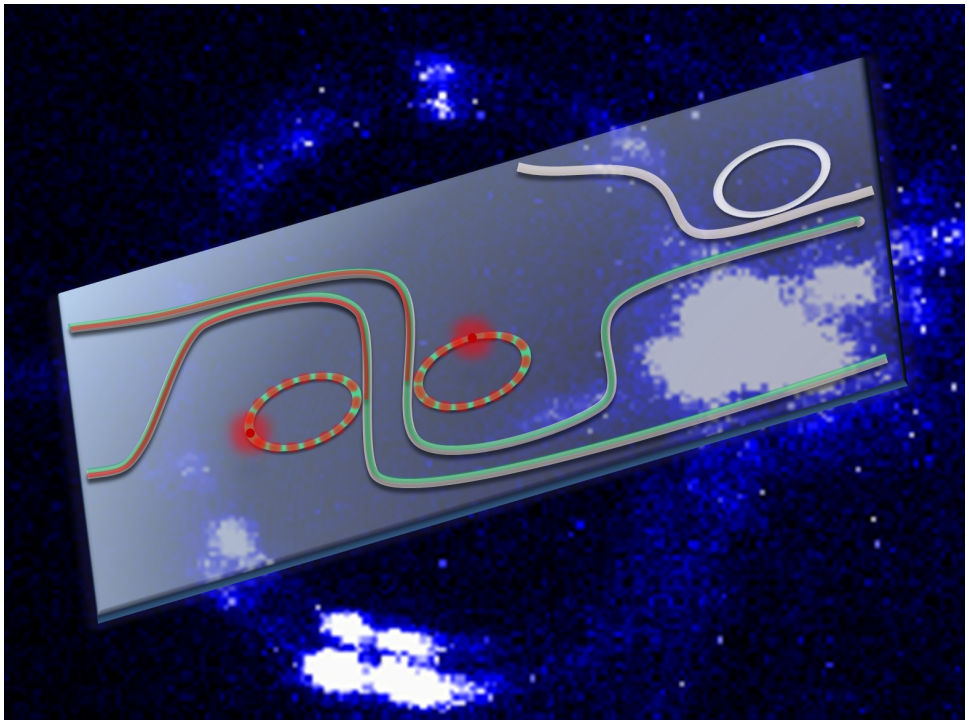

Figure 2: Cartoon of diamond integrated devices on chip containing NV centers which are discussed in chapter 6.

formed by replacing one carbon atom in the diamond lattice by a nitrogen atom, and removing one adjacent carbon atom such that the NV center's axis is along the [111] direction (Fig. 1a). It can exist in two charge states, NV^0 and NV^- out of which the NV^- center is suitable for quantum operations due to the electron's spin kinetics. NV centers can be introduced either during the diamond's growth or after the diamond has formed, using ion implantation. The electronic levels of the negatively charged NV center, sketched in Fig. 1b, consist of triplet ground (^3A) and excited (^3E) states that are separated by 1.95 eV corresponding to 637 nm. The triplet ground

state of the NV center is split due to spin-spin coupling effects by 2.87 GHz between the $m_s = 0$ and $m_s = \pm 1$ states [69]. A selective coupling between the excited states and the long-lived metastable singlet state ($^1A_1$), dependent on the initial ground state population, enables state-dependent fluorescence and spin-readout. The NV center's emission spectrum can be obtained using green excitation and consists of a zero-phonon line (ZPL) at 637 nm, a pure photon transition, and a broad phonon sideband (PSB) from 637 nm to around 800 nm that originates from phonon-assisted transitions. The electron-phonon coupling for an NV center is strong so that most of the spontaneous emission occurs into the PSB. Fig. 1c shows the NV center's spectrum in a bulk diamond both at room and low temperature. At low temperature, the phonon-assisted transitions around the ZPL are suppressed and the ZPL becomes much more visible. The ZPL emission can be further increased using optical resonators as discussed below.

For applications in quantum information science and technology, diamond offers unique advantages over other solid-state platforms. The NV center in particular, as a stable single photon source, that can be used as a long-lived (spin-based) memory with optical read-out via its optically-detected magnetic resonance, is very attractive for applications [88] in magnetometry [13, 121] and quantum information science and technology [37, 50, 129, 132, 181]. For instance, NV

centers coupled to a resonator could form a quantum node of a quantum network to store, manipulate and process information while waveguides could represent quantum channels between the nodes that transfer quantum information [93, 132]. While proof-of-principle quantum networks with diamond NV centers have previously been demonstrated [21, 36], the scalability of the approach crucially depends on the realization of an integrated diamond nanophotonic platform (Fig. 2).

Until recently scalable diamond photonics has been limited to bulk [3, 11, 17, 38, 70, 160] or polycrystalline diamond devices [82, 176, 177] due to difficulties associated with the fabrication of thin, single crystal, diamond (SCD) films on sacrificial or low index substrates. Light absorption and scattering at grain boundaries can be detrimental for the polycrystalline diamond approaches, while the realization of scalable, on-chip quantum networks is challenging with single-crystal bulk diamond approaches.

These and other applications, however, depend crucially on the efficiency with which information can be exchanged between the NV center's electron spin (a stationary qubit in the context of quantum computation) and a photon (a "flying" qubit). Therefore, there has been great interest in increasing the photon - NV center interaction using diamond - based optical nanostructures. While quantum science and technology has been the main driving force behind recent interest

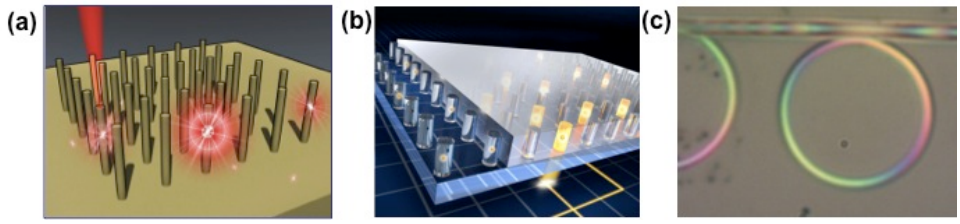

Figure 3: Schematics of diamond devices discussed in this thesis. **(a)** Diamond nanowires containing single NV centers that provide a high capture of single photon flux. **(b)** Diamond silver apertures offer Purcell enhancement of the NV center's emission. In a dream quantum network, these silver-capped nanoposts can be envisioned as individual nodes that communicate via single photons that are routed either on- or off-chip. **(c)** Integrated diamond devices such as ring resonators (shown here coupled to an optical fiber) as well as photonic crystal cavities (not shown).

in diamond nanophotonics, such a platform would have many applications that go well beyond the quantum realm. For example, diamond's transparency over a wide wavelength range and large third-order nonlinearity are of great interest for the implementation of frequency combs. Furthermore, diamond's wide bandgap (5.5 eV), very large phonon energy (165 meV compared to 65 meV in Si), and excellent thermal properties are suitable for integrated, high-power Raman lasers [46, 125].

2.1.1 Challenges in diamond fabrication and material synthesis

Recent accomplishments in diamond nanodevices Due to difficulties associated with the fabrication of nanoscale optical devices

in diamond, early approaches to enhance the NV center-photon interaction had mostly relied on hybrid platforms that couple diamond nanocrystals [20] or nano pillars to evanescent or confined optical fields produced by dielectric [16, 53, 103, 136, 152, 171] or metallic [35, 85, 154, 155] nanostructures. However, the optical and spin properties of single NV centers found in nanocrystals tend to be inferior to those in bulk diamond and device fabrication lacks scalability. In particular, severe spectral diffusion of the ZPL and its broad linewidths, even at low temperature [180], have limited the applications of diamond nanocrystals. Another bottleneck in many of these techniques is the deterministic coupling of single quantum emitters to photonic elements, which is typically challenging and incompatible with large-scale production of devices. For instance, bottom - up approaches involving diamond nanocrystals have mostly relied on random (drop/spin-casting) or alignment - sensitive (pick-and-place by an AFM tip) techniques of positioning diamond nanocrystals to achieve emitter-optical field coupling, resulting in one-of-a-kind devices.

An enticing approach is to realize optical devices directly in diamond and embed individual color centers inside them. However, the realization of such a monolithic system is met with a set of material challenges, namely the difficulty of growing high-quality single crystal diamond films on sacrificial or low index substrates, and

the physical and chemical resilience of the material. Ion slicing [134] has been used to realize thin diamond slabs, but damage introduced into the diamond during the process has prevented applications in quantum science. However, recent techniques based on the regrowth of single crystalline material on sliced membranes [4], [114] showed promising results. An alternative technique used to sculpt optical devices directly in diamond is based on focused ion-beam (FIB) milling [10] [156], [18][12]. Despite the versatility of the method, however, the resulting devices are prone to damage due to the implantation of gallium ions. Furthermore, the devices are one of a kind and the fabrication process is slow. Therefore, the approach is likely not suitable for the realization of nanoscale optical devices and their large scale integration. The exception are devices in which the NV center is located far away from the processed surface, such as solid-immersion lenses (SILs) [70, 156, 160], or post-processing techniques are used to minimize the damage due to ion bombardment [146].

Recent advances in conventional top-down fabrication techniques now allow for three-dimensional [72], [11] and planar [55], [76], [56], [146] nanoscale diamond structures to be made with scalability and high yield. This approach involves the patterning of an etch mask using electron beam lithography (EBL) and subsequent reactive-ion etching (RIE) of diamond material in an oxygen-based environment

[72]. Thousands of devices can be realized in parallel this way, which suggests that the procedure can eventually enable the construction of chip-scale quantum networks. Additionally, the latter approach of dry etching diamond can be used in conjunction with ion implantation to provide deterministic positioning of color centers in nanophotonic devices [73].

Material considerations Device throughput is an important consideration for diamond nanofabrication and greatly depends on the density and distribution of NV centers in the diamond substrate. In type Ib diamond (Element six, < 200 ppm N content), the NV center density is quite high, but varies from chip to chip as well as within the chip. In type IIa mechanical grade CVD diamonds (Element six, < 1 ppm N content), the NV center density is usually too high for single NV centers to be resolved, while the density of NV centers in ultrapure electronic grade CVD diamond (Element six, < 5 ppb N content) is very low to the extent that sometimes no NV centers are found close to the surface in a whole chip. However, when found, these NV centers are of high quality and can have ZPL linewidths down to ~ 20 MHz in resonant absorption [181]. In mechanical grade IIa CVD NV centers have shown to have ZPLs as narrow as 4 GHz [56] in a nanodevice. Nonetheless, the randomness in the density and position of natural NV centers makes their integration in optical devices challenging when precise positioning at a mode maximum is required.

Hence, there has been interest in engineering the spatial distribution of single color centers in diamond via ion implantation on a large scale. Techniques based on blanket electron irradiation or ion implantation at different dosages [69, 143], focused ion implantation [123], and implantation through nanoscale apertures [124, 167] have all been demonstrated to generate single color centers in a bulk crystal. Implantation of Nitrogen ions (usually ^{15}N to distinguish from naturally occurring ^{14}N via the hyperfine splitting signature [87]) offers some control over the depth of NV centers (to the accuracy of the ion straggle) in the crystal by way of the ion energy. The ion dosage and annealing conditions can further increase the probability of proper integration of NV centers to devices by providing some degree of density control and will be discussed in chapter 3.3. Future scalable quantum technologies will benefit from complete fabrication routines that combine diamond photonic device engineering with ion implantation of color centers at the single defect level.

2.1.2 NV-Photon interaction inside an optical cavity

Due to the strong electron phonon coupling that leads to a prominent PSB emission, only $\sim 5\%$ of the overall radiative NV emission goes into the ZPL. This limits the ZPL photon rate to $\sim 1,000$ counts per second (CPS), in a typical confocal microscope, which in turns significantly limits the applications in quantum science and

technology that rely on high rates of indistinguishable photons (e.g. realization of quantum repeaters). This situation can be significantly improved by embedding NV centers inside optical devices which fall in one of the two categories:

(A) Non-resonant geometries, like diamond nanowires [72], [11] and solid immersion lenses [70], that overcome total internal reflection (TIR) at the diamond-air interface can be used to significantly improve the photon collection efficiency without affecting the radiative emission rate of the NV center.

(B) Resonant optical structures, both dielectric and metallic [38], can be used to increase the emission rate of the NV center via the Purcell effect [140]. Some quantum cryptography schemes rely merely on the single photon rate where plasmonic resonators provide an attractive approach [6, 29, 51, 99, 115, 147]. Here, sub-wavelength confinement of optical fields can strongly modify the spontaneous emission of a suitably embedded dipole despite possessing only modest quality factors. Meanwhile, the scalability of solid-state quantum systems critically depends on the ability to control such emitter-cavity interaction in a number of devices in parallel. For other applications in quantum science and technology, high-quality factor optical resonators with sharp optical resonances are of particular interest: when their resonance is matched to the NV center's ZPL, selective

enhancement of the ZPL emission over the PSB emission can be achieved. In this case, optical resonators on-chip such as ring resonators or PCCs are of particular interest.

The Photon-NV center interaction can be described in terms of the coupling rate g between the emitter and the cavity field, the cavity decay rate κ and the spontaneous emission rate γ. Depending on the relative magnitude of these rates, two different regimes are possible: i) the weak coupling regime, characterized by $g^2 > \kappa \cdot \gamma$, and ii) the strong coupling regime, where $g >> \kappa, \gamma$. The weak coupling regime (Purcell regime) is of interest in applications that depend on a large number of ZPL-single photons, including single photon transistor/photon blockade experiments [32] [22], various interference and entanglement scenarios [23] [129] [166][137], or efficient read-out from quantum registers [50] [131]. In this limit, the Purcell factor, F_P, is often used as a figure of merit for the degree of spontaneous emission rate enhancement. For an emitter placed at the cavity's field maximum with optimum polarization, F_P is defined as

$$F_P = \frac{g^2}{\gamma\kappa} = \frac{3}{4\pi^2}\left(\frac{\lambda}{n}\right)^3 \frac{Q}{V} > 1 \tag{2.1}$$

where Q is the quality (Q) factor and V the mode volume of the resonator. The Q-factor describes the resonator's ability to store photons, whereas V represents the mode volume in the dielectric

material. For an NV center, where a maximum 5% of light is emitted into the ZPL, a Purcell factor of 20 results in equal emission rates into the ZPL and the PSB. In addition, the ZPL is usually not lifetime-limited and is broadened by charge fluctuations around the NV center. A Purcell factor exceeding 20 might counteract this effect in the case where the cavity linewidth is broader than the ZPL. To enter the weak coupling regime a Q-factor on the order of 10^3 is needed for a mode volume of $1 \cdot (\lambda/n_{diam})^3$, as can be achieved with photonic crystal cavities (PCCs), having an optimum NV axis orientation with respect to the mode polarization and mode overlap. These effects put stringent requirements on the quality of optical cavities made in diamond when compared to other material systems. For example, compared to quantum dot-cavity systems [172], a NV center-diamond cavity system needs to have up to two orders of magnitude larger cavity Q-factor to achieve a comparable Purcell factor. This, combined with immature fabrication techniques for diamond, makes the realization of quantum optical devices based on diamond very challenging.

In the strong coupling limit, coherent exchange of energy between the NV center and the cavity field exists, and the system undergoes Rabi oscillations between the split dressed states [49]. Strong coupling could enable a full spectral control of the NV center's ZPL emission, as well as extraction of emitted photons into a well defined cavity/

waveguide mode. Furthermore, this limit of light-matter interaction is of interest for deterministic, on-demand, single photon sources [122]. While these oscillations have been observed with other solid-state systems [145], this regime of operation is challenging to achieve with NV centers (where a Q-factor on the order of 10^5 is needed) due to the lack of high-Q all-diamond optical resonators, as well as stable NV centers embedded inside optical nanostructures.

2.2 Outline

In this thesis, efforts to realize non-resonant diamond structures, as well as resonant structures in the weakly-coupled limit are described in part I. First, single NV centers coupled to a waveguide mode of a diamond nanowire are demonstrated as a high-collection efficiency platform (Fig. 3a). The second geometry considered consists of a diamond nanopost embedded in silver. This nanocavity takes advantage of the ultra-small mode volume typical of metallic nanodevices in ordered arrays to increase the radiative emission rate (Fig. 3b) over wide wavelength range. The third device described consists of a ring resonator coupled to an optical waveguide (Fig. 3c) - a building block for future on-chip quantum networks. On-chip single-photon routing using this device is discussed as well. Finally, the coupling of single NV centers to suspended PCCs is discussed. A Purcell enhancement of the NV center's ZPL is inferred when tuning

the cavity mode over the ZPL in low temperature measurements.

Part II covers nonlinear optical processes in fully integrated SCD diamond ring resonators on a low index substrate. The strong interaction of light with the diamond material due to the resonator's high Q factors allow for the exploration of optical parametric oscillations based on diamond's $X^{(3)}$ response.

Un art qui a de la vie ne reproduit pas le passé ;

il le continue.

Auguste Rodin

3

Diamond fabrication and Implantation

3.1 Materials and Methods

We used two types of diamond samples based on their crystalline nature: a) poly-D films and b) type Ib and IIa single crystal

diamonds(SCD) synthesized via HPHT and CVD processes respectively. While SCDs are needed to realize single-photon sources, poly-D films have been used to identify highly resistive etch masks and to optimize etch recipes and other processes due to their low-cost and availability in large quantities.

The poly-D samples were diamond on insulator (DOI) AQUA 25 wafers ($2\,\mu$m poly-D film on $1\,\mu$m thermal SiO_2 on a Si substrate) from Advanced Diamond Technologies, Inc. The nitrogen rich HPHT Ib and two different types of CVD IIa SCDs (low and high Nitrogen content $[N] < 1\,$ppm, $[N] < 5\,$ppb respectively) were obtained from Element Six (E6) or occasionally CVD SCD from Apollo Diamond. SCD samples had unless noted otherwise a <100> crystal orientation (and occasionally <111> orientation). Prior to mask deposition the SCD samples were cleaned for about 45 min in a boiling 1:1:1 (Nitric : Perchloric : Sulfuric) acid bath. This aggressive etch was not used with the poly-D samples as it appeared to damage the DOI film.

Three different routes in etch mask definition were pursued as illustrated for the exemplified fabrication of nanowires in Fig. 16.

(A) Nanoparticle mask, deposited via drop-casting: In this approach drop cast nanoparticles have been used as an etch mask. Au and SiO_2 colloids suspended in DI water as well as Al_2O_3 powder with different sizes were used. While the method is least time

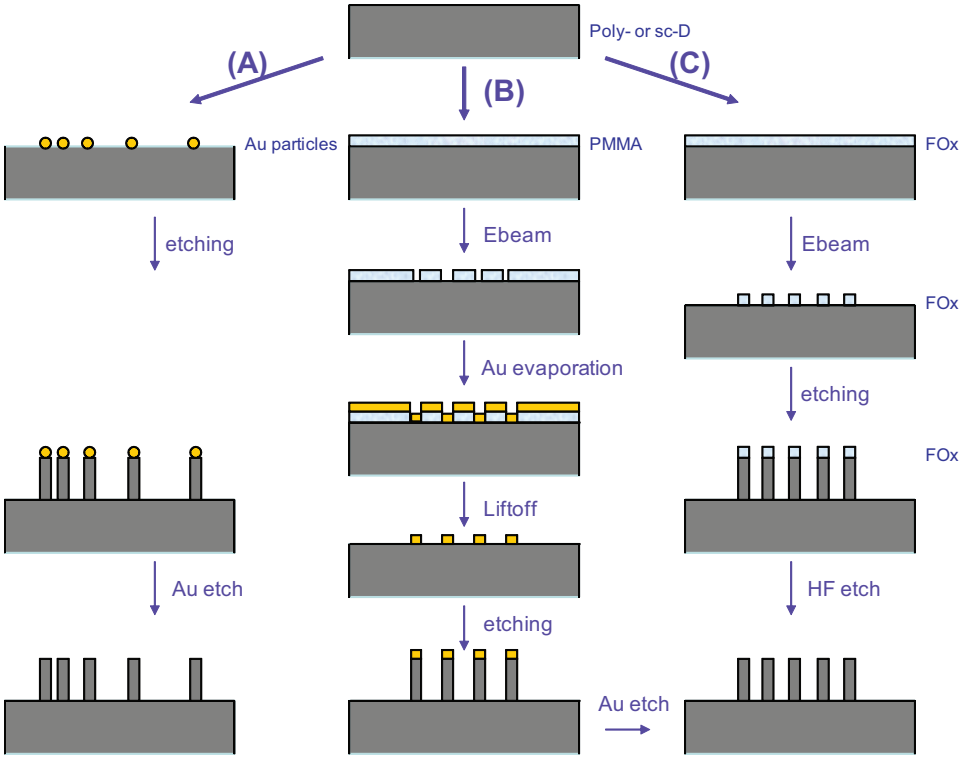

Figure 4: Fabrication process schematic. (A): Drop casting of nanoparticles (Al_2O_3, Au, SiO_2) followed by etching. (B) EBL defined metal/ceramic evaporation or sputtering respectively. (C) EBL defined FOx mask (flowable oxide, a spin-on-glass resist).

consuming, it results in randomly distributed wires, the particle sizes differ within each suspension within statistical errors and the distribution of wires is not completely uniform across a chip.

(B) Au, Cr or Al_2O_3 mask defined via a lift-off process: In this approach, evaporated metal or sputtered alumina was used as an etch mask. A pattern was defined in EBL using bilayer PMMA from MicroChem Corp in 100 kV or 125 kV Elionix e-beam tools. Dosages were varied from 800 μC/cm^2 to 1600 μC/cm^2. Next, for example, 10 nm Cr and 200 nm Au evaporation followed by a lift-off process was used to define a metal etch mask.

(C) Spin-on-glass (HSQ) mask defined by EBL: XR e-beam (Dow Corning) resist was first spun having a better adhesion to diamond and flowable oxide (FOx 17, Dow Corning) was diluted with MIBK in 1:2 or 1:1 ratios and spun as second layer for longer etch processes. Dosages from 4800 μC/cm^2 to 8000 μC/cm^2 were used to expose FOx resist in the case of nanowires with diameters up to 250 nm. For larger surface area devices the dosage required is much lower.

An ICP RIE system (UNAXIS shuttleline) was used to transfer the mask pattern into diamond. An etch recipe having 30 sccm oxygen flow rate, 100 W Bias power, 700 W ICP power at a 10 mTorr chamber pressure was used, hereafter referred to as "basic recipe". After RIE,

the mask was removed in gold (type TFA, Transene) and /or chrome etchant (type 1020, Transene) or an HF (49%, aq) wet etch was performed to remove the remaining FOx or alumina mask followed by another acid bath treatment. For implanted samples, several post-processing procedures such as high temperature annealing, cleaning and an anneal in a rapid thermal processor (RTP) was performed in oxygen environment at 465 °C.

3.2 Results and discussion

3.2.1 Basic top-down device fabrication for nanowires and -posts

The etch recipe was optimized (starting with poly-D material) to obtain a vertical wire profile. Details on the results on variations of the etch recipe can be found in [72]. Different mask materials, including metals like Au and Cr, ceramics like Al_2O_3, and different forms of silica were also evaluated. We found that spin-on-glass HSQ resist provides both a high etch resistivity and very smooth sidewalls. Although the resist handling (quick degradation of resist over time and low adhesion on top of diamond) is challenging and the repeatability is poor compared to other standard EBL resists, it provides highly smooth sidewalls [72]. The optical device performance depends critically on the smoothness of sidewalls to avoid scattering

of light and hence a loss channel. The optimized etch recipe seems to not add further deterioration (which has yet to be confirmed by AFM); the etching seems to transfer the level of resist smoothness into the film. For some devices like ring resonators, we found that we are limited by how the EBL writes the pattern (see details in section 9.2). For the fabrication of nanowires a quick way to obtain randomly distributed nanowires without the necessity of EBL is dispersing nano particles on substrates (Fig. 5a) according to method A. This process can be useful for bio-applications, where the non-toxicity of diamond comes in handy for tests of luminescent markers in fruitflys for example. Here, a very high yield (100 millions of devices) of nanowires is required, which also needs to be transferred from the substrate to the fruit fly food. A collaboration with Christelle Prinz in Lund University is being pursued in this direction.

For ease in characterization it is desirable to use EBL and create ordered arrays of nanowires (or any devices). A longer run of the basic recipe resulted in a cone-shaped profile of wires (Fig. 6). Verticality in sidewalls was achieved for a process where the recipe was varied in time: The basic recipe was used for 2 min, the ICP power was decreased to 600 W for 3 min and then ramped up to 1000 W for 5 min. We were able to realize large arrays of 2 μm tall nanowires with near vertical profile (Fig. 7a and 21) as well as 4.3 μm tall wires with a 4-step recipe (Fig. 7b). Etch rates in different types of diamonds

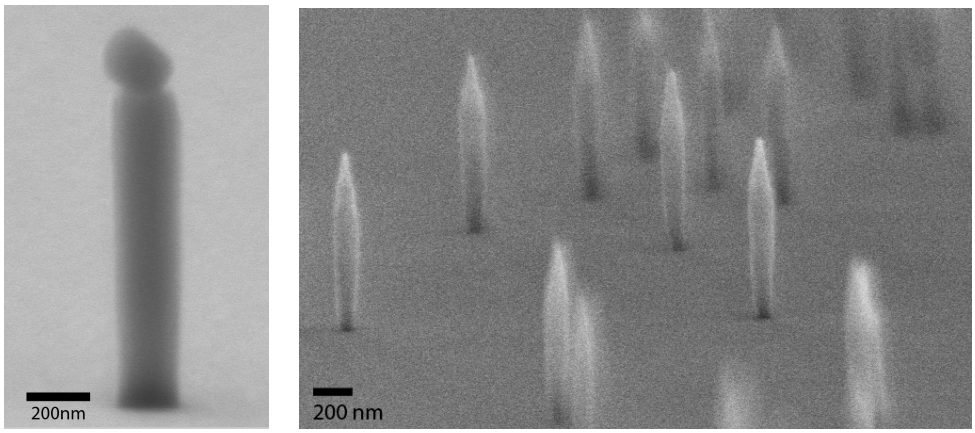

Figure 5: Poly-D nanowires after a $5\,\mathrm{min}$ oxygen etch. (a) Al_2O_3 powder as mask ($\approx 200\,\mathrm{nm}$ in diameter) [72]. (b) Au colloids as mask $100\,\mathrm{nm}$-Au.

were found to be similar [76]. Even if mask erosion occurs and the nanowire has a tapered profile it will not deteriorate the nanowire's performance, but can be beneficial for a high extraction efficiency of single photons emitted from NV centers embedded within nanowires [61]. Tiny diamond posts were also fabricated in a short RIE run as discussed in the section on plasmonic resonators 5.2.

3.2.2 Planar device fabrication

The method presented here was developed together with our collaborators from the Yacoby group [116].The advantages of this approach lie in the high crystal quality that can be maintained for the optical devices. We note, however, that the handling of such thin

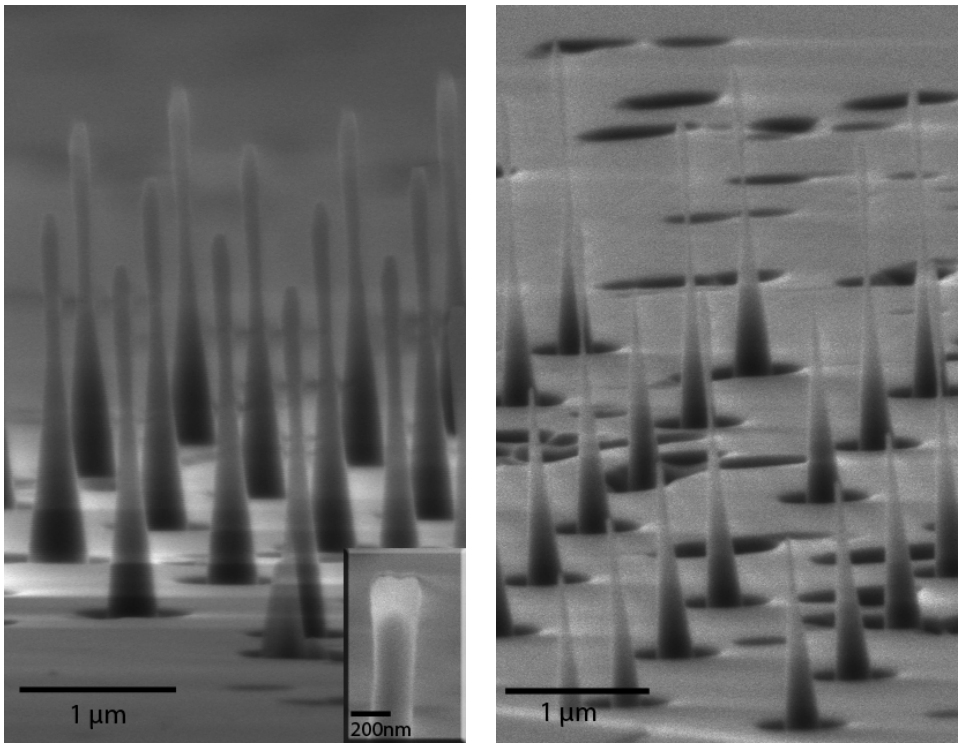

(a) **(b)**

Figure 6: SCD wires formed in a Ib HPHT diamond. FOx was used to produce an array of pillar-shaped mask with EBL. The mask was then transfered to the substrate during a $10\,\mathrm{min}$ oxygen etch and subsequently removed. The height of the wires is $2.3\,\mu\mathrm{m}$. **(a)** The diameters at the broadest part of the top and the bottom are $\approx 110\,\mathrm{nm}$ and $\approx 310\,\mathrm{nm}$ respectively. At the thinnest part of the wires the diameter is $\approx 70\,\mathrm{nm}$. Inset: One wire with the remaining FOx mask after etching (different diameter). **(b)** One array of nanowires with a bottom diameter of $226\,\mathrm{nm}$.

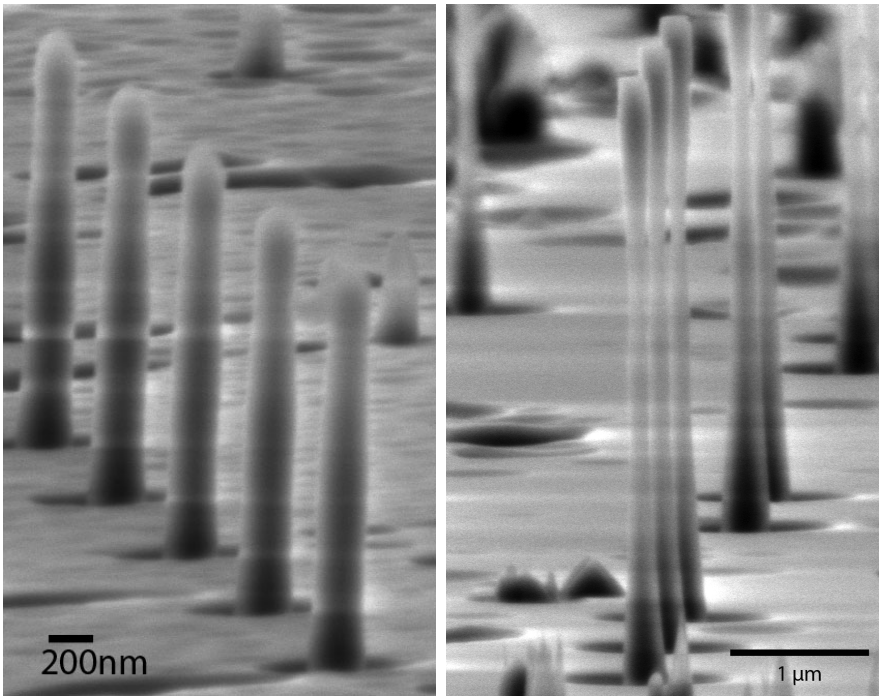

Figure 7: (a) Nearly vertical sidewalls were achieved for these $2\,\mu\mathrm{m}$ high SCD (Ib HPHT) wires after a $10\,\mathrm{min}$ oxygen etch. The diameter at the bottom is $\approx 260\,\mathrm{nm}$. **(b)** SEM image of an array of nanowires of height $4.3\,\mu\mathrm{m}$ after a 4-step etch recipe was applied

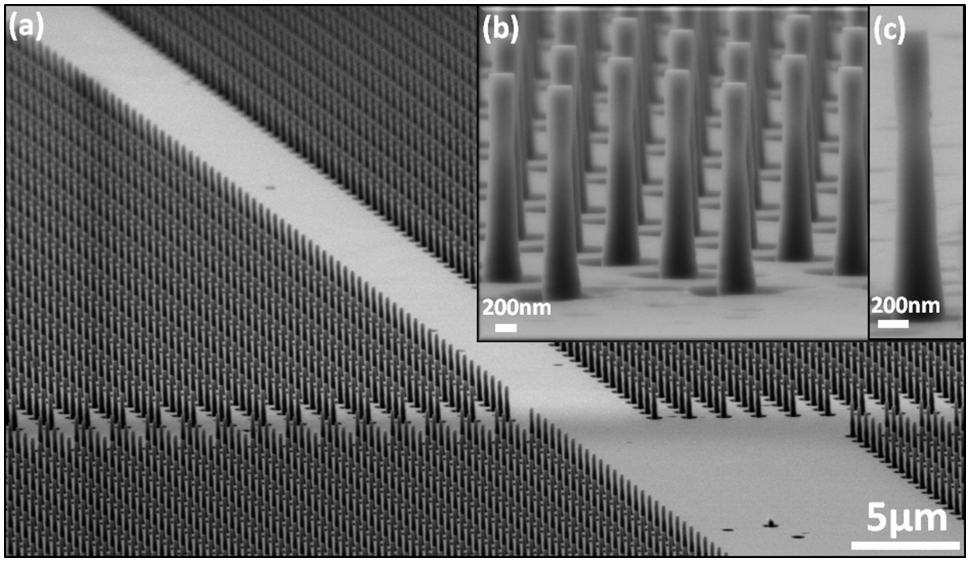

Figure 8: (a) SEM image of an array of nanowires of height $2\,\mu\mathrm{m}$ and diameter $200\,\mathrm{nm}$. Thousands of devices can be realized in parallel due to high-throughput nanofabrication techniques that were used. **(b-c)** Higher magnification images of nanowire arrays.

diamond substrates ($< 1\,\mu$m thickness), as well as wedging of the diamond films, can be detrimental in the fabrication process.

Planar device fabrication requires a thin diamond film on a substrate and for optical needs, a low-index substrate like silica on silicon. As mentioned before, growing thin films of diamond on a different substrate results in polycrystalline diamond which has not yet been shown to comply with single photon operation. The lattice constant mismatch between diamond and most substrates is significant, hence the polycrystallinity. However, one approach comprises the growth of a thin diamond film on cubic boron nitride (cBN) on diamond, which has a similar refractive index of 2.1 and

lattice constant. The growth of cBN on diamond has been demonstrated [187]. In addition, sputtered films of cBN on diamond tend to come off the substrate in an acid bath [118].

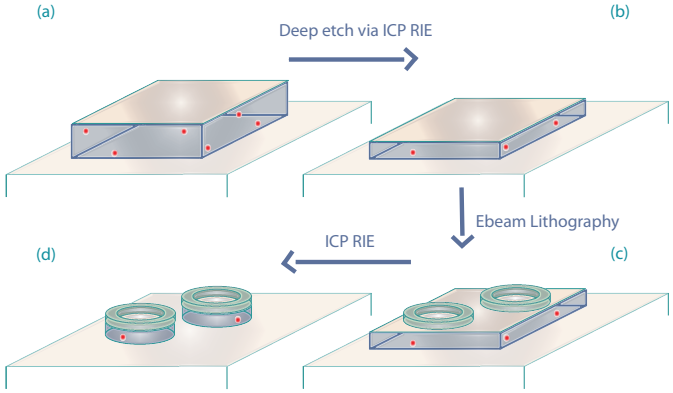

Figure 9: Fabrication schematic used to make ring resonators is as follows: First, we thin a diamond slab via an oxygen based reactive ion etch (RIE). Next we use e-beam lithography to define a the devices in e-beam resist. Finally we transfer the mask into the thinned diamond slab using RIE. Residual resist is not removed from devices during characterization. Optically active defect centers are indicated in red.

Here, our approach involves the fabrication of high quality, low loss diamond devices directly in SCD thin slabs. Figure 9, illustrates our fabrication sequence exemplified on ring resonators, based on the approach that we [74, 111, 116] as well as others [55] have demonstrated. First we thin a $10-50\,\mu$m thick type Ib or IIa single crystal diamond slab (Element Six) to the preferred device layer thickness by an oxygen-based ICP RIE [116]. Figure 10 shows a partly masked diamond thin film (with a quartz plate) after several μm have been etched. The deep etching leaves sidewalls at the edges

of the diamond film behind (Fig. 11) which need to be removed in acid cleaning or sonication bath if the film thickness is $\geq 3\,\mu$m. Etching has to be performed on both sides of the diamond to remove at least $2\,\mu$m of diamond material on the surface that can have stress/strain from the polishing process otherwise the film might bend (Fig. 12a, b).

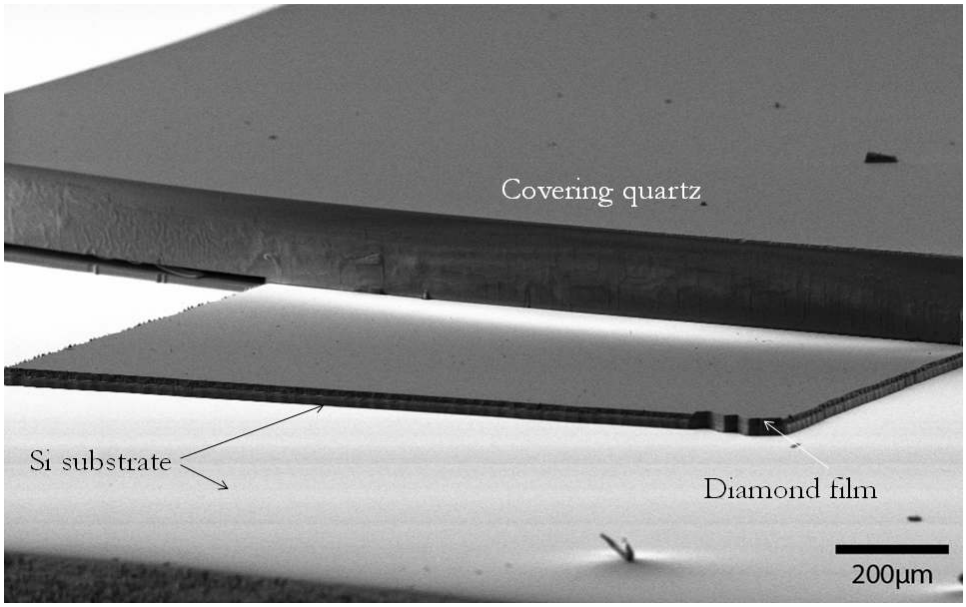

Figure 10: Depending on the sample size, quartz was used to mask off part of the diamond plate prior etching. Si or silica substrates have been used for deep etching. Remarkably, the etch recipe etches Si substrates with decent rates of $> 12\,\mu\mathrm{m/cycle}$ as well. For silica substrates an etch rate of $150\,\mathrm{nm/min}$ has been inferred for the oxygen etch step only.

The thinning process requires a truly clean surface as residual dirt on the substrate results in "dimples" that will lead to holes in the thin film (Fig. 13). Most likely, residual dirt acts as a mask for nanowires,

that form trenches surrounding the nanowire base during the etch process. At some point during the etch, the wire etches through from the side when it has a bowling pin shape or gets etched away when the film is very thin (Fig. 12c). For that reason it is also crucial that the etch chamber is clean. Since numerous materials are etched or used as a mask in our ICP RIE chamber, the chamber sidewalls get coated with etch residues after some time. The long etch times in deep etching causes the chamber to heat up and etch residues deposited at the chamber sidewalls tend to come off more easily. Furthermore, dimple formation can also arise from polishing defects often present in the surface of as - purchased diamond. After thorough cleaning (acid and solvent clean in sonication if necessary), the diamond gets transferred onto p-doped Si (or just Si or silica) and bonded to the substrate. Best bonding results are obtained when the surfaces of the diamond and the substrate are freshly cleaned, and when the diamond is rinsed in DI water (instead of solvents) after the acid clean. Then, deep etching can be performed and figure 14 presents a good quality well-bonded thin film.

The deep etch itself contains of cycling through the following steps: 1) $10 - 30\,\text{min}$ Ar/Cl_2 etching, 2) up to $30\,\text{min}$ oxygen etching and 3) $15\,\text{min}$ cooling while purging the chamber with Ar. The last step is necessary to prevent graphitization due to the associated heating after

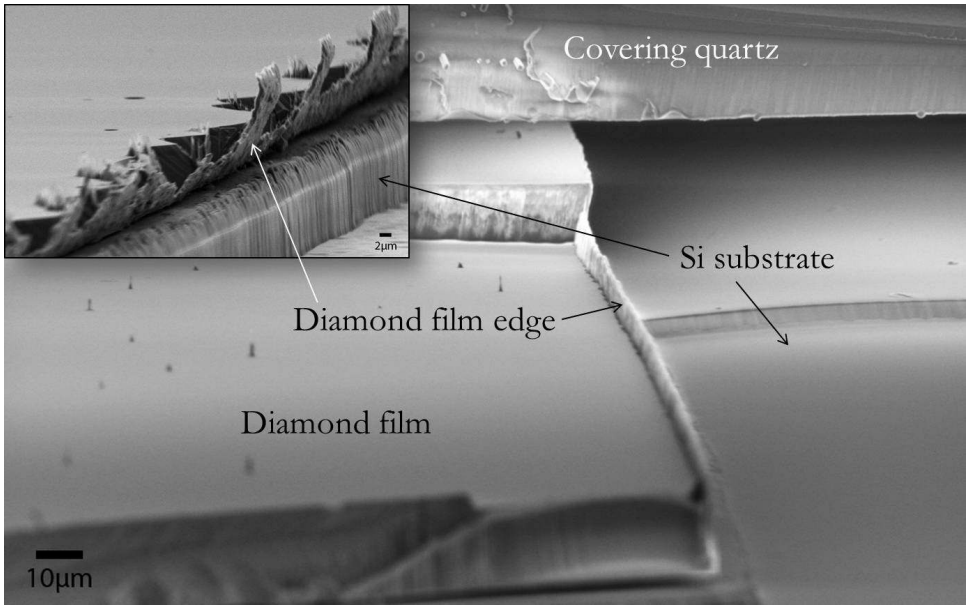

Figure 11: During deep etching sidewalls form due to either re-deposition of material or different etch rates for different crystal orientations.

long etching. The etch rate of the oxygen rate has been found to be $200 - 250\,\mathrm{nm/min}$. The etch rate varies with chamber condition over time, and the Ar/Cl_2 etch rate itself can vary immensely. Overall an etch rate around $6 - 8\,\mu\mathrm{m/cycle}$ has been established. The etch has to be stopped when the diamond starts to get etched through at one of the sides (due to the wedged profile of the initial diamond substrate), which can be observed through the chamber window. A final cleaning step and transfer to SiO_2/Si substrate is necessary when making integrated devices like ring resonators. For suspended devices such as PCCs the diamond can remain on Si which will eventually be undercut beneath the devices. In general, the better the quality of the

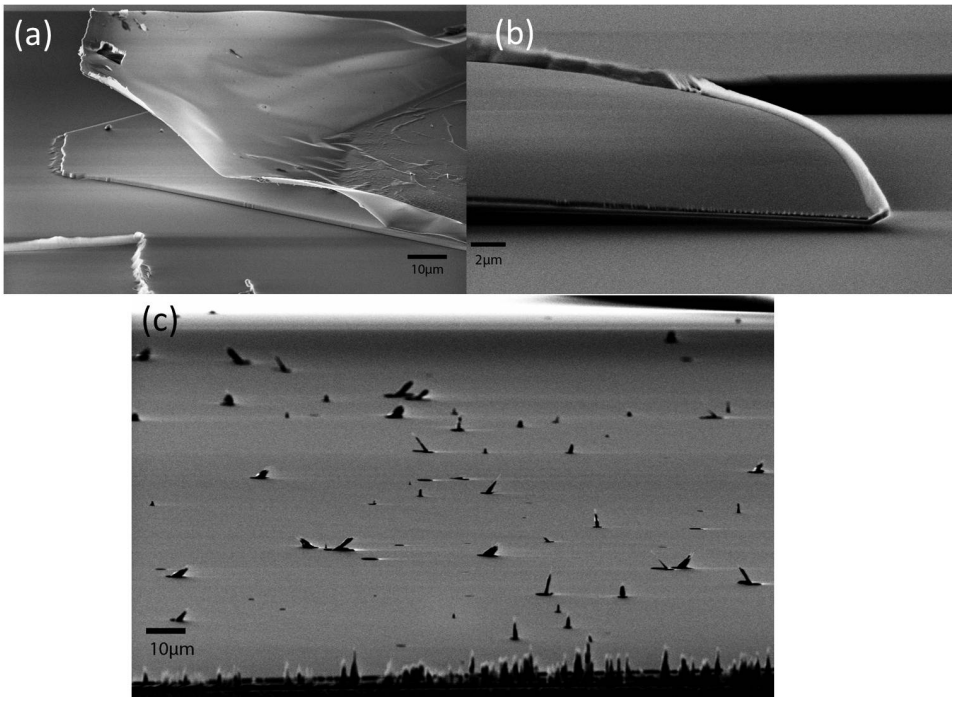

Figure 12: (a-b) Residual stress in the films, that most likely arise during the polishing process, can cause warping of films for thin thicknesses. **(c)** Non-clean surfaces can assist the formation of nanowires which can first lead to dimples that eventually result in holes in the film.

original diamond film (in terms of roughness and cleanliness), the better is the bonding strength. Obtaining a nice thin film without breaking it into small pieces during the cleaning and transfer steps and without many dimples is the most tricky part of the fabrication process. After the final film thickness is achieved and the (good) film is transferred and bonded well on the final substrate, the student can take a deep breath and be happy.

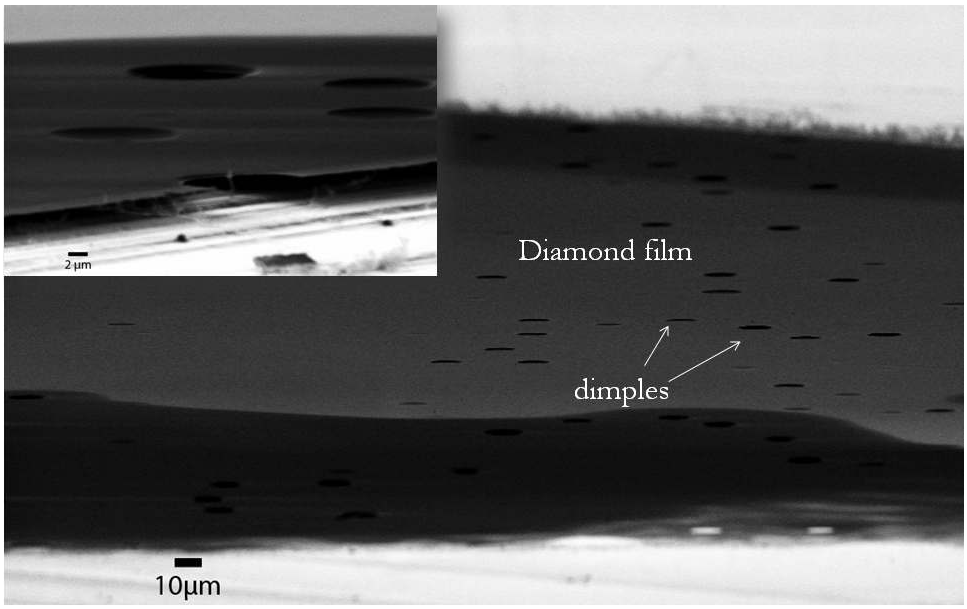

Figure 13: A diamond film on substrate containing "dimples" after the thinning process that result in holes in the film.

Finally, EBL is used to expose XR and/or FOx resist to form a mask which is transferred to the diamond film in another etch.

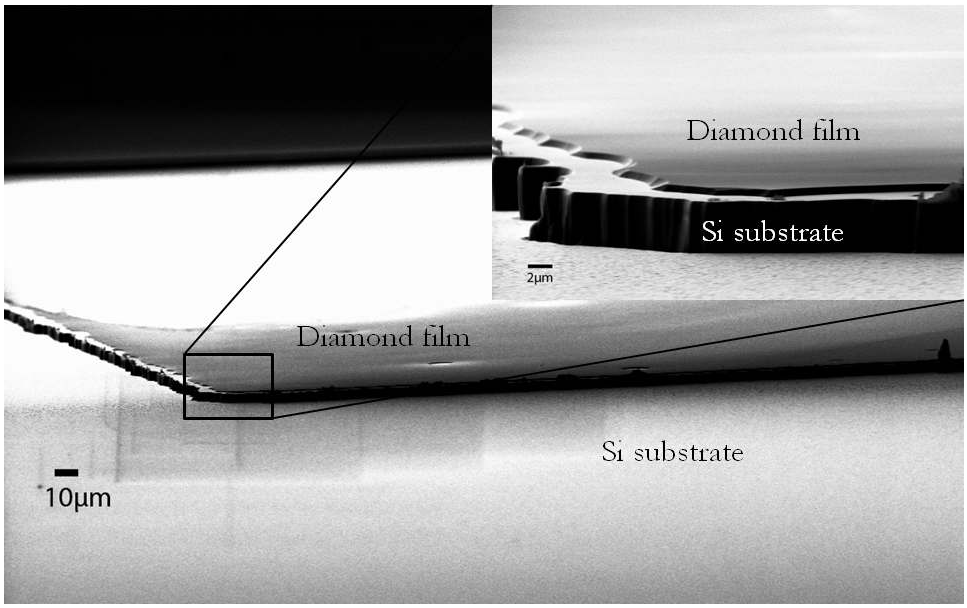

Figure 14: Well-bonded diamond thin film on a Si substrate after deep etching.

3.3 Implantation

In collaboration with the Lukin group and Yacoby group at Harvard, different routes in implantation have been pursued [8, 39]. Here, the main goal is the formation of photostable NV centers having lifetime-limited ZPL even in diamond nanodevices. Prior to our work, implanted NV centers have not been observed to have narrow ZPLs (or any at all in resonant absorption measurements [89]) even in bulk, and furthermore often are not even photostable for a long time at low temperature. Moreover, the quality of implanted NV centers seems to be even more affected in nanostructures at low temperature. To understand the origin of this problem and to find suitable solutions,

we study different implantation conditions, and post-implantation treatment procedures. Our efforts have resulted in the formation of high quality NV centers in bulk and nanodevices even at low temperature.

Spectral diffusion is introduced by the green laser pulse that re-ionizes the NV center after each resonant red pulse in resonant absorption measurements. The relatively high energy photons of the green laser (2.3 eV) can however excite various other defects, surface states etc surrounding the NV center. It has been shown that a very weak resonant excitation of the NV^0 at 575 nm can decrease spectral diffusion effects significantly [161]. This scheme could potentially circumvent spectral diffusion due to surface states for implanted NV centers in diamond nanodevices as well.

3.3.1 Annealing

First, the annealing procedure has been revisited. In literature, NV center implantation is typically followed by a 2 hour anneal at around $750 - 800$ °C where vacancies are known to start diffusing in the crystal and to form NV centers. However, the implantation does not leave the lattice unaffected, but rather causes interstitials, vacancies, vacancy complexes and other defects as the ions impinge on the diamond lattice. The photostability and spectral properties depend strongly on the NV center's environment and other defects might

cause photoionization of the negatively charged NV center or spectral broadening. The Nitrogen itself can come to rest either as interstitial point defect or at a Carbon lattice site. At ≈ 400 °C, the interstitial Nitrogens start moving to find lattice sites. It has been found that the formation of NV centers is most effective at around 800 °C. However, at that temperature, other defects (such as di-vacancies [169], vacancy complexes) might not move yet. Hence, at even higher temperatures, other defects and vacancy complexes might start diffusing away from the Nitrogen and NV center layer and might also leave the crystal. Therefore, we implemented a 3-step annealing procedure that consists of a 4 hour anneal at 400 °C, followed by a 2 hour anneal at 800 °C and a 2 hour anneal at 1200 °C in high vacuum.

3.3.2 Implantation density

Second, we study the ZPL linewidth as a function of nitrogen ion density while implementing the above mentioned annealing procedure. Here, only electronic grade IIa CVD (Element Six) diamonds have been used. The depth of the implantation was aiming at 100 nm for the data presented, corresponding to an ion energy of ≈ 80 keV. We note however, that the actual depth can significantly deviate from the intended depth due to channeling effects [48, 179]. Before implantation, samples were pre-etched for 2 μm to remove the residual stress layer from mechanical polishing in Ar/Cl_2 and oxygen RIE steps

and acid cleaned before being shipped for Nitrogen ion implantation (Core Systems). After the implantation the samples were acid cleaned, annealed and acid cleaned again, followed by a 145 min long RTP step in oxygen flow (5000 sccm) to minimize background fluorescence originating from surface functionalization effects.

Figure 15 shows confocal scans and corresponding representative resonant absorption ZPL scans measured in the phonon sideband at $4 - 7\,\mathrm{K}$ for Nitrogen ion dosages of $10^9\,\mathrm{cm}^{-2}$, $10^{10}\,\mathrm{cm}^{-2}$, $10^{11}\,\mathrm{cm}^{-2}$ and $10^{12}\,\mathrm{cm}^{-2}$. For nanodevices, a high NV density is preferable so that a high yield of cavities containing a single NV center can be achieved. However, it can be seen that the spectral properties of the ZPL deteriorate when the Nitrogen content in the crystal increases within our range of tested dosages. Remarkably, for a dosage of $10^{10}\,\mathrm{cm}^{-2}$ we observe almost lifetime limited linewidths down to $\approx 30\,\mathrm{MHz}$ with good photostability (over weeks). Here, the Nitrogen to NV conversion efficiency is 1% (or 1 NV center per $1\,\mu\mathrm{m}^2$). For a lower dosage, the conversion efficiency seems to be too low for an efficient integration of NV centers with devices. Hence, for our purpose, we found an optimum dosage to be $10^{10}\,\mathrm{cm}^{-2}$. This result can be interpreted as follows: The photostable and low spectral diffusion ZPL seems to be accompanied by a certain Nitrogen content in the crystal. The Nitrogen atoms, whose level is about 1.8 eV below the conduction band of diamond, can be easily excited and hence ionized with the

green pump laser (2.3 eV). The electron can then relax (under photon emission) and be captured by the NV center. Therefore, the implanted Nitrogen atoms act as an electron donor bath (up to a certain degree), thus stabilizing the NV^- centers. For higher dosages however, spectral diffusion introduced by the high Nitrogen content and/or accompanied by other defects or a general deterioration of the diamond lattice by the high Nitrogen dosage broadens the ZPL.

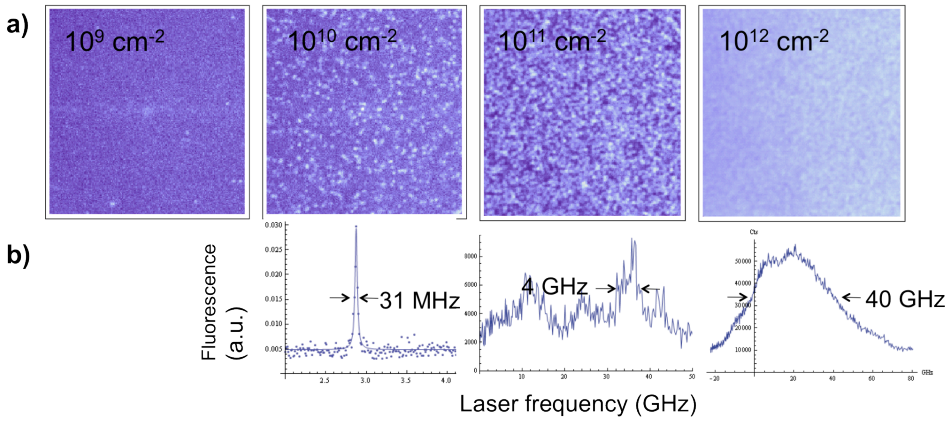

Figure 15: The density and ZPL linewdith as a function of Nitrogen ion implantation density is shown in confocal scans **(a)** and representative ZPL resonant absorption scans in **(b)**.

3.3.3 Nanodevices and surface effects

When devices are fabricated in diamonds that underwent the optimized implantation procedure the ZPL properties deteriorate significantly in both photostability and spectral diffusion. This effect seems to be more severe with decreasing device size suggesting surface

effects as possible cause. The properties can be restored to some degree ($\approx 100\,\mathrm{MHz}$ in the best case, $\approx 1\,\mathrm{GHz}$ reliably) when repeating the annealing process discussed above. The requirement of re-annealing increases the difficulty of the use of thin films since handling of the 250 nm thick films is delicate. Therefore, we identified bulk-nanomachined diamond cavities, using angle etching approach, as better suited direction for realization of cavity QED systems based on NV centers [30]. However, the relatively low density of our optimized dosage requires the mapping of NV centers in the beams with subsequent alignment and cavity formation around the found NV centers in PMMA slab cavities [188].

4

Diamond nanowires for improved collection efficiency of photons

To achieve efficient extraction of single photons from an NV center, we first consider a nanowire structure made from bulk crystal [72], [11] (Fig. 16). The development of a robust light source that emits

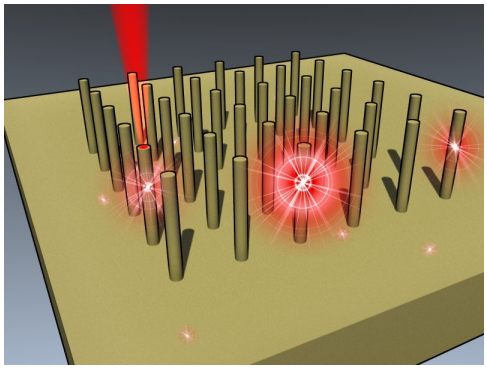

Figure 16: Cartoon of diamond nanowires containing NV centers.

one photon at a time will enable new technologies such as perfectly secure communication via quantum cryptography [21]. Devices based on fluorescent dye molecules [112], quantum dots [52], and carbon nanotubes [83] have been demonstrated, but none have combined a high single photon flux with stable, room-temperature operation. Luminescent centers in diamond [2, 20, 64, 101, 174] have recently emerged as a candidate for these applications, and the remarkable NV center additionally possesses spin quantum bits with optical read-out [13, 50, 90, 121, 129, 138]. In this chapter, a single photon source composed of an NV center in a diamond nanowire overcoming this limitation is reviewed. The device produces ten times greater photon flux than a bulk diamond, while using ten times less power. This result enables a new class of devices for photonic and quantum information processing based on nanostructured diamond, and could have broader impact in nanomechanical systems (NEMS), sensing, and scanning probe microscopy.

4.1 Design and Modeling

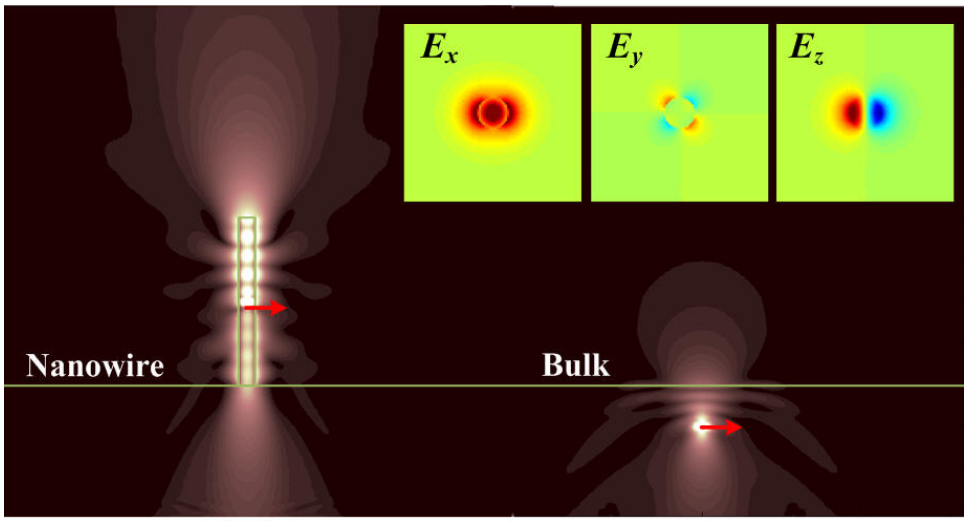

Figure 17: Field profile of the E-field's radial component (E_r) in the case of a $2\,\mu$m long, 200 nm diameter diamond nanowire (left) and a bulk diamond (right). The dipole is polarized parallel to the interface, emitting at $\lambda = 637$ nm (zero-phonon line wavelength of NV center). The fundamental nanowire waveguide mode (HE_{11}) (inset) is the dominant decay channel for the nanowire case.

First, we studied the emission from an NV center (modeled as a dipole) in a diamond nanowire using FDTD simulations. We assume a circular cross section of the nanowire with a diameter d, and consider the two general polarization scenarios for a dipole/nanowire system: dipole polarization perpendicular (s-polarized) and parallel (p-polarized) to the nanaowire axis. The dipole associated with an NV center in (100) diamond can be represented using a combination of these two dipoles, since it is polarized in the (111) plane. At

different wavelengths within the NV center's radiation spectrum ($637\,\text{nm} - 780\,\text{nm}$), the number of collected photons per second can be expressed as $\Gamma(\lambda) \cdot \eta(\lambda)$ where Γ is the emission rate (reciprocal to the lifetime) and η the collection efficiency. The collection efficiency can be dramatically improved in diamond nanowires compared with bulk diamond, as demonstrated in Figure 17. These field profiles show that the major portion of light emitted from an NV center in bulk diamond leaks to the substrate due to significant total internal reflection at the diamond-air interface, whereas in a diamond nanowire the fundamental HE_{11} mode is the dominant emission channel for a dipole polarized perpendicular to the nanowire axis (in the xy plane) 17 (inset) [61]. This waveguide mode directs the light propagating in the nanowire, and is scattered vertically as it approaches the top nanowire facet. This process allows for efficient collection using an objective lens positioned above [119].

In Figure 18(a) we show the coupling efficiency, α, between NV center and nanowire waveguide mode as a function of the nanowire diameter, for wavelength $\lambda = 637\,\text{nm}$. It can be seen that, in the case of s-polarized dipole, more than 80% of emitted photons can couple to a nanowire mode for a broad range of nanowire diameters ($180\,\text{nm} - 230\,\text{nm}$). We choose to work with 200 nm diameter nanowires in order to optimize the coupling efficiency. Photon collection efficiencies can be quantified from the far-field profile of

power emitted from the top nanowire facet, shown in Figure 18b and c. An objective lens with a numerical aperture NA=0.95, positioned above the nanowire, can collect light emitted into the solid angle of 72° (represented by shaded areas in the far field emission profiles). It can be seen that in the case of both s- and p-polarized dipoles, 100% of photons emitted from the nanowire can be collected with the lens. It is interesting to note that this is true even for a p-polarized dipole despite the fact that it cannot couple to the nanowire waveguide mode due to the symmetry mismatch. In this case, however, the large collection efficiency is enabled by coupling to radiative and leaky modes that are also modified by the presence of the nanowire. Finally, comparing a dipole in a nanowire (red line in figures 18b and c) with a dipole in a bulk diamond crystal (blue line), we find that nanowire geometry provides one and two orders of magnitude improvement in the collection efficiency in the case of s-polarized and p-polarized dipole, respectively.

We also evaluated the total emission rate (the reciprocal of lifetime) of an NV in a nanowire, and found that it is dependent on the NV's position: Fabry-Perot resonances, formed due to the (weak) reflection of a waveguide mode from the nanowire's facets, can modify the emission rate of s-polarized dipole. We introduce the enhancement (Purcell) factor $F_P(\lambda) = \frac{\Gamma_{NW}(\lambda)}{\Gamma_0(\lambda)}$ where Γ_0 is the emission rate of the quantum emitter in a homogeneous diamond medium. It describes the

modification of the NV center fluorescence lifetime in a nanowire ($\tau_{NW} = 1/\Gamma_{NW}$) compared to the bulk ($\tau_{bulk} = 1/\Gamma_0$). For $\lambda = 637\,\text{nm}$ and $d = 200\,\text{nm}$, the enhancement factor is in the range of $0.65 - 1.10$, depending on the dipole position along the nanowire positions. It is interesting to note that the collection efficiency for s-polarized dipole is maximized (Figure 18b) when destructive interference occurs between downward emitted photons and photons reflected from the top nanowire facet (Figure 17). This case favors an upward emission at the expense of slightly increased radiative lifetime.

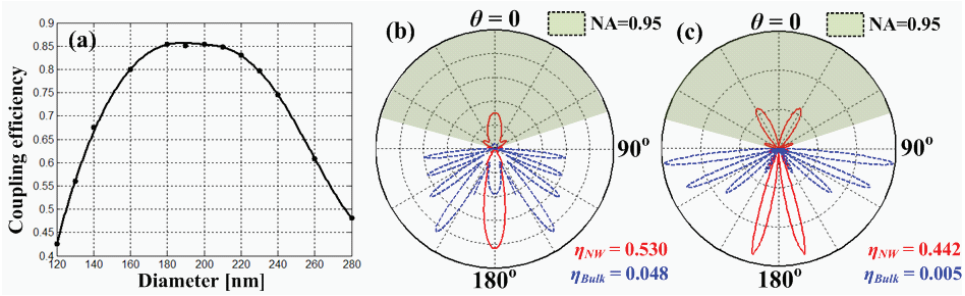

Figure 18: (a) Coupling efficiency α as a function of the nanowire diameter at $\lambda = 637\,\text{nm}$. The dipole is assumed to be placed at the center of the nanowire with a polarization parallel to the interface. **(b)** and **(c)**: The far-field profile of power emitted from a **(b)** s-polarized (perpendicular to the nanowire) and **(c)** p-polarized (parallel to the nanowire) dipole embedded at the center of a nanowire with $d = 200\,\text{nm}$. Blue lines, in both **(b)** and **(c)**, show far-field profiles of emitter embedded in the bulk diamond crystal. The shaded areas denote the light that can be collected using an objective lens with an NA of 0.95. Calculated values of collection efficiency η for nanowire and bulk, for both polarizations, are also indicated.

To take into account wavelength and polarization dependence of parameters F_P and η, they were averaged over the room temperature

NV center fluorescence spectrum $I(\lambda) = \Gamma_0$, as well as over the (111) plane of a (100) diamond crystal in which NV dipole resides. The total number of collected photons is obtained by averaging over wavelengths and polarizations, by using following (unitless) figure of merit

$$Z = \frac{\int\int F_P(\lambda,\sigma)\eta(\lambda,\sigma)\Gamma_0(\lambda)d\sigma d\lambda}{2\pi\int\Gamma_0(\lambda)d\lambda} \tag{4.1}$$

where σ denotes the polarization angle.

Using this figure of merit, we find that nanowire geometry provides an order of magnitude improvement ($Z \approx 30\%$) over the bulk diamond case ($Z \approx 3.3\%$). We note that F_P and η are sensitive to radial and axial position of an NV center within a nanowire due to the Fabry-Perot resonances formed between the nanowire facets.

4.1.1 Device fabrication and experimental setup

To confirm our predictions in experiment, we fabricate arrays of nanowires with the designed geometrical parameters. The fabrication is similar as presented in section 3 and depicted in figure 19a. Briefly, EBL is used to define the etch mask in HSQ. The mask is then transferred into diamond using an ICP RIE with an oxygen-based gas chemistry. The etch consists of a 3-step or 4-step process where the Bias or ICP power is varied with time if vertical nanowires are

intended. For example, for 2 μm tall wires, for the first 2 min, 700 W ICP power is applied, then 3 min of 600 W ICP power, and finally 5 min of 1000 W ICP power. A SEM image of an array of fabricated devices is presented in Fig 19b. The nanowires have diameters of ≈ 200 nm and height of 2 μm to meet the modeling predictions. Synthetic type Ib HPHT (Element Six) and CVD grown type IIa electronic grade diamonds have been used. These samples respectively contain naturally occurring NV centers, created during the diamond synthesis process, and NV centers created via ion implantation[73].

To characterize our devices, we used a confocal microscope (Fig. 19c) with a 0.95 N.A. air objective, resulting in a collection half-angle of 72 °. This allows for ideal isolation of a single photon emitter by exciting and collecting emitted photons from a small focal volume ($0.25 - 0.5\,\mu m^3$). Such a configuration is suitable for characterizing NV centers in a bulk substrate, as well as in nanowires, and allows for fair comparison between the two geometries. The devices are mounted on a scanning piezo-stage, and a green laser (532 nm) is used to excite the devices. Emission from the NV centers is transmitted through the dichroic mirror, then filtered with a long-pass filter (630 nm) to remove both the excitation light and diamond Raman signal, and finally detected using avalanche photo-diodes (APD) [11]. This allows us to obtain the luminescence image of our sample (Fig. 19e). To bleach residual background fluorescence typically found after the

oxygen RIE process, the arrays were scanned slowly with a green laser at a few mW. We note that all measurements of optical devices discussed in this chapter were performed at room temperature.

4.1.2 Autocorrelation function measurement

The emission characteristics of single NV centers embedded in the bulk are compared to those in nanowires. In both cases the presence of a single emitter can be inferred by measuring its second order photon correlation function using the Hanbury Brown Twiss (HBT) configuration [28]. In the measurement, the photon stream is divided using a beamsplitter (fiber beam splitter in this case), directed to two APDs (Fig. 19c), and the delay between the arrival time of photons is recorded. The finite lifetime of the NV center results in the time delay between photon emission events. Therefore, within one emission lifetime, only one photon can be present in the stream, and only one of the APDs can register photon arrival. Hence, the intensity correlation function, defined as

$$g^{(2)}(\tau) = \frac{\langle I(\tau + t)I(t)\rangle}{\langle I(t)\rangle^2} \tag{4.2}$$

where τ is the delay time, is 0 for a perfect single photon flux at $\tau = 0$ (called photon antibunching). Residual background that impinges on the APDs results in $g^{(2)}(0) > 0$ and a true single photon source has $g^{(2)}(0) < 0.5$ as upper bound in the absence of an additional emitter

[94]. The width of the dip at zero delay carries information on the emitter's lifetime and provides a way to measure the lifetime without a pulsed laser source for pump powers below saturation [11]. Away from the dip the photon statistics are Poissonian and result in $g^{(2)}(\tau) = 1$. The inset of fig. 19b shows the pronounced signature of a single photon correlation for an NV center in a nanowire below saturation pump power. Additionally, the $g^{(2)}$ function has been evaluated at different pump levels below and above saturation (Fig. 20a-c). A long-lived intermediate shelving state of the NV center gives rise to $g^{(2)}(\tau) > 1$ in the vicinity of the dip under high pump powers, a phenomenon called bunching [101]. In addition, the main features of the level crossing system that lead to the polarization mechanism of the $m_s = 0$ sublevel of the triplet ground state and the spin-dependent fluorescence rate [117] remain unchanged after nanostructuring. This was confirmed by standard electron spin resonance (ESR) and Rabi measurements (data not shown).

Additional information about the optical properties of an NV center in a diamond nanowire may be obtained by triggering the emission of single photons. We have constructed a versatile pulsed excitation system for this task. Ultrafast (200 fs) pulses generated by a Ti:Sapphire (Coherent Mira 800-F) laser were used to generate supercontinuum white light in a photonic crystal fiber (Newport, SCG-800). A pump wavelength of 800 nm maximized the overall

spectral density at green wavelengths, which was then isolated using band-pass filters in the $510 - 540\,\text{nm}$ wavelength range (Semrock), collected with an optical fiber, and used as an excitation source for our confocal microscope. Since the radiative rate of an NV center in a diamond nanowire ($60 - 80\,\text{MHz}$) is comparable to the fundamental repetition rate of the Ti:Sapphire pulse train ($76\,\text{MHz}$), an electro-optic modulator (ConOptics, Model 350) was used to reduce the repetition rate to $10.8\,\text{MHz}$ prior to launching in the photonic crystal fiber. We used this excitation scheme to observe the full temporal dynamics of the diamond nanowire fluorescence (in this case for implanted NV centers). Pulsed intensity auto-correlation measurements show a series of spikes in coincidence counts at times separated by an integer number of laser repetition cycles (Fig. 20d). Strong suppression of the central peak $g^{(2)}(0) \approx 0.16$ is observed at a pump power of $65\,\mu\text{W}$, which is consistent with the extent of the photon anti-bunching observed using CW excitation.

4.1.3 Evaluation of overall device performance via saturation measurements

The overall performance of single NV centers is appraised in their saturation behavior and is statistically compared to that in bulk. Intrinsically, a quantum emitter's emission intensity I levels off after a

certain pump level P_{sat} according to [101]

$$I(P) = \frac{I_{sat}}{P_{sat}/P_0 + 1} \tag{4.3}$$

where I_{sat} and P_0 are the saturated emission intensity and pump power respectively. P_{sat} and I_{sat} were extracted from a measurement of the device count rate for different pump powers. For a representative bulk NV device, $I_{sat} = 21 \pm 2\,\text{kCPS}$ and $P_{sat} = 990 \pm 540\,\mu\text{W}$. The result for a typical nanowire device is $I_{sat} = 168 \pm 37\,\text{kCPS}$ and $P_{sat} = 58 \pm 37\,\mu\text{W}$. This corresponds to $\approx 2.5 \cdot 10^{-4}$ collected photons per NV center lifetime in the bulk device and $\approx 2.5 \cdot 10^{-3}$ in the nanowire antenna. Factors such as optical cycling through the metastable shelving state, and more importantly losses in the optical system used in the experiment, are the reason that the absolute photon counts measured in our devices deviate from the theoretical predictions. However, relative comparison between photon counts obtained from diamond nanowire and bulk diamond is insensitive to these imperfections and Fig. 21 shows saturation intensity levels versus saturation pump powers for several single emitters in nanowires compared to bulk. The nanowire efficiently funnels light to- and from the NV center, resulting in a ten-fold improvement in saturation count level at one-tenth of the saturation pump power required in the bulk. The enhancements in excitation and extraction confirm the predictions from FDTD

modeling. Similar count rates have been predicted and measured with SILs, which also enhance photon collection efficiency by overcoming TIR [70]. In addition to the characterization of NV centers, diamond nanowires have been also made in substrates containing SiV centers in collaboration with the Becher group. Furthermore, the oxygen environment in the RIE process might have assisted the generation of a new, oxygen related defect center in diamond, which has been characterized in the Wrachtrup group. However, the origin of the defect is still not clear [106].

4.1.4 Implanted nanostructures

Two different approaches in the characterization of implanted NV centers in diamond nano devices have been pursued: 1) Devices (in this case small nanoposts) are fabricated after implantation of Nitrogen ions, while in method 2) devices (nanowires) are fabricated prior ion implantation.

Small nanoposts have been fabricated in an implanted high quality electronic grade type IIa CVD diamond (Element 6) with low ($< 5\,\mathrm{ppb}$) background Nitrogen content. The sample was implanted with $^{15}\mathrm{N}$ ions at an energy of $14\,\mathrm{keV}$ and a dosage of $1.25 \cdot 10^{12}\,\mathrm{cm}^{-2}$. Stopping Range of Ions in Matter (SRIM) calculations project a Nitrogen layer $20\,\mathrm{nm}$ below the diamond surface. Next, the sample was annealed at $750\,^{\circ}\mathrm{C}$ for 2 hours in high vacuum ($< 10^{-6}\,\mathrm{Torr}$) to

mobilize vacancies and generate a shallow layer of NV centers. Following the method presented in chapter 3 arrays of 200 nm tall posts with 65 nm radius were fabricated. Ten of the seventeen devices that we tested showed strong photon anti-bunching. The other seven devices were characterized by $0.5 < g^{(2)}(0) < 0.7$, which is consistent with the presence of two or three NV centers in the device. Since at least ten of the one hundred total devices in this particular array contained a single NV center, this combined implantation and fabrication routine may be implemented with a high yield (>10%) operating in the single photon regime. Our high-throughput fabrication technique can generate many more devices than can be tested in serial with the standard confocal microscope system. This suggests the future need to develop automated characterization tools or wide-field microscope approaches that optically address many devices in parallel.

Next, we modify the approach slightly and implant single NV centers in diamond nanowire antennas. The diamond nanowires were then implanted with ^{15}N at 1.7 MeV and $1 \cdot 10^9\,\mathrm{cm}^{-2}$ dosage and annealed in the same conditions as noted above. SRIM calculations indicate that this produces a layer of NV centers 1 μm below the diamond surface. A relatively low yield of nanowires containing a single NV center was found, which can be attributed to a) the lower dosage used compared to the previous sample but b) also the reversed

technique.

Photon antibunching in the nanowire fluorescence $g^{(2)}(0) \approx 0.06$ was possible without background subtraction, which represents a 5-fold reduction compared to nanowire devices demonstrated in type Ib material. Contributions to the nanowire fluorescence come from single photons, S, that lead to non-classical correlations at zero time delay, as well as background fluorescence, B, emitted with Poisson statistics that reduces the observed contrast. For a given pump power, the relative contributions of S and B to the total fluorescence are encoded in the anti-bunching contrast according to [20] $g^{(2)}(0) = 1 - \rho^2$, where $\rho = S/(S + B)$. We therefore measured both the total number of photon counts per second from the nanowire as well as $g^{(2)}(0)$ for different pump powers P (Fig. 22a). The results are in good agreement with theoretical predictions (dashed line). The saturation curve for this device demonstrates that an implanted nanowire may act as a high-flux single photon source (Fig. 22b). The maximum possible number of photons collected per second was $I_{sat} = 304,000$ and the pump power scale to saturate the NV center emission was $P_{sat} = 0.34\,\mathrm{mW}$.

4.1.5 Lifetime evaluation

The fluorescence lifetime of a color center in the diamond nanowire gives an upper bound on the number of single photons that may be collected. Lifetimes of single NV centers in nanowires have been extracted from the $g^{(2)}(\tau)$ statistics as well as by pulsed excitation. In the former method, the lifetime is encoded in the temporal width of the autocorrelation data, whose exponential decay is of the form $\exp\left(-(r+\Gamma)|\tau|\right)$ for low pump powers [20, 101]. Here, r is the pump rate, $\Gamma = 1/\tau_{NW}$ is the NV center decay rate, and τ_{NW} is the NV center lifetime in the nanowire. The overall decay rate $r + \Gamma$ was measured at different pump powers and observed to decrease linearly at low pump powers (Fig. 23a, here for natural NV centers in type Ib material). The lifetime of six different nanowire devices was observed to be in the range 14.6 ± 1.9 ns, which is slightly longer than the lifetime of an NV center in a bulk material as expected. A similar lifetime was extracted for both natural as well as implanted NV centers compared to ≈ 11 ns in the bulk material [11, 73] and 25 ns in nanocrystals [20]. The fluorescence lifetime of an NV center in diamond nanowire is expected to be intermediate between bulk diamond, where the NV center lifetime is short due to the large background refractive index ($n \approx 2.4$), and an NV center in a diamond nanoparticle, which resembles a dipole in air ($n \approx 1$) [61].

Additionally, we were able to make a direct measurement of the

exponential decay of the nanowire fluorescence after pulsed excitation (Fig. 23b). A fit was obtained from a bi-exponential function using a fast time constant $\tau_{bg} = 1.5\,\text{ns}$, which corresponds to the decay of the background fluorescence, and a slow time constant $\tau_{NV} = 13.7\,\text{ns}$, which corresponds to the fluorescence decay of the NV center in the nanowire.

4.2 Conclusion and applications of diamond nanowires

In this chapter, the design, fabrication and characterization of diamond nanowires has been reviewed. The large scalability, combined with the option of ion implantation or integration of different defect centers as well as transferability make this device a promising candidate for numerous applications.

4.2.1 Transfer of wires

Extending their use as a substrate based device, transferring wires is advantageous in several ways:

- The collection efficiency of photons potentially further increases, especially if the out coupling nanowire tip is tapered.
- The wires could be used for applications in biosensing where huge amounts of wires are necessary to feed fruitflies.

- Their integration as tips for e.g. sensing, electron field emission or robust scanning tip is imaginable.

In addition to earlier attempts to transfer wires, as outlined in my diploma thesis, we pursued a technique where the wires would be transferred within a UV curable epoxy and hence be embedded vertically in the epoxy. First results in this regard can be seen in figure 24. The sample is first embedded in UVO 114 epoxy, and cured in UV light for 20 min. The sample is then "knocked off" the epoxy and leaves a mold therein (Fig. 24a). The arrays of wires can be seen in the epoxy (Fig. 24b) as well as transferred wires (Fig. 24c). It was confirmed that the majority of wires were removed from the diamond sample.

4.2.2 Magnetometry and sensing

Room temperature applications such as magnetometry and near-field sensing can potentially benefit greatly from the brightness of nanowires (over e.g. nanodiamonds, which are about an order of magnitude less bright [20]) . For example, the nanowire antenna effect has been employed to realize a scanning near field and magnetic field sensor [116]. The nanowire is made on a diamond cantilever carved from a thin film diamond slab (50 μm) in a deep dry etch and optical characterization is performed from the cantilever side which is advantageous in terms of collection efficiency (Fig. 25). Here, a

magnetic field sensitivity of 56 $\frac{\mathrm{nT}}{\sqrt{\mathrm{Hz}}}$ was established for 10 nm deep implanted NV centers at the tip revealing long spin coherence times up to 75 μs. The NV center at the tip can also be used as optical near-field sensor and a spatial resolution of down to 20 nm has been observed.

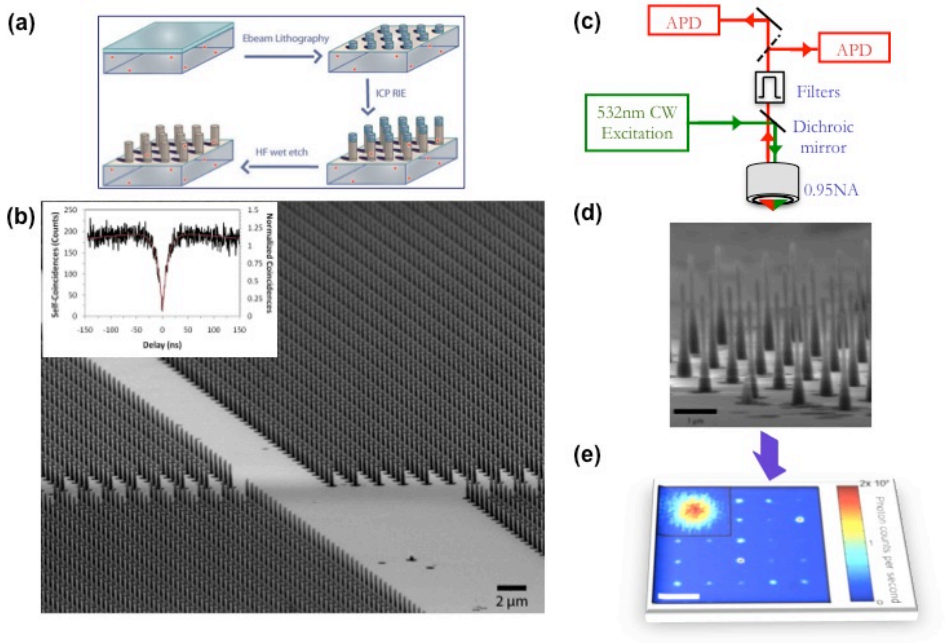

Figure 19: Efficient and scalable single photon sources based on diamond nanowires: **(a)** Fabrication schematic shows spin-on-glass resist deposition, definition of an etch mask using e-beam lithography, transfer of the mask into the diamond via an oxygen reactive ion etching step and removal of remaining mask using HF. **(b)** SEM image of arrays of $2\,\mu\mathrm{m}$ spaced diamond nanowires with $2\,\mu\mathrm{m}$ height and $200\,\mathrm{nm}$ diameter. Inset: A second order correlation function shows a pronounced dip at zero delay indicative of single photon emission for an NV center in a diamond nanowire [73]. **(c)** A schematic of a confocal microscope setup used to characterize nanowires. **(d),(e)** For visualization a (graphically rotated) confocal scan of diamond nanowires is shown in **(e)**.

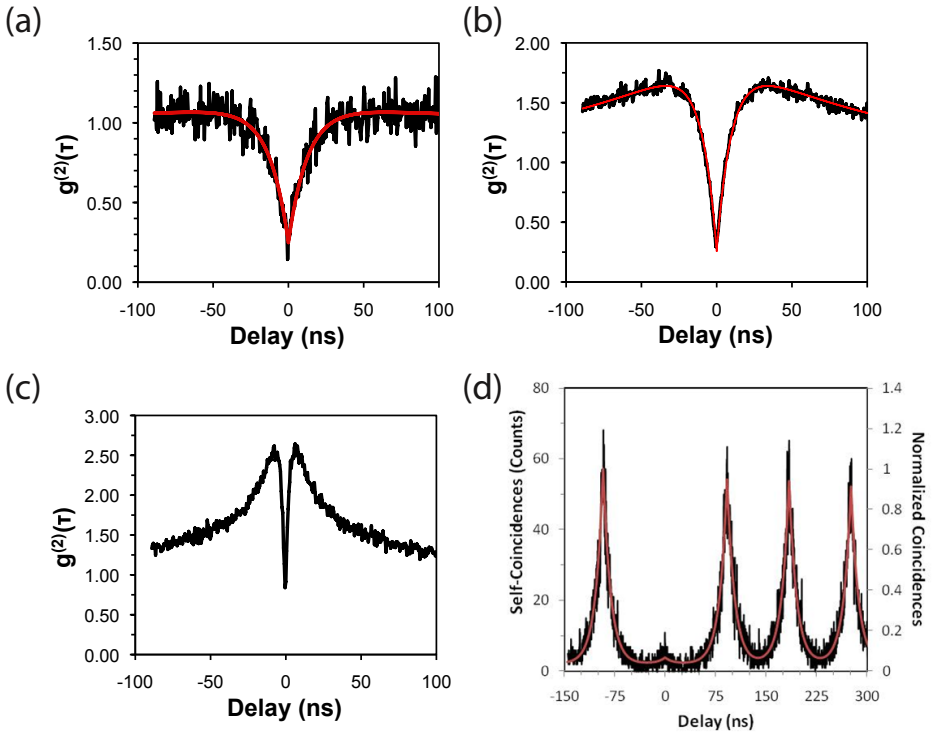

Figure 20: a-c The presence of a single quantum emitter in the diamond nanowire is revealed by the second-order autocorrelation function $g^{(2)}(\tau)$. The dramatic decrease in the number coincidence counts at zero time delay ($g^{(2)}(0) < 0.5$) indicates that photons from the nanowire device are anti-bunched. Qualitatively different dynamics are observed at different excitation powers: **(a)** $11\,\mu\mathrm{W}$ below saturation, **(b)** $190\,\mu\mathrm{W}$ near (but above) saturation, and **(c)** $1.6\,\mathrm{mW}$ above saturation. At high pump powers, coupling to the metastable shelving state is significant and results in bunching shoulders ($g^{(2)}(\tau) > 1$) at intermediate times. Red curves in **(a)** and **(b)** are fits using a three-level model of the $g^{(2)}(\tau)$ function [101]. **d** Photon anti-bunching measurement of a diamond nanowire using pulsed excitation ($65\,\mu\mathrm{W}$ average pump power). Strong suppression of the central peak at zero delay $g^{(2)}(0) \approx 0.16$ is observed without background subtraction. Raw data (black) and theoretical fit (red) are shown.

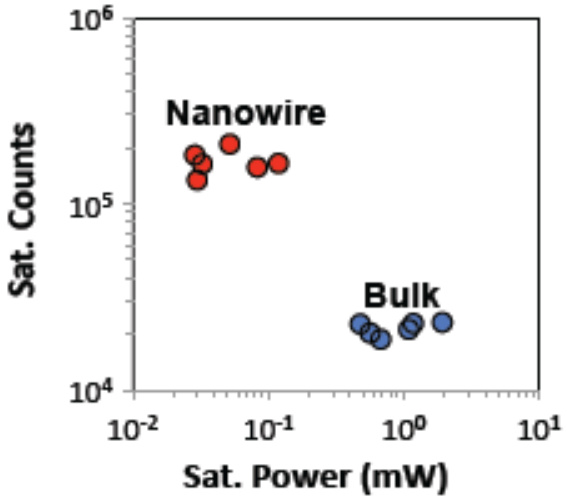

Figure 21: Comparison of saturation parameters of the emitter in bulk diamond versus diamond nanowire. The coupling between the emitter and the waveguide mode provides a ten-fold improvement in the excitation and photon collection efficiencies [11].

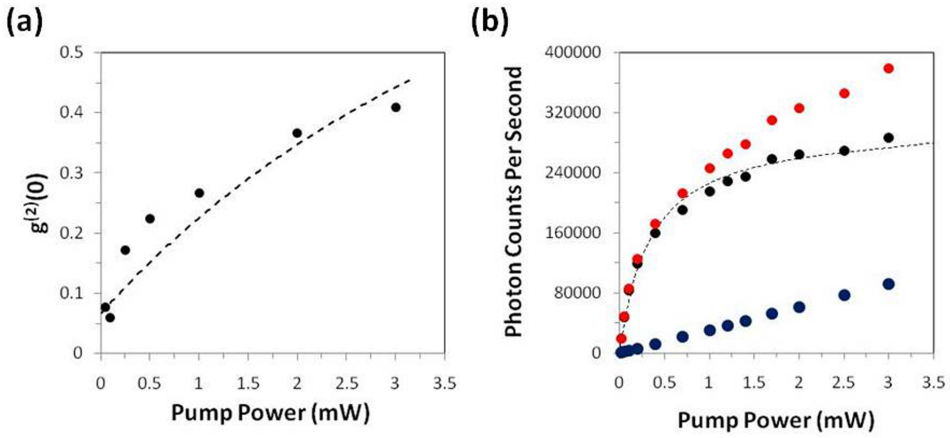

Figure 22: (a) $g^{(2)}(0)$ as a function of pump power. Dashed curve is the expected level of coincidence counts $1 - \rho^2$ based on the measured saturation data (not shown), where $\rho = S/(S + B)$, S is NV center single photon count rate, and B is background fluorescence count rate. **(b)** Total nanowire fluorescence from the same device is presented in red, the background fluorescence obtained from contrast in photon anti-bunching data in part **(a)** is shown in blue, and the remainder of the net single photon counts from an embedded NV center is shown in black. A fit of the NV center fluorescence to the saturation model is given by the dashed black line. Pump power was measured before the microscope objective.

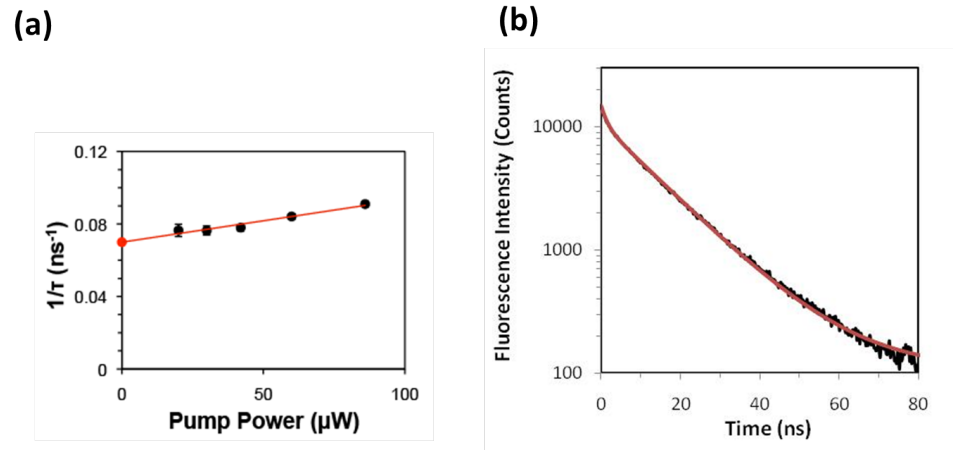

Figure 23: (a) The decay rate of the $g^{(2)}(\tau)$ spectrum measured for different excitation conditions gives the fluorescence lifetime in the limit of zero pump power [20] (for natural NV centers in this case). This extrapolation yields a lifetime of $\tau = 14.0\,\mathrm{ns}$ for this NV-nanowire system, which is slightly larger than that of bulk material ($11.8\,\mathrm{ns}$). This suggests slight suppression of emission in nanowire, consistent with our numerical model. Error bars represent $\pm 1\,\mathrm{ns}^{-1}$ standard error in the decay rate fitting parameter. **(b)** Measurement of the fluorescence lifetime via fluorescence decay is shown in black ($14\,\mu\mathrm{W}$ average pump power) for implanted NV centers. The red line corresponds to a bi-exponential fit to the fluorescence decay with time constants $\tau_{bg} = 1.5\,\mathrm{ns}$ for background fluorescence and $\tau_{NV} = 13.7\,\mathrm{ns}$ for the NV center fluorescence.

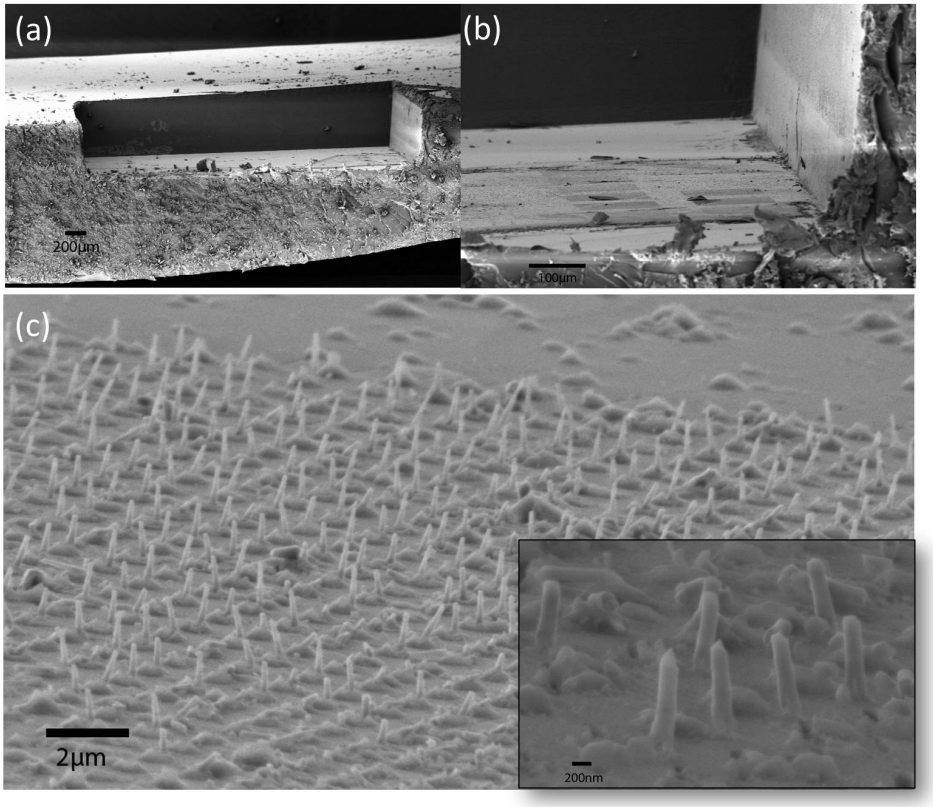

Figure 24: (a) A mould of the rectangular diamond sample is formed in epoxy. **(b)** Magnified view of the mould shows an imprint of the nanowire arrays. **(c)** An arrays of transferred nanowires in and sticking out of epoxy.

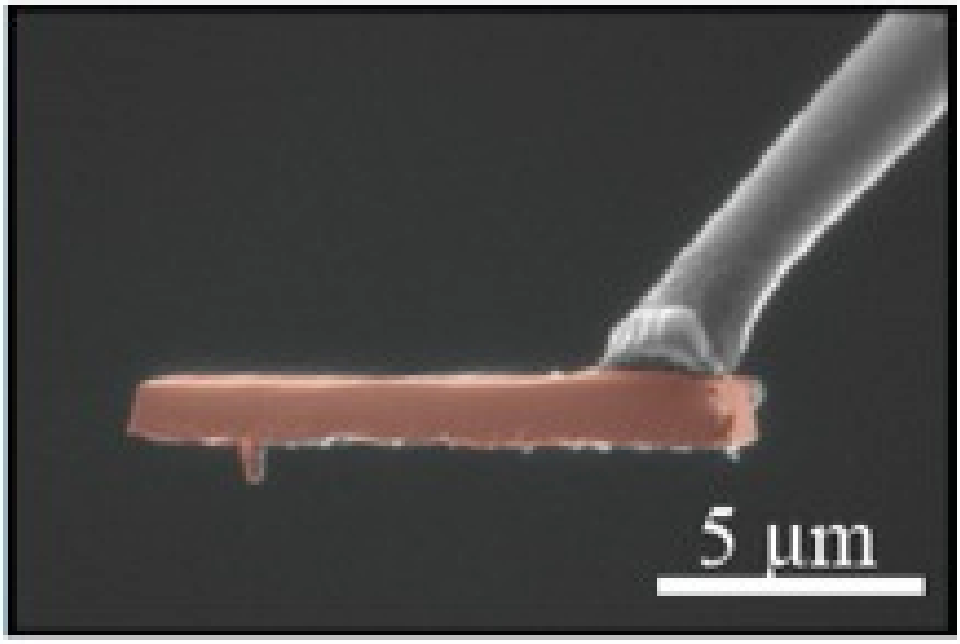

Figure 25: An all-diamond magnetometer and near-field sensor based on a diamond nanowire on a diamond cantilever (as indicated by red-colored parts) which itself is attached to an AFM tip. A shallow implanted NV center at the tip of a nanowire is used as a sensitive sensor to image magnetic fields [116].

A diamond with a flaw is worth more than a pebble without imperfections.

Chinese proverb

5

Enhanced NV center spontaneous emission in diamond-silver apertures

A complementary approach to improving the single photon yield of a solid state quantum emitter like the NV center is to enhance the photon production rate and control the NV center's emission behavior

via the Purcell effect, by coupling the color center to a host cavity. Metallic nanocavities [51] are attractive in this regard since they provide strong localization of optical modes with fairly broad bandwidths [29, 115, 155]. An interacting emitter then experiences varying degrees of modification in its spontaneous emission rate, depending on the overlap in its position, spectrum, and polarization with those of the cavity system (Sec. 2.1.2). The combination of top-down nanofabrication and ion implantation makes it possible to engineer the emitter-cavity interaction in a diamond-plasmon system for many devices in parallel [38]. Subwavelength metallic apertures containing individual color centers can be realized by fabricating arrays of diamond nanoposts on a single crystal diamond that has been implanted with a blanket layer of NV centers. The diamond nanoposts are finally embedded in a silver (Ag) film and optically addressed through the bulk diamond crystal. However, the nanostructures have been studied before and after Ag deposition. The NV center's emission is quenched in the bare posts (without silver present) leading to long lifetimes of up to 47 ns. Time-resolved photoluminescence measurements on diamond nanoposts after Ag deposition indicate that coupling to the plasmonic cavity has resulted in shortening of the emitter lifetime for single NV centers. Lifetimes as short as 2.4 ns are observed in the 90 nm implant sample, corresponding to more than a six-fold enhancement in spontaneous

emission rate in comparison to the bulk value. The enhancements in the spontaneous emission rate are accompanied by comparable increases in the single photon count rate, which is confirmed by saturation measurements.

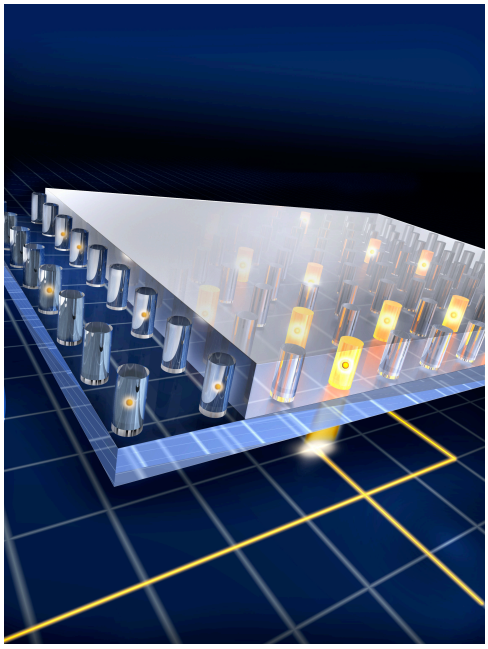

Figure 26: Cartoon of the plasmonic resonator studied in this chapter.

5.1 Design and fabrication

In this work, we present a high-yield approach to directly embed single NV centers into metallic nanostructures which leads to spontaneous emission lifetime reduction of the enclosed NV centers. Specifically, we consider plasmonic apertures (Fig. 27a), consisting of

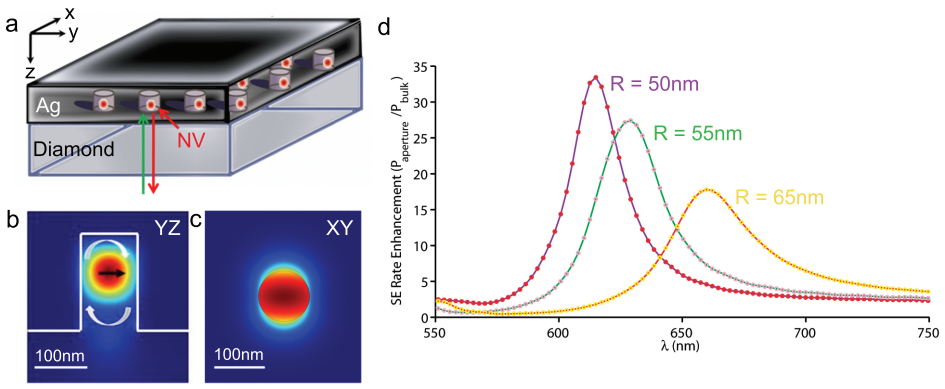

Figure 27: (a) Three-dimensional schematic of the diamond-plasmonic system. The idealized structure for coupling to the NV emission consists of a diamond nanopost (with height $180\,\mathrm{nm}$ and diameter $100\,\mathrm{nm}$) embedded in a $500\,\mathrm{nm}$-thick layer of silver (Ag). NV fluorescence is excited and collected through the bulk part of the diamond sample (green and red arrows, respectively). **(b)** Cross-sectional view of the structure along either the XZ (or YZ) plane, plotted with the longitudinal mode profile. The dipole is shown to be radially polarized and positioned in the center of the structure, where field density is maximized. As in a Fabry-Perot resonator, light reflects off the diamond-metal interfaces (curved arrows) and becomes tightly confined in the nanoposts. **(c)** Simulated lateral (XY) mode profile shows a near-uniform energy distribution of the plasmonic mode. **(d)** Simulated spontaneous emission enhancement as a function of wavelength for nanoposts with different radii, calculated by placing the dipole at the field maximum.

cylindrical diamond nanoposts (radius $r = 50\,\text{nm}$, height $h = 180\,\text{nm}$) surrounded by silver (Ag). These structures support modes with mode volumes as small as $0.07\,(\lambda/n)^3$ and can provide good spatial overlap between the highly localized optical fields and enclosed dipole due to nearly uniform field distributions in the transverse direction (Figs. 27b-c). This results in the enhancement of the spontaneous emission (SE) rate of the dipole.

The SE rate enhancements for our structures were calculated with a three-dimensional finite-difference-time-domain (3D FDTD) solver using a classical approach [29] by comparing the total power emitted from a dipole when it is placed inside the aperture to the total power emitted in a homogeneous medium. The simulations were performed with measured parameters from Johnson & Christy (1972) [92] and take into account material losses in the silver. The theoretical SE rate enhancement spectrum, plotted in figure 27d for aperture radii of $r = 50\,\text{nm}$, $r = 55\,\text{nm}$, and $r = 65\,\text{nm}$, exhibits a broad resonance that red-shifts with increasing radius and can therefore be tailored to overlap with the NV emission while keeping the height of the structure constant [29]. Based on our simulations, SE rate enhancements on the order of 30 can be expected for a radially polarized NV center placed at the maximum field intensity in an optimized structure.

The hybrid diamond-metal device, depicted in figure 27a, was realized using a combination of blanket ion implantation and

top-down nanofabrication techniques [11, 72, 73] (Fig. 28a). Two ultrapure bulk diamond crystals (type IIa, Element 6) were used for this experiment. Arrays of nanoposts used in this experiment were fabricated on the electronic grade diamond samples that were implanted with nitrogen ions (at an energy of 14 keV and a dose of $1.25 \cdot 10^{12}$ 1/cm^2 for the 20 nm-implant, and at 75 keV and $1.5 \cdot 10^{11}$ 1/cm^2 for the 90 nm-implant) and subsequently annealed under high vacuum ($< 10^{-6}$ Torr) at 750 °C (20 nm) and 800 °C (90 nm) for 2 hours to generate a layer of NV centers approximately 20 nm and 90 nm below the diamond surface. Arrays of diamond nanoposts of radii from $r = 50$ nm to $r = 70$ nm and height 180 nm were then fabricated using EBL followed by an oxygen ICP RIE (Fig. 28b). We have previously shown [73] that such a procedure can result in a high yield (>10%) of single-center devices. The nanoposts were finally embedded in a 500 nm-thick Ag film that was deposited by electron beam evaporation (Denton). For the 90 nm-implant sample, a 2 nm-thick evaporated layer of Ti was added before the Ag deposition. The thickness of the Ag layer was chosen to ensure that the diamond nanoposts were fully covered and to minimize oxidation of Ag at the device layer.

5.2 Results

In order to rigorously quantify the effect of the plasmon cavity on single NV centers, we identified bare nanoposts containing single NV centers and compared their emission properties before and after Ag deposition for the 20 nm-implant sample. These optical characterizations were performed under ambient conditions using a home-built confocal microscope with a modest numerical aperture (N.A.=0.6) and long working distance (WD=4 mm), which allowed us to optically access plasmonic nanostructures through the 500 μm-thick bulk diamond material (Fig. 28c). For the autocorrelation and saturation measurements, a continuous-wave 532nm laser was used for excitation and focused through the diamond sample onto individual posts using an air objective (Olympus LUCPlanFLN 40x, N.A. 0.6), while both the incoming and collected signals were scanned by a steering mirror (Newport). Emitted light collected by the objective passed through a dichroic mirror and was then spectrally and spatially filtered using bandpass filters (650-800nm) and a single mode fibre (2x2 coupler, Thorlabs) before being sent to avalanche photodiodes (Perkin Elmer) for photodetection and measurement of photon statistics. Spectral data were acquired using a grating spectrometer (Jobin Yvon iHR550, 76mm x 76 mm monochromator with 150 g/mm gratings).

A comparison between confocal scans taken on an array of $r = 65\,\text{nm}$ posts before (Fig. 27d) and after (Fig. 28e) Ag-deposition under identical experimental conditions indicated enhancement of light emission by the nanoposts in the presence of Ag. The nature of photon emission was then further characterized by autocorrelation measurements to determine photon statistics and triggered fluorescence decay measurements [73] to extract lifetime information.

5.2.1 Statistics on single photon emitters

For the 20 nm-implant sample, we tested a total of 65 Ag-embedded nanoposts of radii 50 nm and $r = 65\,\text{nm}$ and measured each enclosed emitter's autocorrelation function, $g^{(2)}$ (see equation 4.2) as a function of time delay, τ, in a Hanbury Brown and Twiss experiment [94]. Of these, five devices exhibited single photon character with $g^{(2)} < 0.5$ (Fig. 29, from the circled post in Fig. 28e). No background subtraction was performed in all data presented. In addition to the preservation of non-classical behavior, we observed significant narrowing of the anti-bunching dips in comparison to those taken of nanoposts prior to Ag deposition at the same excitation power (Fig. 29a), which suggests an enhancement of the spontaneous emission rate due to the plasmonic cavity. However, this comparison does not take into account possible changes in the excitation rate of the NV center due to the presence of Ag and so quantitative comparison of

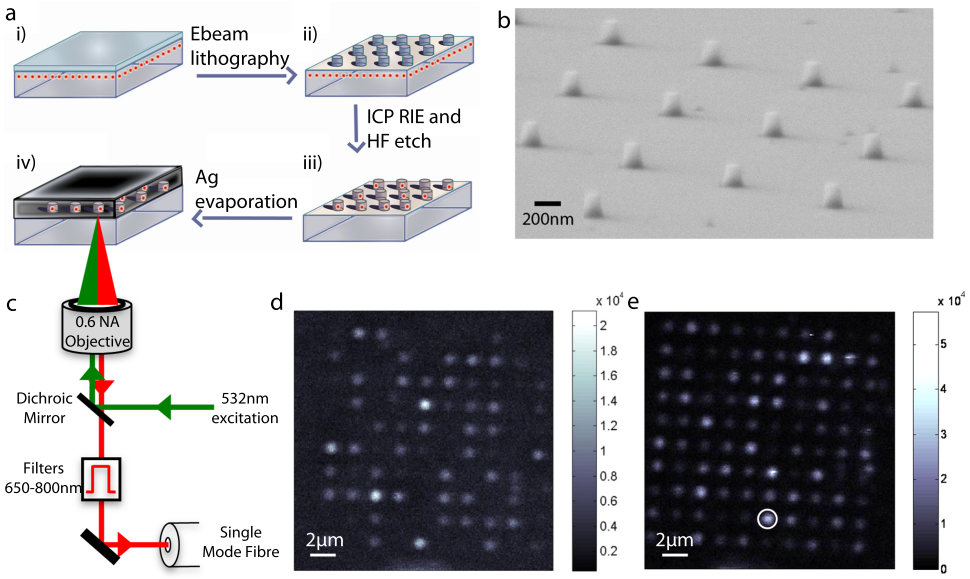

Figure 28: (a) Illustration of the fabrication procedure: (i) resist spinning on bulk diamond after nitrogen implantation and annealing, (ii) mask definition via e-beam lithography, (iii) pattern transfer to the diamond substrate in an oxygen-based RIE, and finally (iv) capping of the shallow implanted diamond posts in Ag (after resist removal). Optical characterization was performed both after step (iii) and (iv) on the same set of posts to measure the extent of plasmonic enhancement. (b) Scanning electron microscope image of a representative array of diamond posts after step (iii) in figure 28a. (c) Schematic of the experimental configuration for sample characterization. (d)-(e) Confocal microscope scans of the same array of $r = 65\,\mathrm{nm}$ posts before ((d)) and after ((e)) Ag-deposition under identical pump power. The circled post represents a plasmon-enhanced device containing a single NV center. The spacing between adjacent posts is $2\,\mu\mathrm{m}$.

the spontaneous emission rates would be later performed via lifetime measurements. Another 13 devices showed some degree of anti-bunching with $0.5 < g^{(2)} < 1$, although many of these had previously exhibited single photon emission in the absence of Ag. The reductions in $g^{(2)}$ contrast in these cases may be due to plasmon-enhanced background fluorescence from the Ag film. Indeed, this background luminescence was observed in spectrally resolved photoluminescence measurements performed on an empty aperture (without NV center). In order to improve the quality of our Ag films, we used a titanium (Ti) adhesion layer (of 2 nm thickness) between diamond and Ag in the 90 nm-implant sample.

5.2.2 Emission behavior comparison

The SE rate enhancement was investigated by time resolved photoluminescence measurements. Pulsed excitation was used to trigger an exponentially decaying fluorescence signal from which the lifetime information was extracted. Pulsed excitations were generated by passing ultrafast (200 fs) pulses at 800 nm from a Ti-Sapphire laser (Coherent) through a photonic crystal fibre (Newport). The resulting supercontinuum white light was spectrally filtered using bandpass filters between 510 and 540 nm (Semrock) to generate green pulses. For lifetime measurements requiring longer time periods between pulses, the 76 MHz repetition rate of the Ti-Sapphire pulse train was

reduced to 10.8 MHz using an electro-optic modulator (ConOptics) prior to launching into the photonic crystal fibre. All time-correlated measurements were performed using a time correlated single photon-counting module (PicoHarp).

The ensemble averaged lifetime of the densely populated NV centers in an unstructured area on the 20 nm-implant sample was measured to be 16.7 ± 0.5 ns, while the bare posts (without Ag) exhibited quenched NV emission leading to much longer lifetimes, with average values of 33.3 ± 7.5 ns for $r = 65$ nm and 38.3 ± 7.3 ns for $r = 50$ nm nanoposts containing single NV centers (Fig. 30). Additionally, the longest lifetime we measured in the bare nanoposts is 47.57 ± 1.1 ns, suggesting that such a system could be advantageous for experiments requiring prolonged excited states [63]. The increase in lifetime with decreasing post radius is due to the reduced density of states for the radiative transition as a result of the nanostructuring [34] and corroborates FDTD simulations based on measured post dimensions. Our calculations also indicate that the nanopost geometry leads to quenching of spontaneous emission for both the radial and axial components of the dipole, although the dominant contribution to the collected photons is the radial polarization. After Ag deposition, lifetimes of the NV centers implanted at 20 nm were shortened by maximum factors of 6.6 for $r = 65$ nm posts and 4.8 for $r = 50$ nm posts and were observed to be as short as 5.2 ns. For the

90 nm-implant sample, lifetimes as short as 2.4 ns were measured, corresponding to roughly a 6-fold decrease over the bulk lifetime. A comparison of fluorescence decays measured for a representative device before and after Ag deposition is shown in figure 31a. The spontaneous emission rate enhancement is accompanied by an increase in the count rates which can be observed in saturation measurements. For direct comparison, we examined one set of measurements on the same 50 nm-post before and after Ag deposition. In this case, we found that the bare and Ag-enhanced saturation intensities (and lifetimes) are $(6.1 \pm 0.2) \cdot 10^3$ cps (42.4 ± 0.8 ns) and $(4.4 \pm 0.2) \cdot 10^4$ cps (9.26 ± 0.1 ns), respectively. Therefore, the enhancements in spontaneous emission rate and fluorescence intensity are respectively 4.6 and 7.3. Since the lifetime reduction was accompanied by a comparable increase in the photon count rate, the observed plasmonic enhancement can be attributed to radiative processes. However, additional factors might be in play which led to a slight increase in the collection efficiency of the Ag-capped device, such as the out-coupling (scattering) of surface plasmon modes at the diamond/Ag interface due to the surface roughness of the metal.

In comparison to single NV centers in the bulk measured using the same low N.A. setup (data not shown), the measured saturation intensities are roughly 2-3 times higher, with the best 20 nm-implant

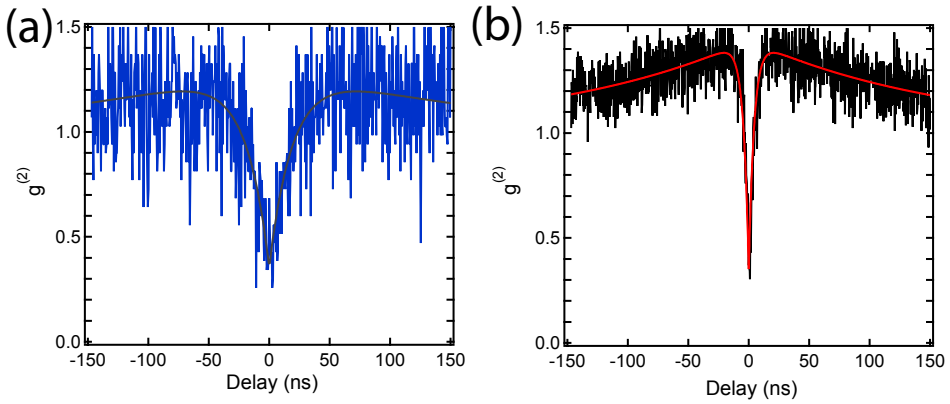

Figure 29: Autocorrelation function for a **(a)** representative bare nanopost and **(b)** Ag-embedded device (circled in figure 28d) reveal strong anti-bunching at zero time delay indicating the emission of non-classical light. No background subtraction was performed. The gray and red curves represent fits to the g(2) function [101].

diamond-plasmon device (Fig. 31b) saturating at $(1.01 \pm 0.02) \cdot 10^5$ cps at a saturation power of 1.18 ± 0.06 mW. In general, saturation measurements were difficult to carry out in the shallow-implanted nanoposts, as photo-ionization of the NV centers could occur at high excitation powers ($P > 2$ mW), so that the saturation intensities could only be inferred from fitting to the saturation model. In addition to TIR at the diamond-air interface, photon losses in the system can be attributed to the coupling of emitted photons to surface plasmons which propagate laterally on the diamond-silver surface and could not be collected. Indeed, FDTD calculations show that only 4-5% of the emitted photons are captured by the collection optics, which suggests that further structure optimizations, such as the addition of gratings, might be necessary to increase the number of collected photons [29].

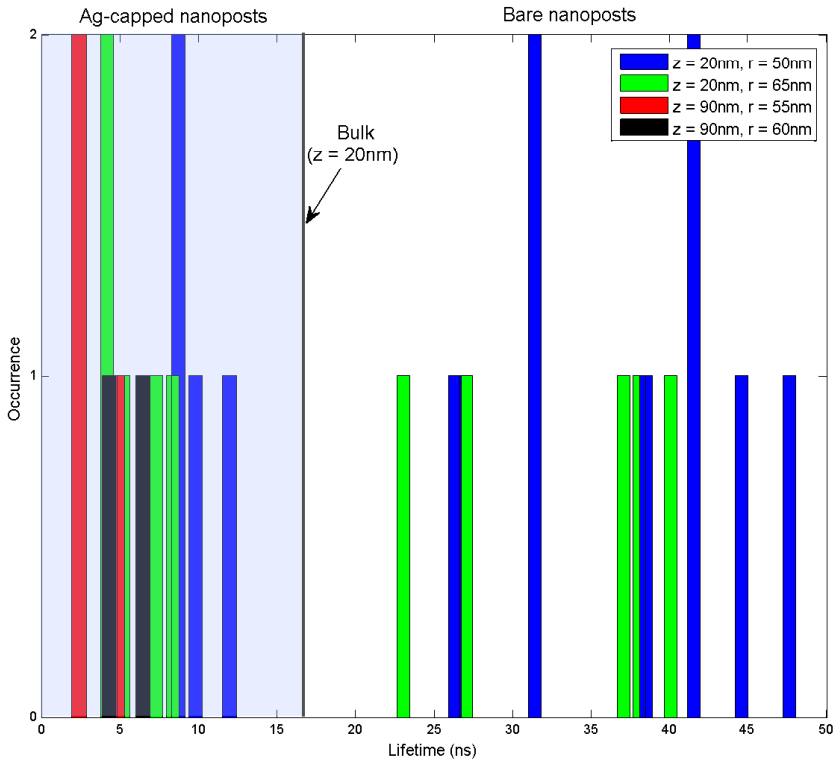

Figure 30: Histogram of NV center lifetimes for nanoposts of different radii (r) and implantation depths (z) before and after Ag deposition. The shaded region represents data points for Ag-capped posts, while the measured bulk lifetime for NV centers implanted $20\,\mathrm{nm}$ below the diamond surface is denoted with a gray line. The quenching of light emission in the bare nanoposts is due to the reduced density of states in the nanostructures.

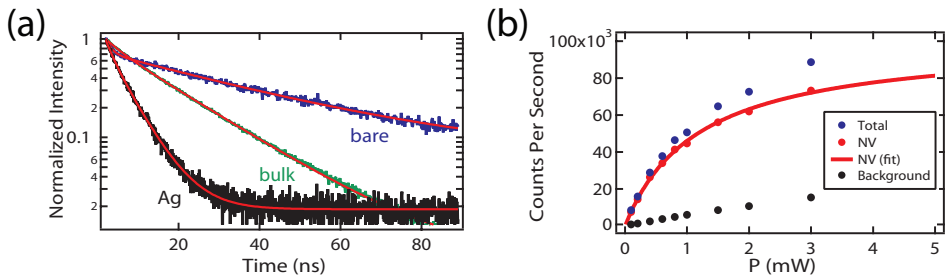

Figure 31: (a) Normalized fluorescence decays for the same $r = 65\,\mathrm{nm}$ nanopost, containing a single NV center, before and after Ag-deposition and for an ensemble population of NV centers in the bulk region, along with fits to a multi-exponential model (shown in red). The fits yielded time constants for fast-decaying background fluorescence ($< 2\,\mathrm{ns}$) as well as a slower NV photoluminescence (bare: $37.17 \pm 0.7\,\mathrm{ns}$; Ag-embedded: $5.65 \pm 0.08\,\mathrm{ns}$; bulk: $16.7 \pm 0.08\,\mathrm{ns}$). **(b)** Saturation curve for a Ag-embedded nanopost with an NV center implanted at $20\,\mathrm{nm}$. The total count rates are represented by blue, while the background contributions (as measured from an empty post without any NV centers) are denoted black dots. Subtraction of the background from the total yields the NV emission (red dots), which can be fitted to the saturation model (solid line). The fitted saturation intensity and power are $(1.01 \pm 0.02) \cdot 10^5\,\mathrm{cps}$ and $1.18 \pm 0.06\,\mathrm{mW}$.

Photoluminescence (PL) spectra taken of the Ag-embedded nanoposts consisted of the NV photoluminescence and the first and second order Raman signals of diamond (not shown). Resonance peaks could be observed after subtracting the background PL (from an empty post) from the plasmon-enhanced NV center PL spectrum. For the 90 nm-implanted nanoposts shown in figure 32, the quality factors are 10, with central peak wavelengths red-shifting from 665.5 nm to 718.9 nm with increasing radius from 50 nm to 70 nm. The dispersion in resonances between similarly-sized posts ($r = 55$ nm) can be explained by the sensitivity of the resonance to nanoscale deviations in the dimensions of different devices (Fig. 27d).

Finally, while their optical spectra have been modified, the observed fluorescence was unequivocally assigned to NV center emission using room temperature, optically detected electron spin resonance (ESR) measurements [69]. ESR measurements were performed using a confocal microscope with a 0.8 N.A. objective. Microwaves were applied using a semirigid coaxial cable which was shorted with a 25 μm-diameter Au bonding wire loop. The Au wire was approached from the bottom side of the sample in close proximity of the Ag film ($30 - 40\,\mu$m distance). Bulk Ag has a skin-depth of 1.2 μm at 2.8 GHz and our 500 nm Ag film is therefore largely transparent to the applied RF field. Additionally, the reduced conductivity of the evaporated Ag film further enhances its transparency to microwaves. A Rohde

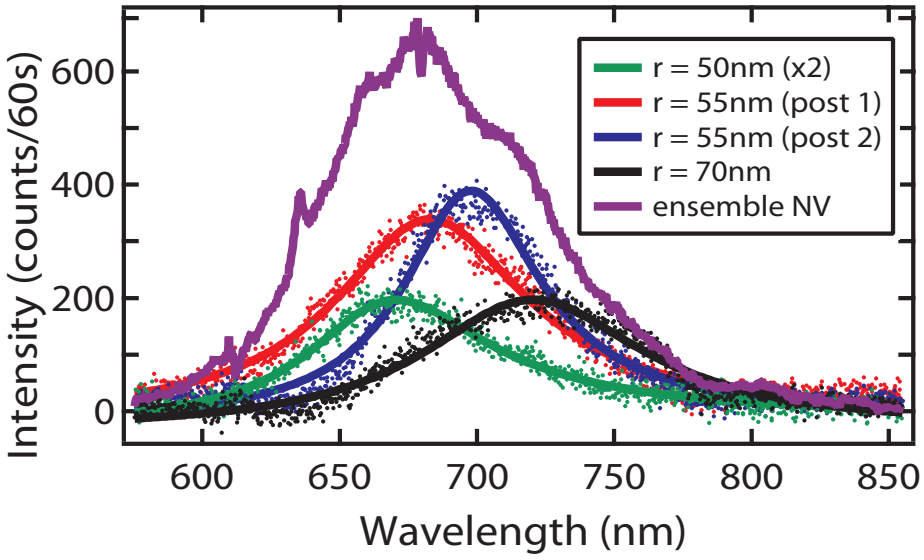

Figure 32: Background-subtracted spectra for four different devices in the $90\,\mathrm{nm}$-implant sample, along with a reference NV center spectrum taken from an ensemble of NV centers in a Ag-covered, unstructured region of the sample. Each solid line represents the fit to the raw data (dots). The $r = 50\,\mathrm{nm}$ nanopost was integrated for twice as long ($120\,\mathrm{s}$). The quality factors corresponding to the fits are roughly between 7 (black curve) and 11 (blue curve), while the resonance peaks range from $665.5\,\mathrm{nm}$ ($r = 50\,\mathrm{nm}$ post) and $718.9\,\mathrm{nm}$ ($r = 70\,\mathrm{nm}$ post).

Schwarz SMB 100A microwave generator was used and the signal was amplified with a 30 dB gain in a Minicircuits ZHL-42W.

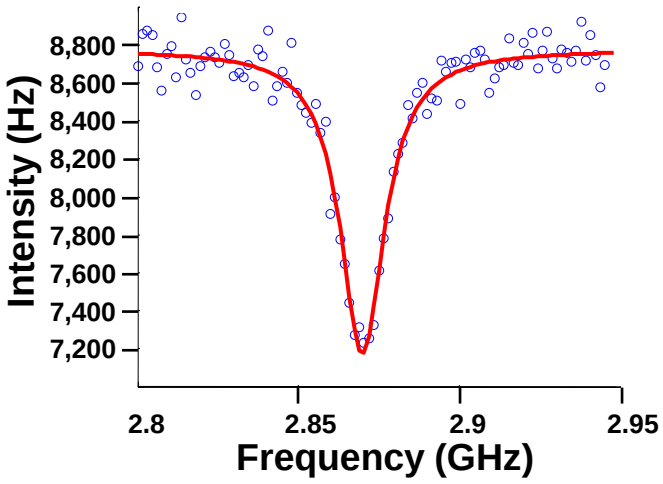

Figure 33: Optically detected magnetic resonance (ODMR) spectrum of a plasmon-enhanced NV center, measured by tuning the microwave source over the NV center splitting between the $m_s = 0$ and $m_s = \pm 1$ ground state levels without an external magnetic field. The spectrum reveals a characteristic dip at 2.87 GHz and a contrast of 18.3%.

We observed a typical NV-ESR spectrum (Fig. 33) with a dip in fluorescence at an applied microwave frequency of 2.87 GHz. The characteristic signature corresponds to the zero-field ground-state splitting between the $m_s = 0$ and $m_s = \pm 1$ states (Fig. 1b). Optical excitation from the $m_s = \pm 1$ state couples more strongly to the long-lived singlet shelving state and undergoes fewer fluorescence cycles before doing so. Hence, it fluoresces 20-40% less initially [69], [89]. The observed fluorescence contrast of 18.3% represents a

preservation of contrast compared to measurements on bulk NV centers which suggests the viability of spin systems based on plasmon-enhanced NV emission, a critical property for both quantum information and magnetometry is spin coherence, which will have to be addressed in future experiments. From the contrast in the ESR dip, one can deduce the average spin polarization populations. However, the spin coherence time can generally be extended substantially using dynamical decoupling techniques [42]. Furthermore, ESR techniques allow for electron spin quantum state read-out [181]. Single-shot read-out measurements have been achieved on an NV center's nuclear spin [130] as well as on a multi quantum bit register consisting of an NV center and nearby Nitrogen atoms [148].

5.2.3 Overall performance

To illustrate the overall performance improvement, we have plotted the saturation intensity against the lifetime for a number of devices in the bare and Ag-capped cases at the two implantation depths. Figure 34 shows a significant decrease in the lifetimes of the Ag-capped devices accompanied by an enhancement in photon emission. For our best 20 nm-deep device, the Purcell enhancement is 6.4 and 3.2 when compared to average lifetimes in the bare nanopost and unstructured shallow implanted NV centers, respectively. We have also modeled the fabricated devices using dimensions obtained from SEM imaging. In

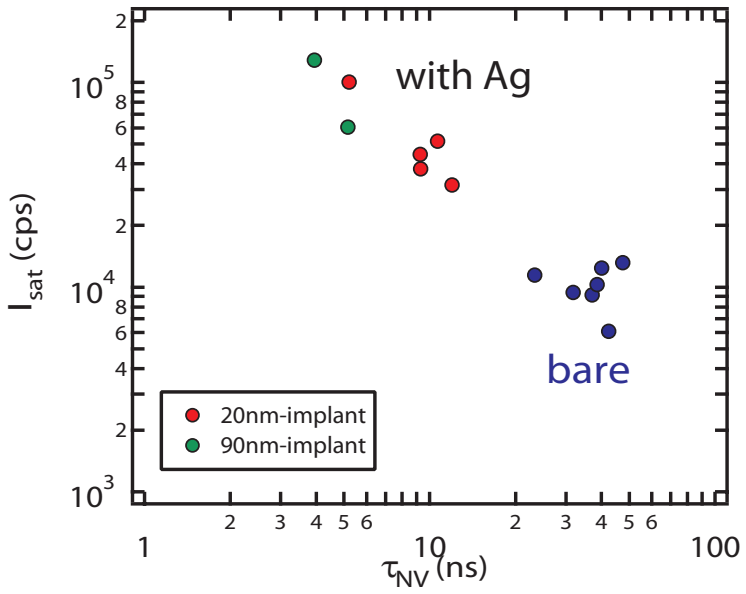

Figure 34: Performance plot of saturation intensity as a function of fluorescence lifetime for the bare and Ag-capped devices we tested for this study, showing that the plasmonic enhancement provided by the geometry has led to shorter lifetimes and correspondingly higher count rates.

addition to the geometry (i.e. truncated conical shapes of the finished devices), the modeling took into account the implantation depth and straggle, as well as the ambiguity in the polarization angle of the dipole moment arising from phonon mixing due to the [100] orientation of the diamond crystal plane [62]. From these considerations, we determined the spectrally averaged minima and maxima of the SE rate enhancements in the 20 nm-implant sample to be 2 and 3.6 in comparison to the bulk (shallow-implanted), showing a good convergence with experimental values. Moreover, the degree of SE enhancement is maximized when the dipole is placed at the center of the aperture and drops off as its axial position deviates from the field maximum and so larger Purcell enhancements (Fig. 27d) are anticipated with optimized implantation depth. Indeed, devices on the 90 nm-implant sample show that the NV center lifetime can be shortened to 2.4 ns, which is roughly a six-fold decrease over bulk values. Finally, modified device designs [29] will allow for collimated emission resulting in larger collection efficiencies of emitted photons. The method presented here provides controlled coupling in a quantum emitter-plasmonic resonator system, for a large number of devices in parallel, and has yielded Purcell-enhanced single photon emission of NV centers. In comparison to existing bottom-up approaches, our geometry is scalable and can be implemented without alignment-sensitive procedures. Such diamond-plasmon devices can

therefore serve as a basis and proof of principle for more complex diamond-plasmon structures9 that can potentially provide stable and reliable systems for demonstrating enhanced zero-phonon line (ZPL) of the NV center, long-range coupling between qubits via surface plasmons [66], and improved optical readouts for single spin states.

Diamonds are a girl's best friend.

Jules Styne

6

Coupling NV centers to integrated diamond ring resonators

Diamond nanowires and diamond-silver apertures discussed above are particularly suitable for applications where single photons are extracted from the chip and coupled to free-space optics. However, for

many applications, including the realization of scalable quantum networks it is of interest to keep the photons on-chip and use them to carry information from one part of the system to another. For these applications it is of great interest to develop a fully integrated diamond photonic platform which can be achieved by the generation of a single crystal diamond-on-insulator material system. In this chapter, we demonstrate an integrated nanophotonic network in diamond, consisting of a ring resonator coupled to an optical waveguide with grating in- and outcouplers. NV centers embedded inside the ring resonator are used as a source of photons, single photon generation and routing at room temperature is observed. Furthermore, we observe a large overall photon extraction efficiency (10%) and high quality factors of ring resonators (3,200 for waveguide-coupled system and 12,600 for a bare ring).

6.1 Diamond ring resonators as representative planar network

6.1.1 Fabrication

Our approach involves the fabrication of high quality, low loss ring resonators directly in SCD thin slabs (type Ib, Element Six) and follows the approach presented in chapter 3.2.2. Here, high-quality single-crystal thin slabs $< 50\,\mu$m are placed on a low-index substrate,

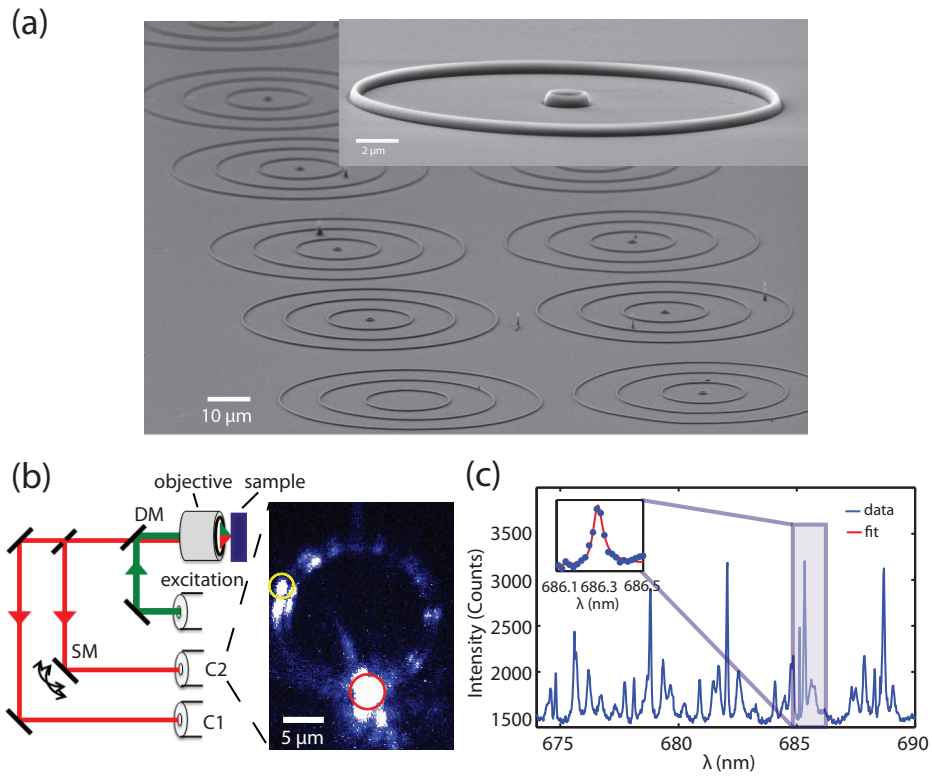

Figure 35: **(a)** The SEM image shows diamond ring resonators on $\mathrm{SiO_2/Si}$ with varying radii. Inset: Higher magnification image of two ring resonators with smooth sidewalls. **(b)** Schematic of a two collection arm confocal microscope. Having obtained a scan of the device using collection arm C_1 we fix the green pump beam (red circle) and use collection arm C_2 to obtain a second scan and collect photons from a different position at the ring resonator (yellow circle). The yellow circle also marks the collection position while taking spectra. **(c)** The photoluminescence spectrum features peaks that correspond to the modes of the resonator. A pump power of $1.5\,\mathrm{mW}$ is used at an integration time of $300\,\mathrm{s}$. Inset: A Q-factor of $(12.6 \pm 1) \cdot 10^3$ is obtained by fitting the experimental data (red).

such as silica, and thinned, to form an optically thin diamond waveguide slab that confines light by means of total internal reflection. Figure 35a shows a scanning electron microscope (SEM) image of representative diamond ring resonators, with different diameter and ring cross-sectional dimensions, on SiO_2/Si substrate. As mentioned in chapter 3 this versatile approach allows for a variety of nanophotonic devices and systems to be made in diamond, including ring resonators [55, 76] and photonic crystal cavities [56, 75].

6.1.2 Simulations

We use three-dimensional 3-D FDTD code (Lumerical) to model our devices, and to estimate the coupling efficiency between the NV center and the ring resonator, the resonator and the waveguide, and the outcoupling efficiency of the gratings. We infer a grating outcoupling efficiency towards the collection optics (0.95 numerical aperture objective) of 30 % compared to 20 % in the case of an abrupt waveguide end. In our modeling, we assume a 5 μm diameter ring resonator with a 250 nm x 250 nm cross-section which is close to the experimental values. The distance between ring and waveguide is assumed to be 50 nm. The NV center is modeled as a dipole polarized along radial direction with respect to the ring and routed fields are observed (Fig. 36). We find that 15 % of the overall dipole emission is routed to and up-scattered at both grating couplers combined for

wavelengths on resonance. Furthermore, we find that gratings also scatter 30 % of the overall dipole emission towards the substrate (fraction of which can get reflected back at the SiO_2/Si interface). Finally no more than 7 % of light is transmitted through the grating. The mode volume of the ring resonator is obtained using

$$V = \frac{\int \epsilon(r) \left|E(r)\right|^2 d^3r}{\max(\epsilon(r) \left|E(r)\right|^2)} \approx 28 \cdot (\frac{\lambda}{n_{diam}})^3.$$

assuming that the dipole is placed in the field maximum with optimal polarization (aligned with the E-field of the cavity mode).

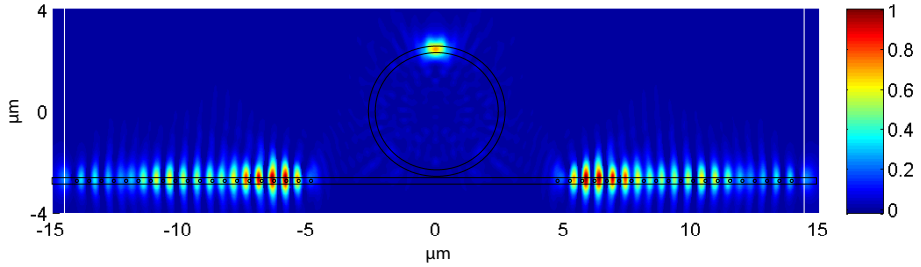

Figure 36: FDTD simulations were used to model the routed fields. We obtain the up-scattering Poynting vector when the photon source is in resonance with the ring resonator. The dipole source is placed in-plane and at the field maximum in the ring, oriented along the radial direction.

6.1.3 Characterization of bare rings

In order to characterize our diamond resonators we take advantage of the intrinsic fluorescence of embedded color centers. We use a photoluminescence approach in a scanning confocal microscope using

two collection arms [6](Fig. 35b). The light that propagates to collection arm C1 is used to obtain a scan of the device, and find the position of an NV center. The pump beam is then placed at a fixed position and $\approx 50\%$ of the emitted light is directed towards collection arm C2 via a beam splitter while a scanning mirror delivers a second confocal micrograph. The second scan reveals out - scattered light from light coupled to the device. To obtain the spectrum of luminescence signal, we use grating spectrometers (HORIBA Jobin Yvon, iHR550 and Acton SpectraPro SP300i) equipped with a sensitive charged coupled device (Synapse CCD) detector.

As mentioned before, one channel of the two-collection arm confocal microscope collects at the excitation spot whereas the second arm can collect independently from the first one at a different spot. Green pump light (532 nm) scans the devices at normal incidence (Fig. 35b) via a scanning mirror, and red photons (650 nm-800 nm) emitted from NV centers are collected and analyzed after passing through a dichroic mirror (DM) and longpass filters. Our detection path is split into two arms, one of which is always fixed at the excitation spot (C1) while the second arm can be scanned independently (C2). The latter allows us to spatially separate excitation and collection positions. First, we scan the sample to obtain an emission image of the device using C1. Figure 35b(right), shows a scan of the photon collection position over the ring in C2 (yellow circle) while constantly exciting with the pump

laser in the same position (red circle). The device shown in the figure has an outer ring radius of 20μm and a 1μm $\times$ 410 nm cross-section with 300 nm XR covering the diamond. The intensity profile of the ring indicates excitation of a higher order mode (confirmed by 3-D finite difference time domain (FDTD) simulations, not shown). The spectrum reveals multimode behavior of the cavity with quality (Q) factors of Q $\approx 12,600$ and a finesse F of 62 (Fig. 35c and inset).

6.1.4 Single photon routing on chip

To form a node of a network it is necessary to integrate the ring resonator with a channel that carries information. We monolithically fabricate ring resonators next to optical waveguides and thereby provide efficient and robust in- and outcoupling of light to the resonator with embedded single NV centers. For a more detailed introduction to waveguide coupled ring resonators please refer to chapter 8. The waveguides contain second order gratings on each end to facilitate free-space coupling of photons (Fig. 37a). We characterize the structure by coupling the light from a broadband white light source into one grating and by collecting transmitted light from the other grating. The transmission spectrum shows regularly spaced dips corresponding to the different (longitudinal) resonant modes of the ring resonator (Fig. 37b). We extract a Q-factor of Q ≈ 2500 and F ≈ 40 for the resonance at $\lambda = 689.8$ nm. Here, we

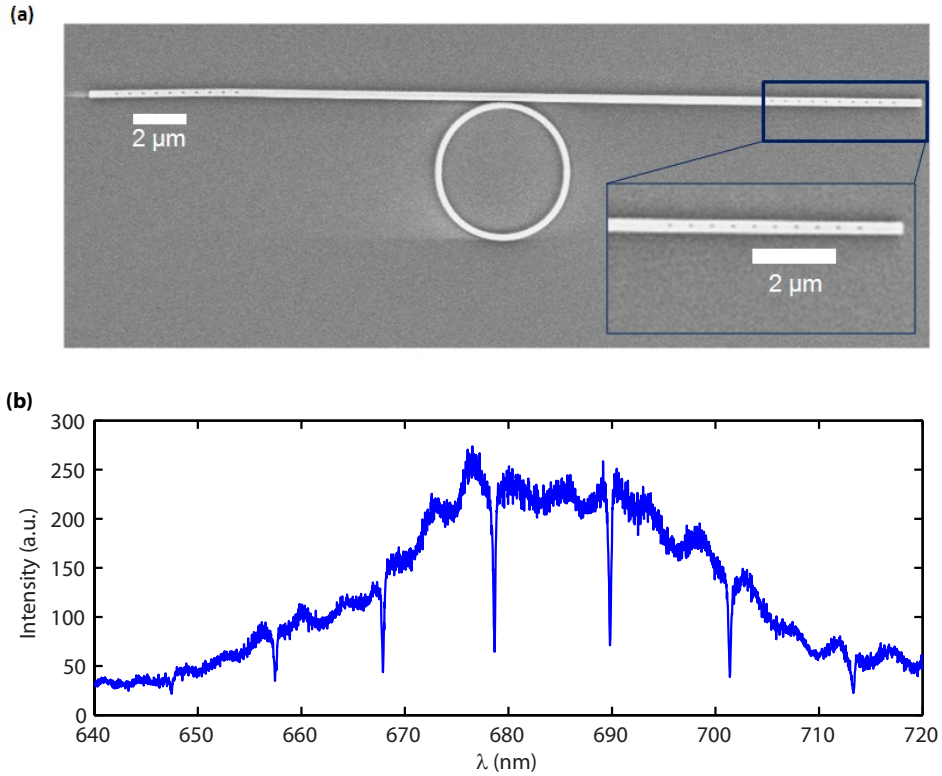

Figure 37: (a) SEM image of a single mode ring resonator coupled to a waveguide containing second order gratings on both ends. The ring diameter is $5\,\mu\mathrm{m}$ and its width is $245\,\mathrm{nm}$. The gap between the waveguide and the ring is $100\,\mathrm{nm}$, while the waveguide itself has a width of $370\,\mathrm{nm}$. The device is sitting on a SiO_2/Si substrate. Inset: Magnified image of the grating region. **(b)** The transmission spectrum is obtained by exciting the structure with white light (from super-continuum source) using the right-hand side grating, and measuring transmitted signal using the left-hand side grating. The dips in the transmission correspond to the ring resonator modes.

operate close to critical coupling where the decay rate to the waveguide would equal the intrinsic field decay rate of the resonator.

Additionally, we demonstrate efficient generation and routing of nonclassical light fields provided by a single NV center embedded inside the diamond ring resonator, at room temperature. Single photons emitted from the NV center into the ring resonator couple evanescently to the waveguide and are outcoupled one by one by the gratings. Figure 38a) and b) illustrate scans using the two confocal collection channels C1 and C2, respectively (the device is different from the one shown in Fig. 37). After scanning, the green pump laser (as well as the first collection channel) is placed at the NV center (indicated by the red circle in Fig. 38a) and b)) and the second arm C_2 is either placed at the NV center (denoted C_{21}) or at the grating couplers at the end of the waveguides (C_{22} for the coupler on the left, and C_{23} for the one on the right). Collection arm C_1, positioned above the NV center, is used to collect photons emitted directly by the NV center - denoted by C_{11}. We use Hanbury Brown and Twiss (HBT) configuration [28] to evaluate the second-order intensity correlations $g^{(2)}(\tau)$ (see equation 4.2), where nonclassical light behavior from a single quantum emitter results in $g^{(2)}(0) < 0.5$ [94]. First we study the free-space emission of the NV center (Fig. 38d). Here, light is directly emitted upwards and extracted at the pump position in each

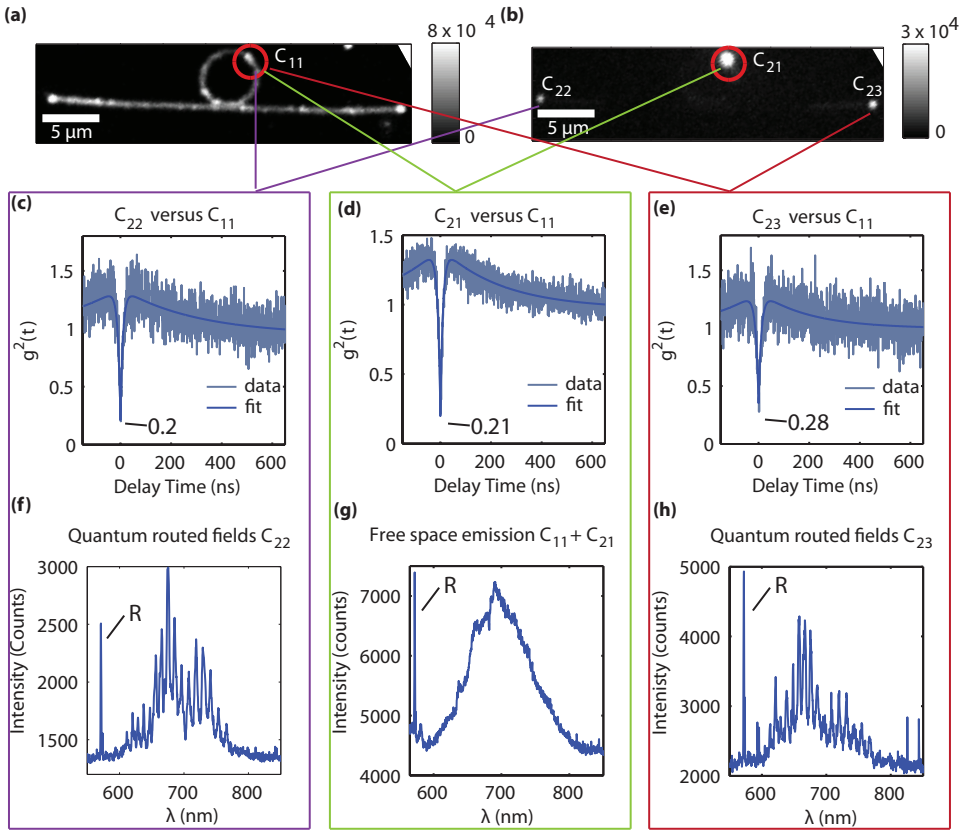

Figure 38: (a) Confocal image of the device is obtained by scanning the pump laser and using collection arm C1 to collect the fluorescence (see also figure 35). After presence of NV center is confirmed, we position the pump beam at its location. **(b)** Second confocal image can then be acquired using the collection arm C2. Furthermore, C2 arm can be used to collect light from three locations of interest: NV center position (C_{21}), left hand side grating (C_{22}) and right hand side grating (C_{23}). **(c-e)** Hanbury-Brown-Twiss apparatus confirms emission and routing of nonclassical light, by cross correlating signals C_{11} with C_{21} as well as C_{23} and C_{22}. Strong anti-bunching ($g^{(2)}(0) < 0.5$) is observed, without any background subtraction. **(g)** The combined spectrum of C_{11} and C_{21} shows the characteristic NV emission. The exact same position of the (non-broadened) Raman line at $573\,\mathrm{nm}$ as in the bulk diamond indicates that the single crystal diamond film quality is comparable to bulk diamond (denoted by R). **(f), (h)** Spectra collected from the gratings C_{22}, C_{23}, respectively, reveal resonances of the ring imprinted on the phonon sideband of the NV center's emission (using a 150 lines/mm grating). We obtain a Q-value of $(3.2 \pm 0.4) \cdot 10^3$ for the resonance at $665.9\,\mathrm{nm}$ using a large resolution grating (1800 lines/mm).

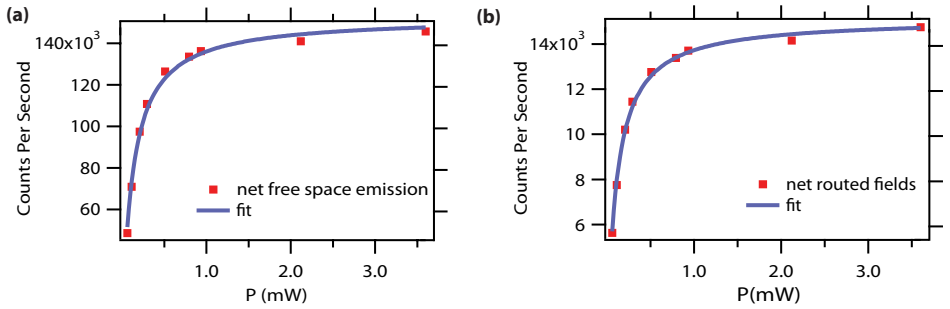

Figure 39: (a) Free-space collection exhibits a saturated single photon flux of $(15 \pm 0.2) \cdot 10^4$CPS at a pump power of $120 \pm 7\,\mu$W from an NV center. The net counts from a single NV center are obtained via subtracting the linear background from the overall count rate. **(b)** The combined count rate at both gratings gives a saturation level of $(15 \pm 0.1) \cdot 10^3$ CPS at a saturation pump power of $(100 \pm 4)\,\mu$W.

collection position (C_{11} and C_{21}). The cross-correlation between C_{11} and C_{21} shows strong photon antibunching demonstrating the single photon character of the emitted quantum field. The increased coincidence rate for $12\,\text{ns} < \tau < 550\,\text{ns}$ is attributed to an intermediate shelving state, characteristic of an NV center's emission [101]. For all $g^{(2)}$-measurements no background subtraction was performed revealing a good contrast even in a type Ib diamond. This type of diamond usually has a high background level that is absent here since our diamond thinning process has led to removal of large amount of background originating from e.g. nearby NV centers, that would normally make such $g^{(2)}$-measurements difficult in the bulk.

When collecting photons emitted directly above the NV center (combining C_{11} and C_{21}) we observe the typical NV center's emission spectrum (Fig. 38g) where the majority of collected photons are

emitted directly into the free-space without coupling into the ring modes. Furthermore, the Raman line occurs at the same spectral position (573 nm) as in bulk diamond, indicating a good film quality (Fig. 38, as denoted by R in all spectra). The spectra at the outcoupling gratings (Fig. 38f and 38h) feature prominent peaks indicating coupling of the NV center's fluorescence to the modes of the ring resonator as well as transfer of emitted photons into the waveguide. Based on this fluorescence spectrum we measure loaded Q-factors as high as $(3.2 \pm 0.4) \cdot 10^3$ at 665.9 nm. Moreover, we observe the evidence of routing of the quantum light field when we cross-correlate C_{11} with C_{22} and C_{23}. We confirm strong photon antibunching without significant change of the light statistics compared to the auto-correlated free-space emission (Fig. 38 c) and 38 e), respectively).

Finally, we evaluate the performance of the routing process by comparing the saturation behavior of the NV center emission into free space with its emission into the photonic structure (Fig. 39). We obtain the net count rate by subtracting the background (linearly increasing with pump power) from the overall counts and fit according to equation 4.3. The free space emission of the NV center, obtained by adding C_{11} and C_{21}, saturates at a count level of $(15 \pm 0.2) \cdot 10^4$ counts per seconds (CPS) at a pump power of $(120 \pm 7)\mu$W. This saturation level is significantly higher when compared to an NV center

in bulk which we attribute to a thin film effect [105] combined with the NV center's polarization-dependent coupling to the ring. At the same time, the combined counts from the outcoupling gratings give $(15 \pm 0.1) \cdot 10^3$ CPS at saturation at a pump power of $(100 \pm 4)\mu$W. As mentioned before, using 3-D FDTD modeling we estimated the overall collection efficiency of our current grating design to be 30%. In addition, by modeling the coupling efficiency from the NV center to the ring and from the ring to the waveguide we estimate a total collection efficiency of our system to be 15% - that is 15% of photons emitted by an NV center are outcoupled by the gratings and collected using our collection optics. We note that reduced photon counts collected from gratings are largely due to the confocal nature of our experimental apparatus which collects light only from a small ($< 1\mu\text{m}^2$) region of the grating. The collection from the gratings could be significantly improved if light from the whole grating regions is collected using a multimode fiber or an objective lens. Improvements in the design of the gratings themselves can increase the collection efficiency up to 90% [102]. Finally, inverse-taper waveguide outcoupling [7, 159] could be used to efficiently collect most of the emitted light directly from the waveguide, without a need for a grating.

6.1.5 Conclusion and outlook

Our first demonstration of an integrated on-chip optical network based on diamond illustrates the great potential of a diamond-on-insulator platform in the field of quantum optics. The compact architecture and low loss material make our diamond platform suitable for large scale integration where multiple devices can be connected via single photon channels, thus enabling on-chip photonic networks. With the recent progress of spin-photon entanglement with single NV centers [19, 166] our approach may pave the way for the realization of integrated, scalable quantum networks [93] in which photons are used to transfer quantum information between different nodes (e.g. NV center embedded inside cavity) of the network. Due to their long spin coherence times at room temperature, NV centers are not only promising candidates for quantum memory, but also have intriguing applications in quantum sensing [13, 116, 121]. In order to enhance the interaction between light and an NV center, and possibly enter the strong-coupling regime of light-matter interaction, photonic crystal cavities fabricated directly in diamond will be explored in the next chapter. Besides other applications, entering the strong coupling regime could be applied to realize single photon transistors [32, 86] based on diamond.

You can focus on things that are barriers or you can focus on scaling the wall or redefining the problem.

Tim Cook

7

NV centers coupled to photonic crystal cavities

The realization of efficient optical interfaces for solid-state atom-like systems is an important problem in quantum science with potential applications in quantum communications and quantum information

processing. We describe and demonstrate a technique for coupling single NV centers to suspended diamond photonic crystal cavities with quality factors of up to 6,000. Specifically, we present an enhancement of the NV center's zero-phonon line fluorescence by a factor of 7 in low temperature measurements. Potential applications of this technique are discussed.

7.1 Introduction to photonic crystal cavities

7.1.1 History

A Bragg stack consisting of alternating media with different refractive indices has been studied widely as predecessor of the PCC since Lord Rayleigh. For instance, the use of a distributed Bragg reflector has been implemented in a 1D structure known as vertical-cavity surface-emitting laser (VCSEL) since 1979 [162]. However, it was not until 1987 when Eli Yablonovitch at Bell labs proposed a gedankenexperiment of forming a Fabry Perot cavity for a dipole emitter in a 3D photonic crystal [183]. He stated, that when a band gap is formed for light by a 3D periodic lattice of dielectric, and overlapping with the electronic one, the spontaneous emission of a dipole emitter can be inhibited. At the same time, Sajeev John proposed strong localization of photons in a "disordered superlattice microstructures of sufficiently high dielectric contrast " [91]. He

realized that there are extended and localized states for light in a band diagram. These two papers mark the beginning of photonic crystal cavities and their interpretation as periodic lattice providing a band diagram with photonic band gap for light, equivalent to band diagrams for electrons as formed by the atomic lattices in a solid state.

Since then, PCCs have been studied extensively and have shown to be compatible with the integration of quantum dots and color centers to form a solid state platform for strong light matter interactions and hence a playground for cavity electrodynamics (cQED). Photonic crystals and PCCs have also found use in (chemical) sensing, fibers, lasers, nonlinear frequency conversion etc. In 1997, the first photonic crystal nano-beam cavity mode in a photonic band gap was demonstrated in Si at telecom wavelength [58]. Being beyond the scope of this thesis, only a brief introduction to photonic crystal nano beam cavities is provided.

7.1.2 Motivation for photonic crystal cavities as building blocks of integrated photonic networks

The integration of solid state quantum emitters with sub-wavelength-scale optical devices has generated substantial interest in chip-based quantum networks [93]. As discussed earlier, NV center in diamond is an exceptional candidate for a quantum bit due to its spin readout and manipulation capabilities, which combined with long

coherence times can be leveraged for quantum information science [129, 132, 181, 186], quantum sensing [13, 121] and quantum networks [21, 36]. These potential applications all either require or benefit from optimized collection efficiency as well as control of spectral and spatial properties of spontaneously emitted photons.

An appealing approach to addressing these problems involves the use of Cavity Quantum Electrodynamics (CQED). Here, the single photon spontaneous emission rate can be controlled by a photonic cavity that enhances the interaction strength between a single optical mode and the NV center. In the case of the NV center, these benefits can be realized by cavity coupling to the narrow-band ZPL transition, which constitutes 3-5% of photoluminescent emission (PLE) from the excited state. Indeed, many applications in quantum science rely on the interference between indistinguishable photons, for which only the ZPL transition is suitable. Coupling to an optical cavity thus provides a means to enhance both the ZPL collection efficiency and the relative proportion of photons emitted into the ZPL. In particular, PCCs, schematically depicted in figure 41a, provide a strong enhancement due to their small mode volumes and have been studied widely in the context of light-matter interactions with quantum dots [145, 185].

Coupling between NV centers and PCCs has been demonstrated in several different systems. In hybrid systems, where a diamond nanocrystal containing an NV center is placed in the cavity mode of a

photonic crystal fabricated from another material, coupling to single NV centers has been shown first for 2D semiconductor PCCs made from GaP [53] and later in 1D plasmonic PCCs based on silver nanowires [43]. Although substantial enhancement has been demonstrated in such systems, the NV centers in nanocrystalline diamond exhibited poor optical qualities. This necessitates the use of bulk diamond. In this vein, coupling between PCCs and ensembles of NV centers or silicon-vacancy centers has been demonstrated in devices fabricated by focused ion beam milling of single-crystal bulk diamond [146]. Additionally, advances in diamond fabrication technology allowed for high quality cavities to be made via reactive ion etching (RIE) techniques. Coupling to individual centers in such devices was achieved first in microring resonators [55, 76] and in 2D PCCs [56].

In this work, we extend these results to include suspended, 1D PCCs fabricated by RIE from high purity single-crystal diamond films [77]. The 1D geometry lends itself easily to integration with chip-based networks via coupling to diamond ridge waveguide modes. We have measured quality (Q) factors up to 6000 in our devices, and we demonstrate both red tuning up to 7 nm by Xe deposition and blue tuning up to 23 nm by baking and plasma etching. Finally, we show enhancement of the ZPL of a single NV center by a factor of 7 at low temperature.

7.2 Photonic Crystal Design & Fabrication

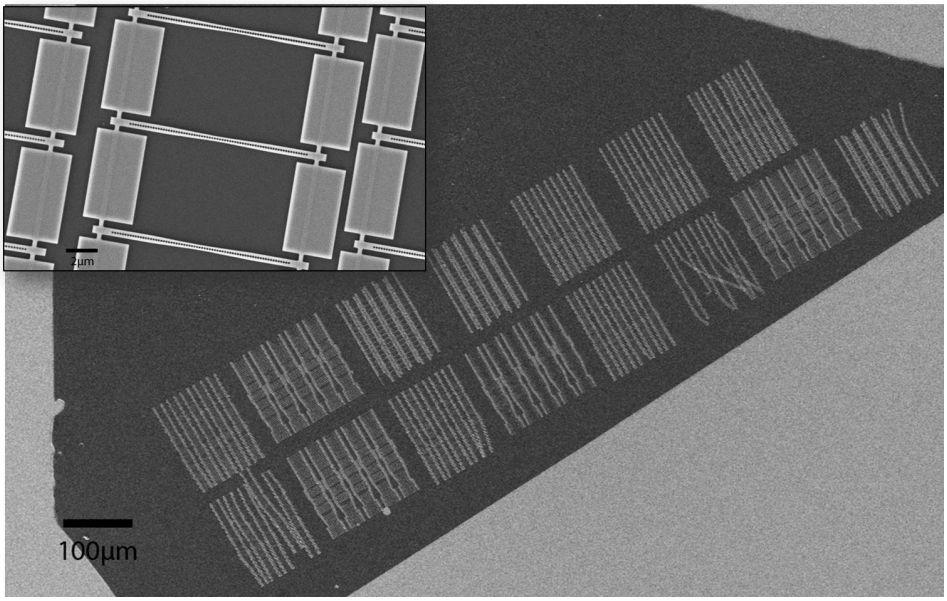

Figure 40: Depiction of the photonic crystal HSQ mask on a diamond film (dark) on a Si substrate. The inset shows a magnified view of a set of PCC mask having a parabolically tapered width.

To fabricate photonic crystals from a bulk piece of diamond, we employ a similar method for nanostructuring as presented in chapter 3.2.2. Briefly, as depicted schematically in figure 41c, we begin with deep-etching a type IIa CVD or Ib HPHT single crystal diamond membrane resting on a Si substrate to the desired device thickness of 250 nm. We then define an etch mask via EBL on HSQ resist film spun on the diamond substrate. Many arrays of photonic crystals with different designs, scalings and out coupling sections can be

written on the same film in parallel (Fig. 40). A second oxygen RIE step transfers the mask pattern into the diamond thin film. Finally, we remove the substrate material from beneath the devices with an isotropic etch recipe for Si in a STS RIE (5 min using a N_2O flow rate of 1420 sccm, N_2 of 392 sccm, SiH_4 of 10 sccm at a chamber pressure of 900 mTorr and a 30 W HF power), resulting in suspended nanobeams. Figure 41d shows a scanning electron microscope (SEM) image of several photonic crystal nanobeams (left) as well as a magnified view (right). Optical images of the undercut PCCs are provided in figure 42 where the diamond film wedging is visible. Similar thicknesses of PCCs can be identified via having a similar color.

The design for our photonic crystals consists of a series of holes etched through a diamond ridge waveguide, illustrated schematically in figure 41a. Light is confined to the waveguide by the index contrast between diamond ($n = 2.4$) and air, while the periodicity of the holes forms a bandgap to confine light along the waveguide. The ability to store light in the cavity region in the time domain can be quantified by the Q factor. The particular parameters of our design were chosen to accommodate the inaccuracies of our fabrication process. In particular, devices obtained from the above procedure exhibit significant thickness variations from device to device across a single chip, owing to an initial thickness gradient in the mechanically polished diamond membrane, which is transferred to the film in the

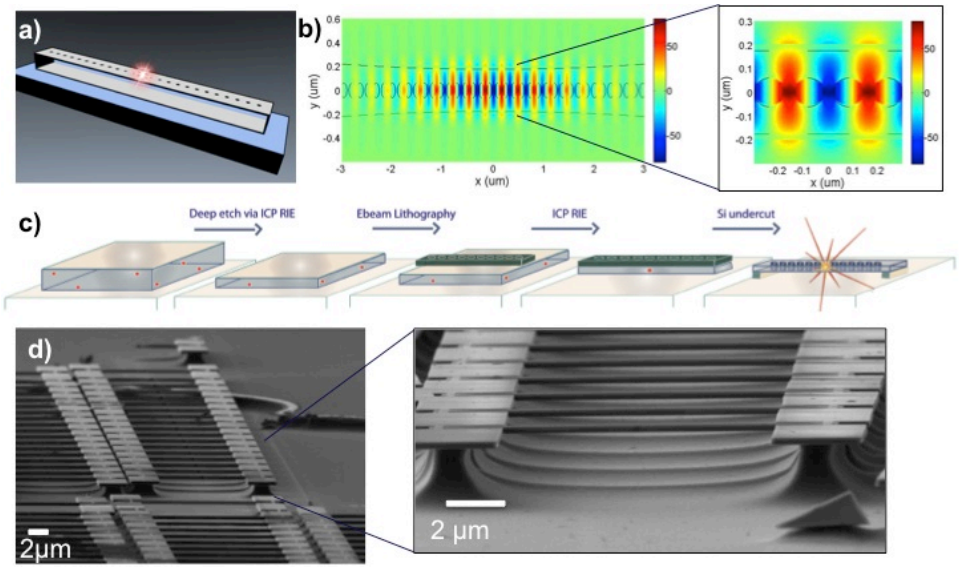

Figure 41: (a) Cartoon of a 1D photonic crystal nanobeam with an emitter coupled to the cavity. (b) FDTD modelling of the mode profile of a 1D photonic nanobeam. The hole diameter was constant while the width of the beam was tapered. (c) Fabrication schematic of diamond nanobeams. First, a diamond membrane was thinned to the optical device layer in a deep reactive ion etch, second, EBL was performed to define the mask, third the mask was transferred to the diamond in a second RIE step. Then, the diamond nanobeams were undercut in an isotropic RIE step etching the Si layer underneath. (d) SEM image of freestanding diamond nanobeams.

deep RIE step. As a result, we designed our photonic crystals to be robust to moderate variations in thickness within the range of $200 - 400\,\text{nm}$. To accomplish this, we used a relatively large hole radius (65 nm) and periodicity (ranging from 165 nm to 175 nm), which were kept uniform across the entire photonic crystal. The cavity is then formed by tapering the width of the waveguide down from 500 nm at the ends to 400 nm at the cavity center, in a parabolic profile [5, 141]. Various scaled versions were also implemented to accommodate fabrication imperfections. Modeling of 1D nanobeams was performed using the 3D finite difference time domain (FDTD) software Lumerical. Coupling between the nanobeam photonic crystal cavity and an optical waveguide can be easily achieved [142] by modifying the geometry of the mirror holes at the ends of the photonic crystal. This allows for integration of multiple devices on the same chip and realization of integrated quantum networks. To achieve a high transmission signal ($T \propto \frac{Q_t}{Q_{wg}}$), the scattering Q factor ($\text{Q} \approx 8 \cdot 10^6$) was designed much larger than the waveguide Q. The waveguide limited ($Q \approx 5.3 \cdot 10^5$), total Q factor was determined to reach values up to $Q \approx 5 \cdot 10^5$, with a mode volume of $1.8 \cdot \left(\frac{\lambda}{n}\right)^3$, concentrated in the diamond (Fig. 41b). Photons coupled into the optical waveguides were outcoupled at the end facet of the waveguide and collected using a lens with large numerical aperture (Fig. 44a, left). In addition, we explore an alternative cavity design with a

central hole removed. This cavity geometry features a moderate, scattering limited Q factor ($Q_{scattering} = 1 \cdot 10^4 < Q_{waveguide}$ and mode volume of $3.7 \cdot \left(\frac{\lambda}{n}\right)^3$ and multimode behavior, but in turn increases the likelihood of locating an NV center in the cavity. A top-view of a suspended nanobeam showing the width taper and filled in hole is presented in figure 44a (right). Conventional designs, where the width is kept constant and the hole radius is tapered in the cavity region have been studied as well 43. Moreover, a design has been studied that implements a gaussian taper in hole radii which is waveguide limited and provides ultra-high Q factors [141]. However, the above mentioned tapered-width design was experimentally the easiest to characterize and most robust towards fabrication imperfections. All data will hereafter refer to this particular design.

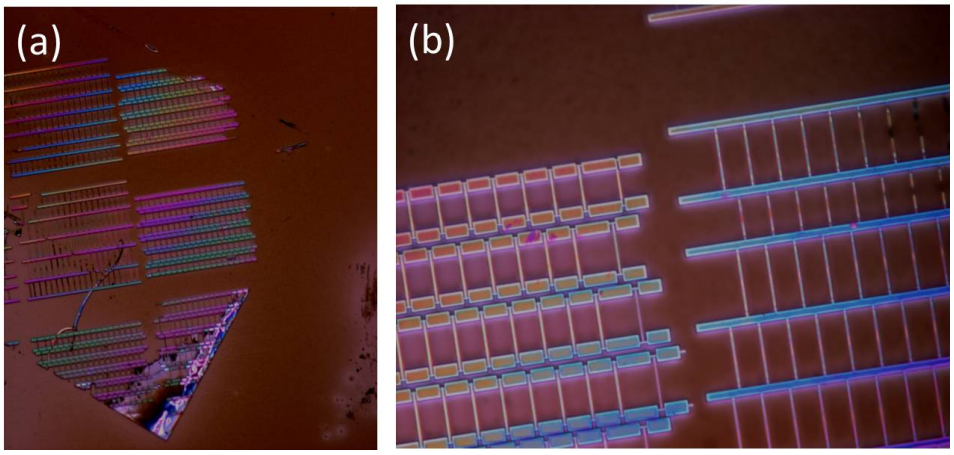

Figure 42: Optical images of **(a)** an array of different sets of undercut PCCs and **(b)** two sets having different out coupling sections for transmission measurements. The thickness variations can be inferred from the color information.

An added advantage of 1D photonic crystals is the natural integration of their geometry with propagating waveguide modes. Coupling between cavity and waveguide modes can be easily controlled by varying the region of mirror holes at the ends of the photonic crystal, and subsequently routed through other photonic devices on the chip or coupled to free space. We investigated waveguide coupling in our cavities by adding simple broadband outcoupling structures to the ends of our nanobeams. The outcouplers are formed by extending the nanobeam in a terminated waveguide section, as shown in figure 44a (left).

7.3 Experimental

Characterization of the cavity spectral properties is performed in two ways. First, we probe the cavity response to a broadband input in a transmission configuration. We excite waveguide modes of the diamond nanobeam by coupling white light from a supercontinuum source (NKT Photonics) into the waveguide at one end. Light that is resonant will then couple to the cavity mode and either be scattered or transmitted to the far end of the waveguide. Figure 44b illustrates this behavior, with light focused onto the right end of the device and scattered from a well-localized spot at the cavity center and from the outcoupler at the left end of the waveguide. We collect the scattered light from each location and analyze its spectrum to obtain the cavity resonance frequency and Q factor (Fig. 44c). With this method we measured spectrometer-limited Q factors exceeding 6,000 for resonators with a filled hole. These Q factors are close to the modeled value for resonators having a filled central hole.

For devices containing an NV center, the cavity spectral properties can also be measured in the PLE spectrum of the NV center, as follows. The presence of an NV center in the vicinity of the cavity is determined by confocal microscopy. A 532 nm laser (Coherent Compass 315M) is focused onto the sample and scanned over the field

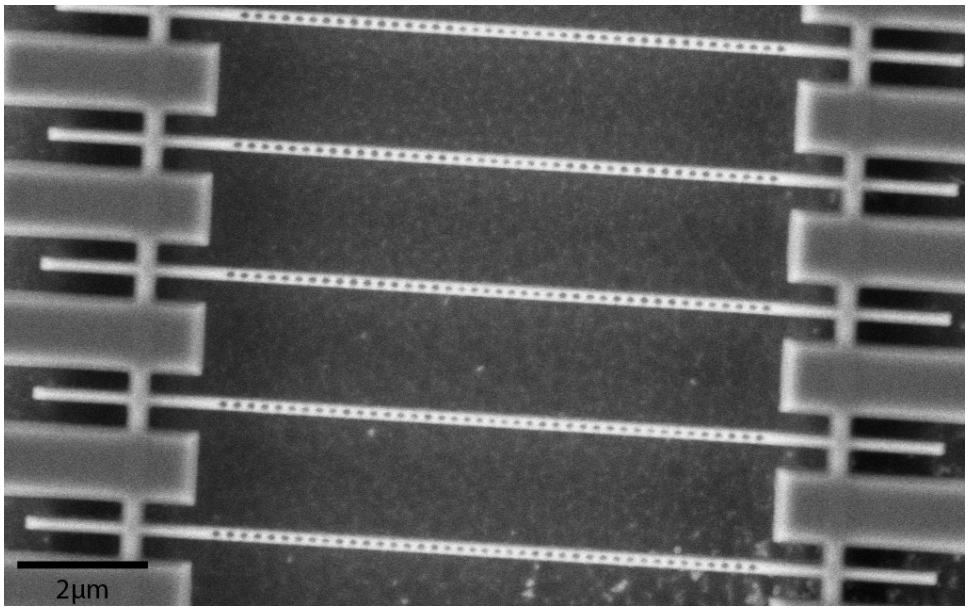

Figure 43: Suspended PCCs with a tapered hole cavity region in the center.

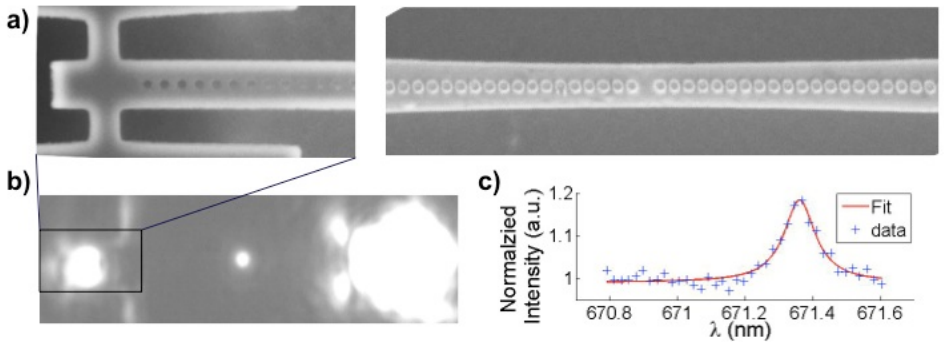

Figure 44: (a) SEM top view of a suspended photonic crystal nanobeam, (right) as well as of the outcoupling region for transmission measurements (left). (b) Transmission measurement of white light from a supercontinuum source incoupled at the right end of the waveguide. Outcoupled and upscattered light is observed both at the cavity region as well as the other end of the cavity. The scattering of the cavity mode is well localized. (c) Spectra obtained at the cavity region in transmission show cavity modes with Q factors up to 6,000.

of view to excite any NV centers, which occur natively and randomly throughout the diamond (in a relatively high density for the diamond types studied here). Emitted light at the excitation spot is collected while green light is filtered out, so that NV centers can be identified as bright spots (Fig. 45a). Single NV centers can are identified by verifying that the second-order autocorrelation of the PLE signal exhibits an antibunching dip below 0.5 (Fig. 45b, and equation 4.2) [94]. Having identified a proximal NV center, we now use it to measure the cavity spectrum. The NV PLE contains components from both charge states (NV- and NV0) and away from the ZPL provides a relatively flat, broadband source with which to probe the frequency of cavity modes over a range from $575 - 800\,\mathrm{nm}$. Hence, resonant fluorescence couples into the cavity mode and is partly scattered into free space as the cavity decays (mere background emission from diamond is sufficient as well). The combined emission of NV center and cavity thus exhibits intensity peaks at the cavity resonances, as shown in figure 45c, from which we can infer both the cavity frequency and Q factor, which are in good agreement with the measured values from the white light transmission measurements described above. In this way, we have measured Q factors up to 6,000, also limited by the resolution of our spectrometer. Having identified an NV center-cavity system of interest, we now wish to control the coupling of coherent NV center emission to the cavity mode.

7.4 Tuning of cavity modes

Integration of our cavities with NV centers for quantum optical applications requires spectral overlap with a narrow-band transition, associated with the ZPL. However, as discussed above, fabrication imperfections and diamond film wedging result in shifts of the cavity resonances from the predicted values, such that the cavity mode is, in general, not at the frequency of the ZPL transition. We employ two methods to tune our cavities, by either etching away material to blue-tune [146], or condensing Xe gas to red-tune [126]. The two techniques are complementary, the etching method working well for coarse, unidirectional tuning over a large range (up to 23 nm), while the red-tuning method can tune in finer, reversible, steps, but over a shorter range (7 nm). To take advantage of this complementarity and ensure flexibility in the tuning, we therefore design the resonances to be positioned to the red of the ZPL when fabricated, such that they can be blue-tuned past the ZPL by isotropically etching away diamond, and finally red-tuned precisely to the ZPL frequency by Xe condensation at low temperature.

For the blue-tuning, we used two etching methods to remove material from the diamond surface, one with an oxygen plasma etcher (Technics, Model 220) and the other in a rapid thermal processor in oxygen environment (Modular Process Technology, RTP-600xp). The

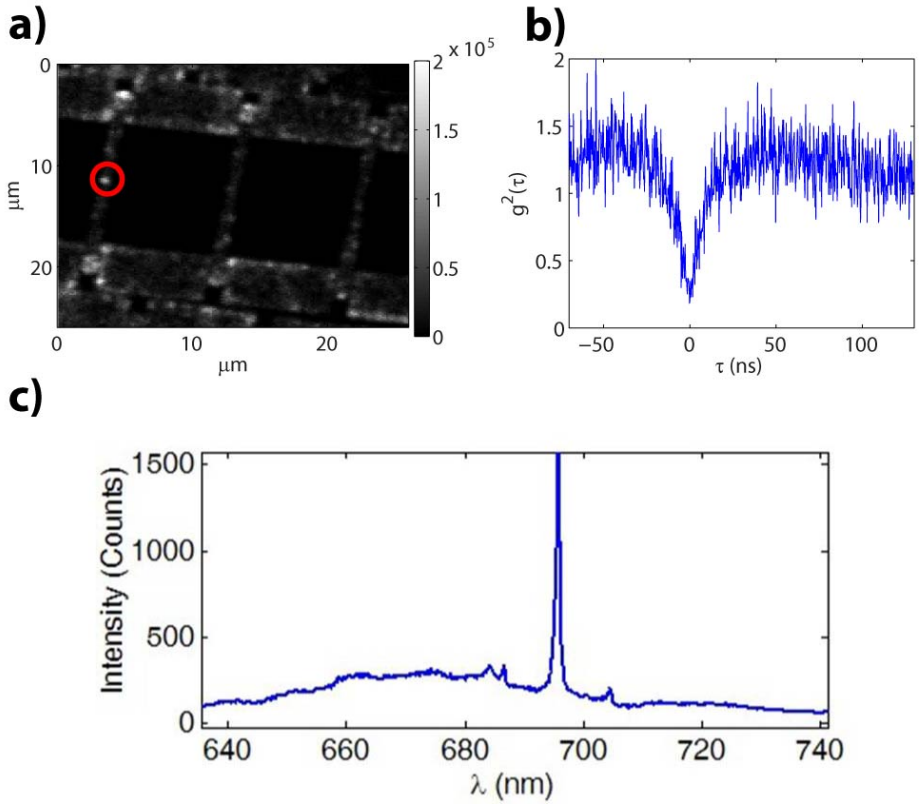

Figure 45: (a) Confocal microscope image of fluorescence from a device under excitation with $532\,\mathrm{nm}$ light. Individual NV centers are visible as bright spots along the nanobeam. (b) Second-order autocorrelation measurement of the fluorescence from an NV center in the cavity region of the nanobeam. The value for zero delay, $g^2(0) = 0.2$ is below 0.5, identifying it as a single NV center. (c) Fluorescence spectrum of the device collected directly from the NV center location. The broad phonon sideband of the NV center is coupled to the cavity at the resonance wavelengths ($685\,\mathrm{nm}$, $695\,\mathrm{nm}$, $705\,\mathrm{nm}$) and the enhanced emission into the cavity is subsequently scattered into free space and collected by the objective along with the NV center emission.

mode positions of a cavity mode having a Q factor of 1100 were studied over a series of etch steps (of varying step lengths). Figure 46 shows the blue shifting of the mode after each etch step. Other cavities on the same chip experienced similar blue-shifts as a result of the etch steps. By varying the duration of the etch we were able to etch in steps ranging from 0.2 nm to 5.3 nm, with the plasma etcher having more reproducible etch rates. In total, we were able to tune by 23 nm over the course of 8 etch steps without deterioration of the Q factor.

We next use reversible red-tuning in fine steps of the cavity resonance to the ZPL of the NV center by condensing Xe gas onto the diamond surface and consequent enhancement of the ZPL fluorescence. In order to condense the Xe, while minimizing phonon broadening of the ZPL, we carry out tuning at 4 K by cooling our devices in a helium flow cryostat (Janis, ST-500). We begin by identifying a cavity containing an NV center, for which the cavity line is just to the blue of the ZPL frequency at 637 nm. The spectrum for such a device at low temperature is shown in the bottom line of figure 47a (zoom in to the ZPL shown in figure 47b). In the device shown, three cavity lines are visible in the spectrum to the blue of the ZPL, which itself exhibits two distinct frequency components. We next released puffs of Xe gas into the chamber through a nozzle directed at the sample and positioned 1 cm from it. Spectra were taken between

each puff to monitor the cavity resonance frequency. The tuning was observed to happen within seconds of the Xe being released, after which the cavity frequencies were stable for hours, indicating no further gas dynamics. Reheating the sample to room temperature reverses the tuning. With this procedure we were able to repeatedly tune over a range of 7 nm in step sizes of 0.5 nm, without significant degradation of the cavity Q.

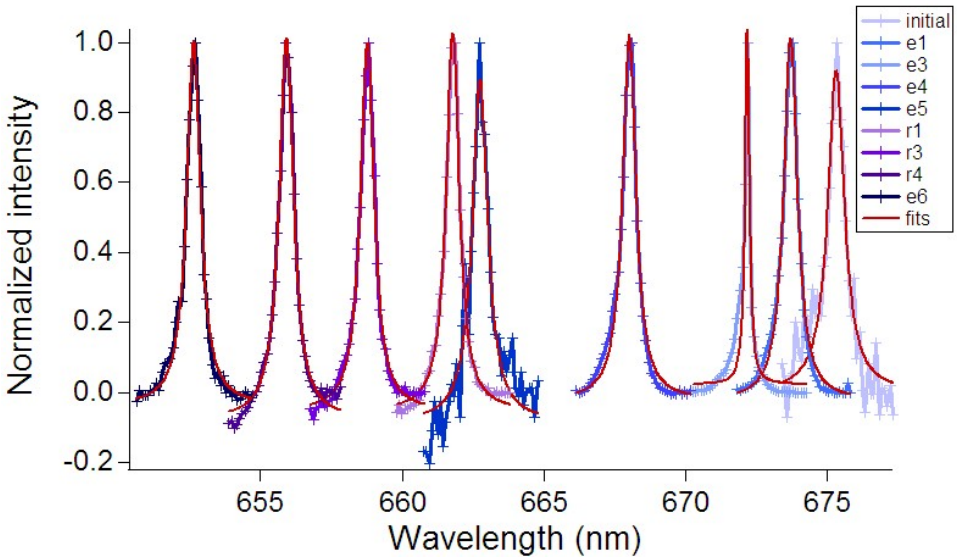

Figure 46: Controlled blue-tuning of a cavity mode via oxygen etching shown over 8 etching steps. e refers to etching in an oxygen plasma etcher, while r refers to etch steps performed in a rapid thermal processor. The etch times are of differing lengths, background has been subtracted and modes are normalized by the peak intensity. An overall average tuning range of 23 nm was observed from several devices.

7.5 Results: ZPL Enhancement

As the cavity is tuned into resonance with the ZPL of the NV center, the total signal in the ZPL band is enhanced due to the interaction with the cavity mode. This enhancement is quantified by the Purcell factor, which in the case of a resonant interaction is given by:

$$F_P = \frac{3}{4\pi}\left(\frac{\lambda}{n}\right)^3 \frac{Q}{V}\frac{\left|\mathbf{E_{NV}}\cdot\mu_{\mathbf{NV}}\right|^2}{\left|\mathbf{E_{max}}\right|^2\cdot\left|\mu_{\mathbf{NV}}\right|^2} \tag{7.1}$$

where $\left|\mathbf{E_{NV,max}}\right|^2$ are the cavity electric field at the position of the NV center and cavity mode maximum, respectively, $\left|\mu_{\mathbf{NV}}\right|^2$ is the NV center dipole moment, λ is the wavelength of the cavity mode and $n = 2.4$ is the refractive index of diamond, and $V = \left[\int \epsilon(\mathbf{r})\left|\mathbf{E}(\mathbf{r})\right|^{\mathbf{2}}\mathbf{d^3r}\right]/max[\epsilon(\mathbf{r})\left|\mathbf{E}(\mathbf{r})\right|^{\mathbf{2}}]$ is the cavity mode volume.

Figure 47 shows the PLE spectrum through a series of Xe deposition steps, clearly indicating an enhancement of the ZPL intensity when the cavity comes into resonance. The spectra in figure 47 have been normalized to the diamond Raman line at 573 nm to account for overall intensity fluctuations resulting from the Xe condensation.

By comparing the spectra when the cavity is resonant with the ZPL to those when it is off-resonant, we can obtain an estimate of the Purcell enhancement. In the case of a resonant cavity (as in the top

spectrum of figure 47), the total ZPL intensity is given by:

$$I_{ZPL}^{res} = \left(\eta_{cav} F_P + \eta_{NV}\right) \frac{1}{\tau_0} \tag{7.2}$$

where $\eta_{can,NV}$ are the overall collection efficiencies for photons emitted by the cavity and by the NV center directly, respectively, and τ_0 is the NV center excited state lifetime in the absence of any Purcell enhancement. In the off-resonant case this reduces simply to

$$I_{ZPL}^{off-res} = \frac{\eta_{NV}}{\tau_0} \tag{7.3}$$

. Dividing equation 7.2 by 7.3 and further making the assumption that $\eta_{can} = \eta_{NV}$, i.e. that cavity Q is scattering-limited, we arrive at:

$$F_P = \frac{I_{ZPL}^{res}}{I_{ZPL}^{off-res}} - 1 \tag{7.4}$$

. This Purcell factor is histogramed in the right-hand panel of figure 47b. A maximum Purcell enhancement of 7 is observed when the cavity is resonant with the ZPL.

This modest enhancement is substantially lower than expected given our cavity parameters. With a cavity Q of 1634 and mode volume of $3.7 \cdot \left(\frac{\lambda}{n}\right)^3$, we expect an enhancement of 34 for ideal NV center placement and orientation. This discrepancy relative to our measured enhancement suggests that a substantial improvement can

be gained by a more deterministic method for spatial alignment of the NV center with the cavity, in addition to improving the cavity Q factor through better fabrication.

7.6 Conclusions and Outlook

In this chapter we have described the design and fabrication of suspended, 1D photonic crystal cavities made from high-purity, single-crystal diamond, and having Q factors of up to 6000. Methods for blue tuning over a range of 23 nm and red tuning over a range of 7 nm were demonstrated, culminating in the selective enhancement of the ZPL intensity of a single NV center by a factor of 7, as verified by tuning a cavity mode into resonance with the NV center s ZPL at low temperature. To facilitate the process of finding a device with a well-coupled NV center we used our lower-Q, higher mode volume design, however with our best fabricated cavities and an optimally placed NV center, we would expect an enhancement of up to 250. With smaller mode volume designs, more refined fabrication techniques to reduce side-wall roughness (Fig. 48), and by developing deterministic methods for spatial alignment of the NV center within the cavity mode, even larger enhancement factors can be expected. Along with the recent work in 2D photonic crystals [56], these results open up promising avenues for new technologies in quantum sensing,

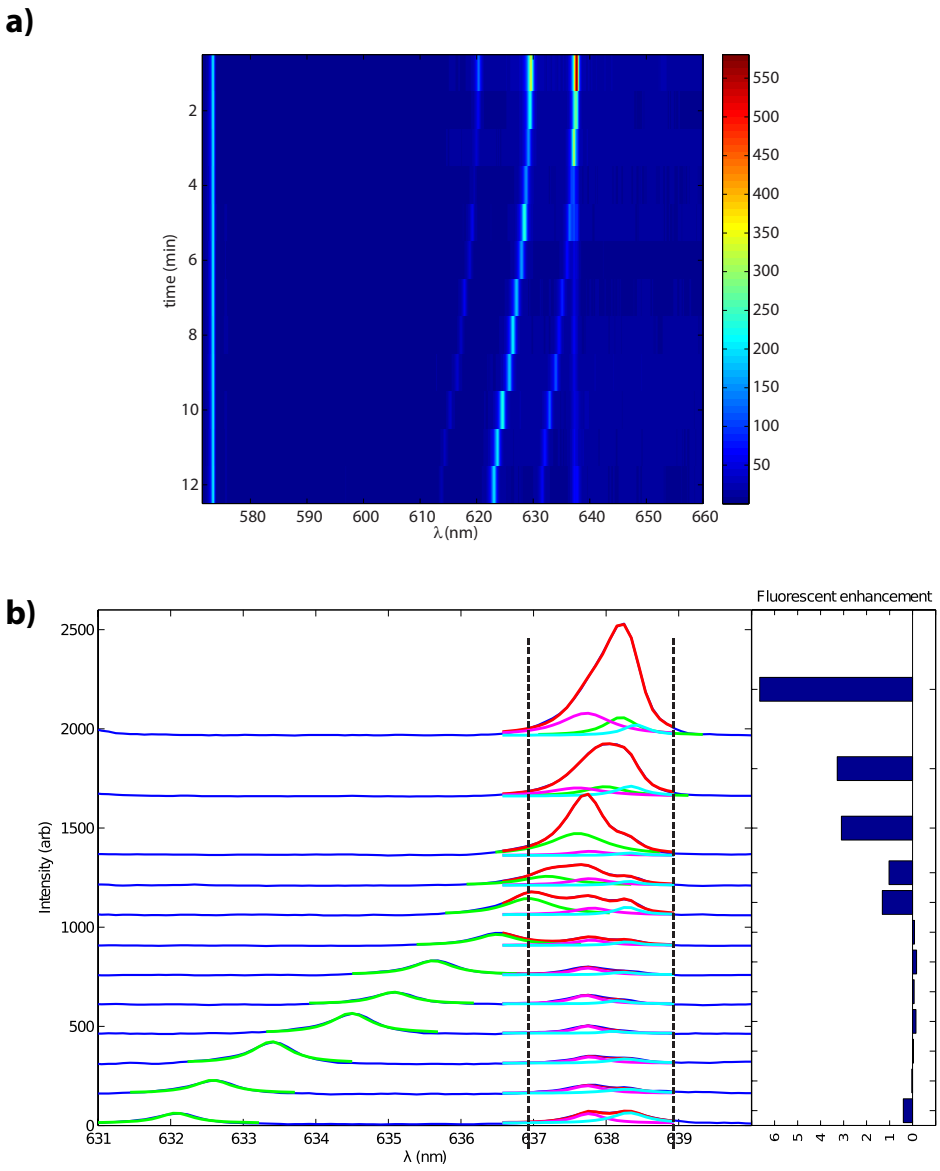

Figure 47: Tuning the cavity into resonance with the ZPL of the NV center. The cavity is tuned into resonance by condensing Xe gas onto the device while continuously measuring spectra of the NV center at $4\,\mathrm{K}$ in a cryostat. Xe is injected into the chamber where it condenses and redshifts the resonance frequency of the cavity mode. When the cavity frequency overlaps the ZPL the fluorescence intensity is enhanced by a factor of $F_P \approx 7$. (b) Magnified and fitted version of figure (a) where a split ZPL is observed. The dashed lines indicate the limits for integration when estimating the Purcell factor. The histogram at the right represents the corresponding enhancement.

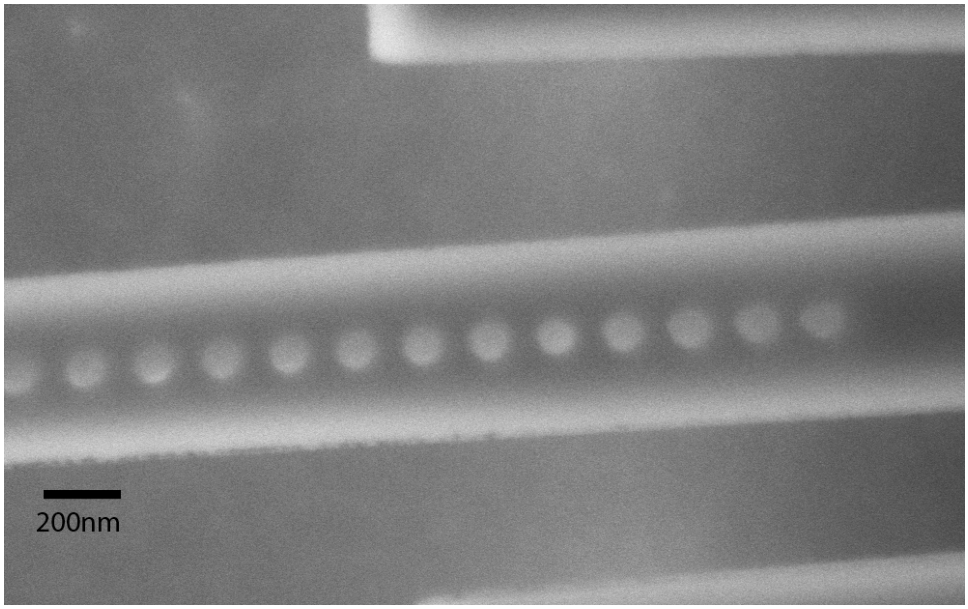

Figure 48: Top-view of a PCC. The surface roughness could originate from mask erosion during the etch or the EBL writing technique.

quantum information science, and quantum networks [93].

The small 1D footprint and fabrication by RIE make the current approach scalable, with 1,000 devices fabricated in parallel on a single chip. Additionally, the coupling to propagating waveguide modes, which occurs naturally in 1D photonic crystal devices, makes this geometry attractive for quantum networks and quantum information applications. Although improved methods must be found which allow for incorporation of these devices with implanted, stable NV centers, our method provides the framework for realizing such advanced quantum technologies.

Part II

Second part: Integrated Nonlinear Optics in Diamond

Unique material properties make diamond a promising candidate for on-chip high-performance photonic devices with novel functionalities. In particular, diamond's large Raman-gain (13.5 cm/GW at 1064 nm)[57], relatively large Kerr nonlinearity [26, 107] ($n_2 = 1.3 \cdot 10^{-15}\,\mathrm{cm}^2/\mathrm{W}$), wide bandgap (5.5 eV), negligible multi-photon loss mechanisms [41], as well as excellent thermal properties (high thermal conductivity of 2000 W/mK, and small thermo-optic coefficient of $dn/dT = 10 \cdot 10^{-6}\,\mathrm{K}^{-1}$) [128] are of interest for the implementation of active and passive optical devices capable of handling high optical powers. In order to take full advantage of these exceptional properties of diamond, it is desirable to fabricate devices integrated on a chip. A diamond-on-insulator (DOI) platform recently developed for applications in quantum optics [55, 76, 111], based on single crystal diamond films on top of a low index substrate, is well suited for these applications. Two promising applications of DOI, and diamond photonics in general, are the realization of coherent light sources based on Raman scattering at wavelengths where semiconductor lasers are hard to implement [125, 149, 150, 163], and parametric nonlinear processes that may lead to wide-bandwidth frequency comb generation [44, 189]. However, the realization of high performance devices places stringent requirements on the diamond film quality. For example, polycrystalline diamond approaches [176, 177] suffer from light absorption and scattering at grain

boundaries, and therefore single-crystal diamond films are of interest for applications mentioned above. Single-crystal thin diamond films can be generated using either ion implantation assisted liftoff [104, 135, 175] or substrate thinning approaches [55, 56, 76]. The former method leaves residual stress within the diamond films [114] that can be detrimental for applications in photonics, but might be overcome using an approach based on regrowth of diamond [4]. This makes the latter approach the most promising route towards a high-performance DOI platform so far, and is the one employed in this work. However, further advances in material science and engineering will likely overcome difficulties associated with polycrystalline and ion-sliced single crystal diamond films. For example, low-loss optical waveguides and resonators having high quality (Q) factors have been successfully fabricated in other polycrystalline materials including Si [139] and TiO_2 [27], while ion-slicing is routinely used for high-performance silicon-on-insulator (SOI) platforms.

To love beauty is to see light.

Victor Hugo

8

The platform for nonlinear optics: Integrated diamond ring resonators

The realization of an integrated diamond photonic platform, based on a thin single crystal diamond film on top of a silicon dioxide/silicon substrate, is reported in this chapter [79]. Using this approach, we

demonstrate high- quality factor single crystal diamond ring and race-track resonators, operating at near-infrared wavelengths ($1,550\,\mathrm{nm}$). The devices are integrated with low-loss diamond waveguides terminated with polymer pads (spot size converters) to facilitate in- (out-) coupling of light from (to) an optical fiber. Optical characterization of these resonators reveal quality factors as high as 250,000 and overall insertion losses as low as $1\,\mathrm{dB/facet}$. Scattering induced mode splitting as well as signatures of nonlinear effects such as optical bistability are observed at an input pump powers of $100\,\mathrm{mW}$ in the waveguides.

8.1 Introduction to ring resonators and their design

A waveguide that is bent such that its ends connect forms a ring resonator with a specific radius R. Reviews on the physics of ring resonators can be found among others in refs [24, 157, 184]. Here, a discussion based on that presented in [24, 184] will be treated in brevity.

In nanophotonics it is common to refer to the quality (Q) factor of a resonator. It describes the ability of a resonator to store light (within a factor of 2π): how many oscillation the system can perform before the power falls off to $1/e$. General applications of ring resonators include their use as filters, switches and/or wavelength

division multiplexer (WDM) in optical communication [110], sensing [100], modulators [182] etc. Losses can be segmented into waveguide propagation (material absorption and scattering) losses, coupling (scattering and waveguide and mode mismatch due to ring cross-section mismatches) losses between ring and waveguide, bending (scattering) losses as well as mode mismatch losses in between straight and bent segments of a racetrack resonator. To obtain high Q factors, minimizing the loss channels is crucial and will be discussed in detail in section 9.2. The Q factor is related to ring resonator losses and can be written as a sum of inverse Q factors associated to different loss channels as: $1/Q_L = 1/Q_0 + 1/Q_C + 1/Q_{sc}$, where Q_L denotes the loaded (total) Q factor equivalent to the measured Q factor of a device, Q_0, Q_C and Q_{sc} represent the intrinsic, coupling and scattering being inversely proportional to the dissipated powers associated with bending, coupling and scattering losses (material losses are assumed to be negligible for diamond).

So far Q factors exceeding $1 \cdot 10^8$ have been achieved in planar silica toroidal microresonators at telecom wavelengths [9], which has been extended to $8 \cdot 10^8$ for wedge-resonators in Silica. While toroidal microresonators and wedge resonators provide access to ultra high Q devices via the means of reflow techniques that minimize scattering loss, these geometries are not intrinsically integratable with other devices on chip since they reside on pedestals and hence not

necessarily CMOS compatible. Intrinsic Q factors as high as $20 \cdot 10^6$, $28 \cdot 10^6$ and $7 \cdot 10^6$ have been achieved for ring resonators integrated with directional waveguide couplers made of Si_3N_4 on silica at 1060 nm, 1310 nm and 1550 nm respectively [165]. In the visible wavelength regime, Q factors of $3.4 \cdot 10^6$ have been obtained in Si_3N_4 microdisks on silica with integrated waveguide couplers [84].

Ring resonators can be accessed via bus waveguides in close proximity to the ring and light is evanescently coupled between the ring and the bus waveguide. A ring contains multiple resonances, whenever the phase shift induced by the wave inside the ring matches an integer multiple of 2π, or equivalently, each time an integer multiple of the wavelength λ matches a round trip of the light in the ring (or the optical path length of the ring) [24]:

$$m\lambda = n_{eff} \cdot L = 2\pi R n_{eff}, \qquad m = 1, 2, 3, ... \tag{8.1}$$

Where n_{eff}, m and L are the effective refractive index, an integer number and the round trip length respectively.

The transmitted to incident field ratio can be described by:

$$E_T = \frac{t - ae^{-i\delta}}{1 - t^* a e^{i\Phi}} E_0 \tag{8.2}$$

where $\delta = 2\pi L n_{eff}/\lambda$ is the round trip propagation phase shift inside the ring, $a = e^{-\alpha L}$ is related to the amplitude attenuation α due to

propagation losses such as bending and scattering losses and t corresponds to the transmission coupling coefficient. The power is split into coupled light into the ring κ^2 (with κ as the coupling coefficient between the waveguide and the ring) and transmitted light t^2 while power conservation is guaranteed in the coupling section via $t^2 + \kappa^2 = 1$ (no loss in coupling section itself). The transmitted intensity can hence be obtained via

$$I_T = |E_T/E_0|^2 = \frac{a^2 + t^2 - 2at\cos\delta}{1 + a^2t^2 - 2at\cos\delta}$$

If the roundtrip phase shift equals an integer multiple of 2π, $\delta = m \cdot 2\pi$, the incident light is resonant with the resonator mode, such that transmitted intensity satisfies

$$I_T = \frac{(a-t)^2}{(1-at)^2}$$

Furthermore, if losses in the ring are negligible, $a \approx 1$ (equivalently the intrinsic quality factor, which provides a measure of the resonator's ability to temporally store light, goes to infinity $Q_0 = \infty$), the transmission is unity for all phase shifts δ. However, for critical coupling, when $t = a = \sqrt{1 - |\kappa|^2}$ so that the power loss in the ring $1 - |a|^2$ equals the coupled power κ^2, the transmission dip of a resonance goes to 0.

The full width half maximum of a resonance can be described in

terms of the resonant wavelength λ_{res}, the field amplitudes t, a, the round trip length L and the group index n_g which takes waveguide dispersion into account:

$$\delta\lambda = \frac{(1-ta)\lambda_{res}^2}{\pi n_g L\sqrt{ta}} \tag{8.3}$$

$$n_g = \frac{c}{v_g} = n_{eff} - \lambda_0 \frac{dn_{eff}}{d\lambda} \tag{8.4}$$

where v_g is denoted as group velocity (velocity of the envelope of a pulse in a medium as supposed to the phase velocity $v_p = \omega/k$, the velocity at which the phase travels for a given frequency). The free spectral range can be approximated to be

$$\Delta\lambda \approx \frac{\lambda_{res}^2}{n_g L} \tag{8.5}$$

Hence the Q factor and finesse (F) of the resonator are represented via

$$Q = \frac{\lambda_{res}}{\delta\lambda} = \frac{(1-ta)\lambda_{res}}{\pi n_g L\sqrt{ta}}, \quad F = \frac{\Delta\lambda}{\delta\lambda} \approx \frac{\pi\sqrt{ta}}{1-ta} \tag{8.6}$$

Here, to design waveguide coupled single crystal diamond (SCD) ring resonators based on the DOI platform, 3D Finite difference time domain (FDTD) modeling (Lumerical Solutions, Inc) is used. The cross section of the resonator and waveguide is first determined to satisfy single mode operation and phase matching (in nonlinear

applications anomalous dispersion, see chapter 9) . The waveguide and ring resonator cross sections are chosen to be equal to obtain ideal mode matching between them. For Raman and Brillouin processes that involve photon - phonon scattering, material dispersion does not need to be attributed. These processes are selective towards phonons with the appropriate wave vector k. Hence, there is an optimum crystal orientation with respect to the light polarization. As mentioned earlier, critical coupling is achieved when the ring resonator loss equals the amount of light coupled to the ring. Numerically, the coupling efficiency between waveguide and ring resonator (and hence the gap size) can be determined when placing a dipole emitter (with TE or TM polarization) in the ring resonator and monitoring the decay into the waveguide. The radius is first chosen to be large to avoid any bending loss contributions. After the Q_C is designed, the bending radius loss can be obtained via choosing smaller and smaller radii and monitoring the decay. In this chapter, single mode operation is obtained at $1,550\,\mathrm{nm}$ for a diamond waveguide with a cross-section of $600\,\mathrm{nm}$ x $500\,\mathrm{nm}$ (refractive index $\mathrm{n_{diam}}$ of 2.4) on a $2\,\mu\mathrm{m}$ thick SiO_2 on Si substrate capped with silica. The coupling Q factor Q_C between waveguide and cavity is larger than 250,000 for a gap size of $500\,\mathrm{nm}$. A resonator length of $330\,\mu\mathrm{m}$ is used.

8.2 Bare ring measurements using tapered fibers

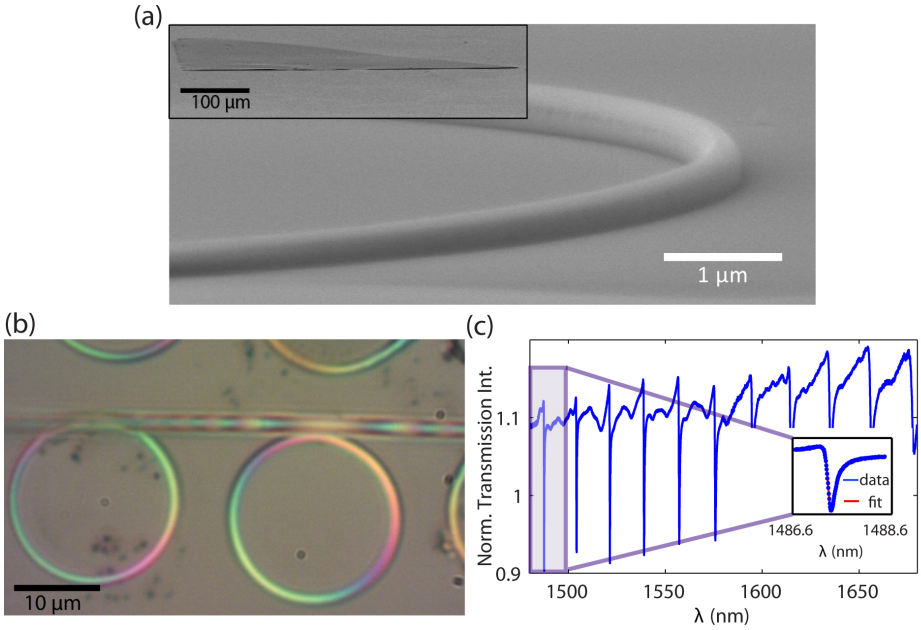

Figure 49: (a) Scanning electron microscop (SEM) image of a diamond ring resonator on low index substrate. The residual resist layer remained on the ring during characterization. Inset: SEM image of an optically thin single crystal diamond slab on a SiO_2/Si substrate before making devices. **(b)** Optical image of single diamond ring resonators on a quartz substrate. A tapered optical fiber, used to in- and out-couple light can also be seen. The rings have a $20\,\mu$m diameter, with a waveguide cross-section of $410\,$nm x $1\,\mu$m. The $300\,$nm thick low-index (1.5) resist layer was kept on top of the ring. The rainbow-pattern in the rings is due to thickness variations of the diamond film. **(c)** Transmission measurement features sharp dips that correspond to the modes of the ring resonator. The Q-factors obtained using Fano-like fits range from 700 ($1678\,$nm) to 9,000 ($1487\,$nm). Inset: Blow-up of one of the resonances.

To test our predictions, an array of bare diamond ring resonators, without coupling waveguides and capping silica, are first fabricated on

quartz substrates. A slightly different geometry from the one discussed above is used, with an outer ring radius of 20 μm and cross section of 400 nm x 1 μm. The planar diamond device fabrication sequence used is described in chapter 3.2.2 (see diamond film on silica substrate (inset) and ring profile in figure 49a). Bare diamond rings are shown in figure 49b along with a tapered silica fiber [31, 98] which is used to evanescently couple light to the rings. To ensure coupling to one device at a time, a small dimple is indented in the middle of the tapered region [15, 164]. Note that in the experiments presented here the optical fiber is in contact with the diamond rings. The performance of the ring resonators is probed in transmission measurements using scanning lasers (Santec, TSL 510) spanning a $1480 - 1680$ nm wavelength range. Figure 49c shows a representative normalized transmission spectrum, which features regularly spaced dips that correspond to optical resonances of the structure. The inset in figure 49c shows a blow-up of one of the resonances, which has been fitted to a Fano profile [54, 65]:

$$F(\lambda) = a_1 - a_2 \cdot \frac{(q + 2(\lambda - \lambda_0)/\gamma)^2}{1 + (2(\lambda - \lambda_0)/\gamma)^2} \tag{8.7}$$

Here, γ corresponds to the linewidth of the resonance while λ_0 represents the resonant wavelength. The asymmetry of the resonance is attributed to the Fano parameter q [54] and a_1, a_2 are fitting parameters. The Fano-like shape is attributed to interference between

light coupled to the ring resonator and light partially reflected from fiber discontinuities (e.g. fiber-ring coupling section, fiber facets) which leads to a perturbation of the phase of the transmitted wave [33]. A Q-factor of 9000 at $\lambda = 1487.4\,\mathrm{nm}$ is extracted, corresponding to a finesse (F) of 100. Both quantities decrease significantly for longer wavelengths ($Q \approx 700$, $F \approx 12$ for $\lambda = 1676\,\mathrm{nm}$), which is attributed to a larger scattering loss at the outer ring edge caused by reduced confinement in the high index material, as well as to larger coupling into the fiber. Since the fiber is touching the ring resonator the measurements are likely performed in the over-coupled limit where the field decay rate to the tapered fiber, exceeds the intrinsic loss rate of the ring resonator, thus reducing the overall Q factor of the resonator. This effect is more dramatic at long wavelengths where the transmission drops by only 18 % on resonance. The color change in the optical image (Fig. 49) is attributed to the thickness variation of the film, which arises from the polishing step. A wedge-like profile of the diamond plates has been measured prior fabrication with a minimum of $1\,\mu\mathrm{m}$ thickness change over a 3 mm sample.

8.3 Initial results of waveguide integrated ring and racetrack resonators

To realize fully integrated diamond photonic networks that enable efficient and robust coupling of light into the cavity, we replace the

tapered optical fiber with diamond waveguides fabricated in close proximity to the ring and racetrack resonators (Fig. 51). In addition, polymer in and out-coupling pads consisting of SU-8 resist with a 3 μm x 3 μm cross-section are defined in a second e-beam lithography step to extend the diamond waveguides to both ends of the sample. This procedure improves the coupling between an optical (lensed) fiber to the on-chip diamond waveguide[47]. To ensure optimal coupling between the diamond waveguide and the polymer pads the diamond waveguides are adiabatically tapered. Figure 51a shows a SEM image of a representative diamond race-track resonator on a SiO_2/Si substrate with extended diamond waveguides.

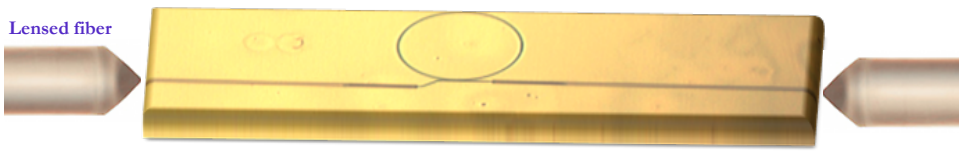

Figure 50: Schematic of the waveguide integrated measurement. An optical image of a diamond ring resonator next to a diamond waveguide is shown along with SU-8 pads extending the diamond waveguides to the end of the chip. Lensed fibbers are used for coupling light in and out of the device.

Lensed fibers (Oz optics) are used to couple light into and out of the cleaved facets of the device (Fig. 50). An outline of the experimental setup and the butt-coupling technique used here are described in detail by Deotare et al [47]. A transmission spectrum of a typical ring resonator device, shown in figure 51b, reveals resonator modes with Q factors as high as 30,000. In this case, an overall transmission loss of

12 dB is inferred. To further improve the coupling efficiency as well as increase the cavity Q factor, a 2 μm thick SiO_2 layer is deposited on top of our devices (after polymer pads are defined) using plasma enhanced chemical vapour deposition (PECVD). A different sample from the one shown in figure 51a was used here with a 330 μm resonator length. After cleaving, the sample facets are polished to maximize the fiber-coupling and to avoid any scrambling of polarization due to facet imperfections. Using this approach an order of magnitude increase in coupling efficiency is observed, and an overall transmission loss down to 2 dB (1 dB/facet) is inferred for the best device. Both TE and TM modes are identified, with TE modes usually having higher Q factors than TM modes (Figure 52a and 52b respectively). Q factors as high as $\approx 2.5 \cdot 10^5$ are obtained from fits to the experimental data. The increase in Q factor is attributed to the reduced scattering losses resulting from the reduced index contrast between the diamond core and the silica cladding. We estimate the waveguide propagation loss [113] to be 1.7 dB/cm from transmission data (Q factor and on-resonance transmission dip), assuming undercoupled devices. Since this estimation accounts for scattering, absorption and bending losses of the ring, it provides an upper limit for the diamond waveguide propagation loss.

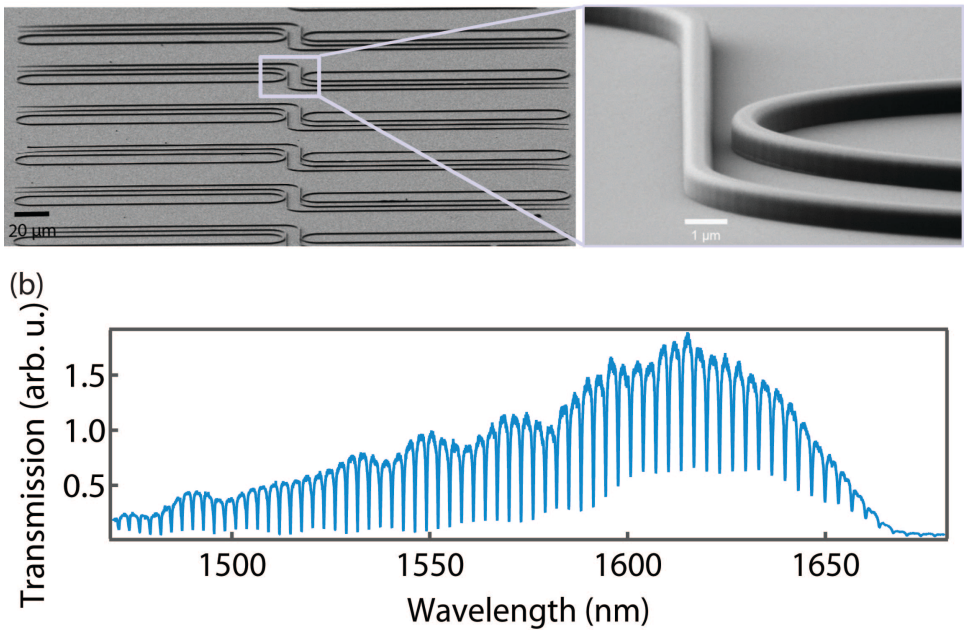

Figure 51: (a) SEM micrograph of an array of diamond racetrack resonators ($330\,\mu\mathrm{m}$ length) coupled to diamond waveguides. Coupling polymer pads are not shown here. Inset: Close-up of the waveguide-resonator coupling region. The height, width and gap size of the devices are in the range of $600 - 700\,\mathrm{nm}$, $550 - 650\,\mathrm{nm}$ and $450 - 500\,\mathrm{nm}$ respectively. **(b)** Transmission spectrum obtained from a $314\,\mu\mathrm{m}$ long race-track resonator. Q-factors as high as 30,000 are observed for devices without silica top cladding.

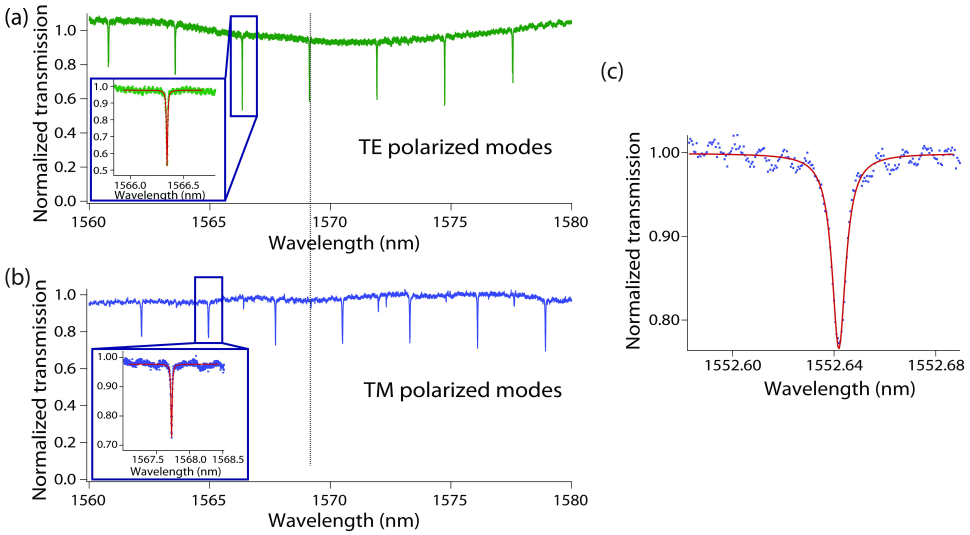

Figure 52: (a) Q-factor of racetrack resonators can be increased by capping them with SiO_2 (deposited by PECVD). Both TE and TM modes are supported, as shown in **(a)** and **(b)** respectively. Lorentzian fits reveal Q-factors of 125,000 for TE modes and 76,000 for TM modes. **(c)** The highest Q-factor measured (TE resonance) is 250,000.

8.4 Split modes and nonlinear bistability signatures

Scattering along the resonator's surfaces or inside the diamond ring can cause the initially degenerate counter-propagating modes to couple, which is referred to as intracavity backscattering [25, 67, 68, 95]. The characteristic signature of this intermode coupling is the splitting of the modes as seen in figure 53b. The response of the system can be analyzed by the following set of coupled

mode equations [95]

$$\frac{da_+}{dt} = -(\gamma_t/2 + i\Delta\omega_0)a_+ + i\beta a_- + \kappa s \tag{8.8}$$

$$\frac{da_-}{dt} = -(\gamma_t/2 + i\Delta\omega_0)a_- + i\beta a_+ \tag{8.9}$$

where $a_\pm$ represent the amplitudes of clock-wise and counter clock-wise ring resonator modes, γ_t the decay rate, β the coupling rate between the two modes, s the amplitude of the input pump field in the coupling waveguide and κ the coupling rate between the waveguide and the resonator. The detuning between excitation and resonance frequency (of the degenerate mode) is denoted as $\Delta\omega_0$. The observed splitting in the modes is most likely caused by scattering due to fabrication imperfections as will be discussed in the next chapter. Further improvements in fabrication, and EBL in particular, mostly eliminates the splitting accompanied with higher Q factors.

Finally, we observed the signatures of optical bistability in our devices for large input powers (Figure 53a,c). With increasing input power the cavity resonance shows a characteristic bistable lineshape with a red-shift and a steep drop-off as the laser is scanned from lower to higher wavelengths. The bistability threshold power is estimated to be 100 mW inside the waveguide for a device with a Q factor of $1.22 \cdot 10^5$. The observed nonlinearity stems most likely from a

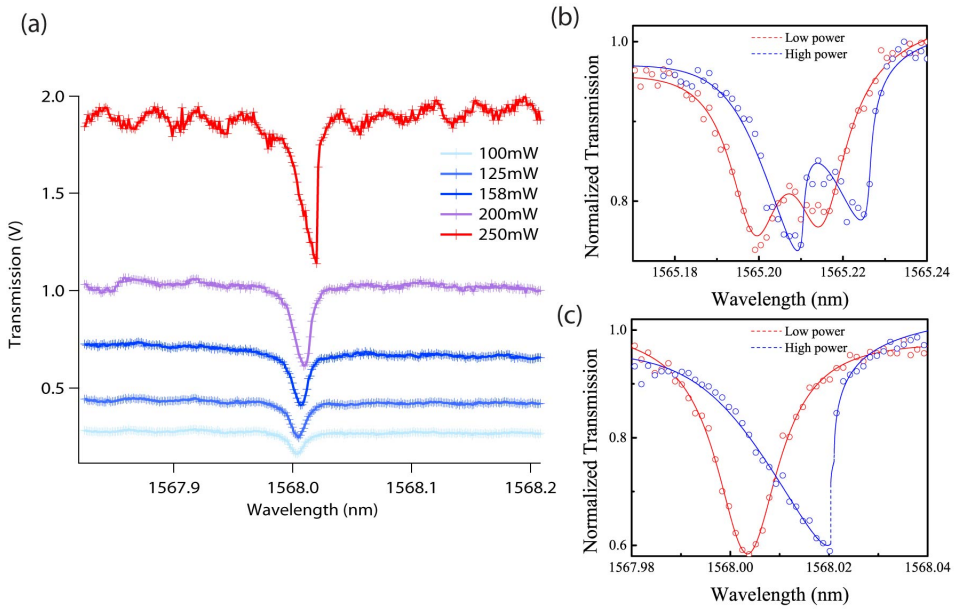

Figure 53: (a) Mode behavior as a function of power reveals optical bistability at high pump powers. **(b)** Mode splitting is observed, indicative of coupling between clockwise and counter-clockwise traveling modes due to scattering. **(c)** Non-split mode of the same device at low (red) and high (blue) pump powers shows signature of optical bistability at high pump powers.

combination of the optical Kerr effect (intensity dependent refractive index) due to the $\chi^{(3)}$ nonlinearity of diamond, and the thermo-optic effect originating from the surrounding silica. Time-dependent studies, could provide more insight to the origin of nonlinearity [158]. We do note, however, that the wide bandgap of diamond makes nonlinear effects due to multi-photon absorption that plagues Si photonics at telecom wavelengths highly unlikely. Similarly, free-carrier dispersion is not a likely origin for the nonlinear effects. The thermal contributions can be suppressed by using a substrate with higher thermal conductivity than silica.

So far, the operation of high-Q diamond race-track resonators integrated with low-loss diamond waveguides at telecom wavelengths has been demonstrated. The integrated diamond photonic platform presented here is the first step towards integrated frequency combs and Raman lasers based on diamond. Owing to diamond's large linear and nonlinear refractive index thresholds for parametric oscillation [81] and Raman lasing to be 300 mW and 10 mW, respectively, for devices with optimal geometries having Q-factors of 250,000. The optimization of the fabrication method and waveguide - ring coupling section will result in a higher coupling efficiency and in a higher optical power transfer from the waveguide to the ring thus further increasing the efficiency of our device. These improvements in fabrication will be discussed in the following chapter along with

results of optical parametric oscillations in diamond resonators.

Precise measurements are really something that you can and should be passionate about. Accurate measurements really mark the beginning of modern science. Whenever you can measure something more precisely than before, you're likely to find something new, because you can look where no-one has looked before.

Theodor Hänsch, during his Nobel Lecture 2005

9

Optical Parametric Oscillations

In this chapter we present the nonlinear optical response of waveguide coupled integrated diamond ring resonators above parametric oscillation threshold. Improvements in design and fabrication allow for ring resonators with record-high Q factors exceeding one million and finesses of 4,000 at telecom wavelengths [78, 79]. Parametric

oscillation thresholds as low as 25 mW (coupled in the waveguide) for Q factors of $1 \cdot 10^6$ have been obtained. Parametric oscillation has been observed into a total of 20 lines over a span of 165 nm. The power converted into the lines was up to 1.1% of the pump power. Furthermore, the first measurement of the nonlinear refractive index at telecom wavelength range in diamond has been performed and a value of $n_2 = 8.2 \cdot 10^{-20}\,\mathrm{m}^2/\mathrm{W}$ was experimentally obtained.

9.1 Introduction

On-chip nonlinear conversion processes of optical wavelengths in diamond is appealing for the generation of novel and fast broadband light sources, single photon conversion and frequency combs. For instance, the large bandgap of diamond combined with low absorption losses make diamond attractive for high repetition rate laser sources at wavelengths that are otherwise hard to reach. In addition, the existence and exploration of color centers in diamond as single photon sources make nonlinear single photon conversion on-chip a promising route for diamond nonlinear photonics. As host of numerous color centers that are of particular interest for quantum information science, sensing and cryptography, their integration with telecommunication networks via nonlinear single photon conversion intersects quantum communication with optical information processing. Finally, an on-chip frequency comb, covering large wavelength ranges, is

intriguing for high precision metrology and measurements of an unknown frequency. Optical frequency combs [170] have been explored from UV, VIS to NIR and are now commercially available for high precision spectroscopy (MenloSystems) [44]. Aside from the laser based frequency comb approach, remarkably, equidistant frequency markers can also be generated over a large span via the nonlinear Kerr effect with high repetition rates in the GHz range [44]. So far, integrated devices suitable for on-chip nonlinear optics have been limited to silica [144], Si and Si_3N_4 [108, 133] . However, none of these materials have shown to be compatible with nonlinear optics in the visible. Diamond, who has recently emerged as a promising platform for on-chip photonics, intrinsically combines the advantages of low absorption losses within its large transmission window with a relatively high nonlinear refractive index and hence could be used to implement frequency combs in the VIS and even UV. Furthermore, its high thermal conductivity allows for high power operation.

9.2 Design and fabrication of ring resonators

Building upon the preliminary promising results of chapter 8, the ring resonator design has been adjusted for an efficient design for four wave mixing (FWM). Owing to an inversion symmetry in crystal lattice, diamond's lowest order nonzero nonlinear susceptibility is $\chi^{(3)}$

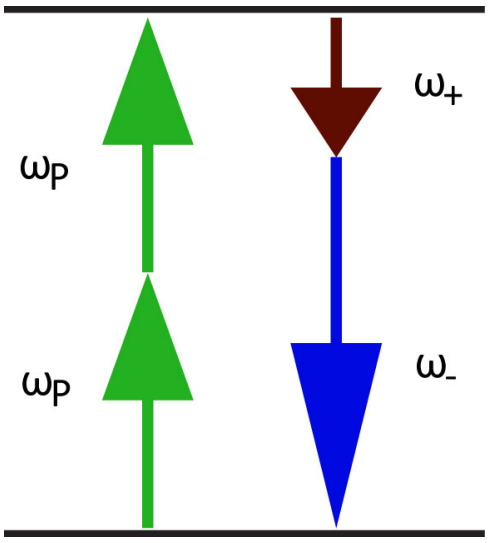

Figure 54: Schematic of four wave mixing process where two pump photons are converted into two photons with differing frequencies while conserving energy.

[26] but is still denoted as n_2 here (and in literature [59]):

$$n = n_0 + n_2 I = n_0 + \frac{12\pi^2 \chi^{(3)}}{n_0 c}$$

where n_0, I and c are the linear refractive index, the pump intensity and the speed of light. A third-order nonlinear parametric process where two pump photons at frequency ω_P are converted to two different photons at ω_+ and ω_- (denoted as signal and idler), such that energy conservation is satisfied by $2\omega_p = \omega_+ + \omega_-$ (Fig. 54 is called four-wave mixing (FWM). The FWM gain scales with the pump intensity, and the pump power requirement can be reduced by confining the light to nano-waveguides [59]. The FWM efficiency can

be drastically increased by using high-Q resonators [1, 168], where photons make multiple round trips on resonance, resulting in the optical intensity to be enhanced by a factor of the finesse. Optical parametric oscillation (OPO) is achieved when the round trip FWM gain exceeds the loss in the resonator - bright coherent light being spontaneously generated at the signal and idler wavelengths - analogous to a laser above threshold.

In addition, FWM also entails momentum conservation, or phase-matching which implies

$$\Delta k = 2\gamma P_{pump} - \Delta k_L \sim 0$$

[59, 71]. Here, the second term $\Delta k_L = 2k_{pump} - k_+ - k_-$ is the phase mismatch due to the linear dispersion, k_{pump}, k_+ and k_- are the pump, signal and idler wavenumbers, respectively, $\gamma = \omega_{pump} n_2 / c A_{eff}$ is the effective nonlinearity and A_{eff} the effective optical mode area. The first term arises from the nonlinear response to the strong pump, which imposes self-phase modulation (SPM) on itself and cross-phase modulation (XPM) on the generated modes that is twice as large as the SPM. This nonlinear phase shift needs to be compensated for by the linear dispersion i.e. $\Delta k_L > 0$. Consequently, the group velocity dispersion (GVD) of the optical mode needs to be anomalous around

the pump wavelength [59, 71], or

$$\text{GVD} = -\frac{\lambda}{c} \cdot d^2 n_{eff}/d\lambda^2 > 0$$

, where n_{eff} is the effective index of the waveguide mode, λ is the wavelength and c is the speed of light in vacuum. For a resonator, this implies that the frequency separation between adjacent modes, $\nu_m - \nu_{m-1}$ (or the free-spectral range, FSR), increases as a function of the mode number m. The resonator dispersion D, given by the change in FSR ($\nu_{m+1} + \nu_{m-1} - 2\nu_m$), thus needs to be positive for modes around the pump wavelength [44, 81]. The unequal frequency spacing of the resonator modes due to anomalous dispersion is compensated by nonlinear optical mode "pulling" i.e a shift in the resonance frequencies caused by SPM and XPM due to the pump [44, 96].

In this chapter we account for the material dispersion of diamond that is normal while the oxides surrounding it have anomalous dispersion at telecom wavelengths. The net waveguide dispersion can be engineered to be anomalous by appropriately designing the cross-sectional dimensions [59, 81, 108, 133]. However, as mentioned before, our fabrication technique relies on thin SCD films that are typically wedged due to the mechanical polishing process of the surfaces resulting in a thickness change of at least $> 300\,\text{nm/mm}$ across the sample [79]. Therefore, the waveguide design has to be robust towards film thickness changes and imperfections due to

fabrication. A finite-element mode solver (COMSOL) is used to simulate the diamond ring resonator dispersion. The material dispersion of both the thermally - grown SiO_2 underneath the diamond devices and the capping SiO_2 deposited via plasma-enhanced chemical vapor deposition (PECVD) are evaluated in ellipsometry measurements and their data included in the simulations.

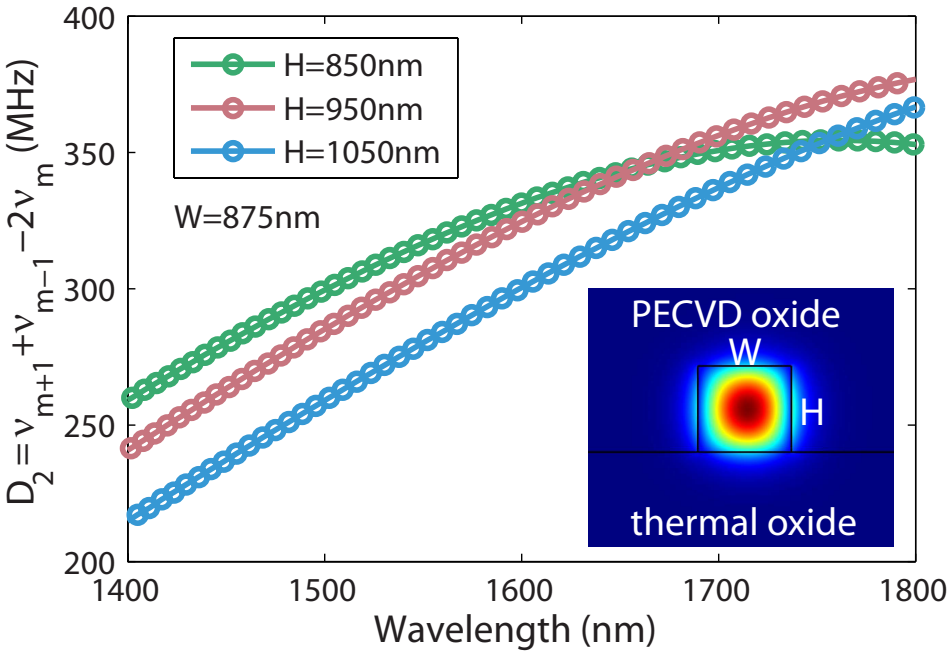

Figure 55: Robust dispersion engineering allows for a range of ring cross-sections yielding anomalous dispersion for the ring resonator modes in the telecom wavelength range. Inset shows the optical mode profile for the transverse-electric (TE) mode in the silica - cladded diamond waveguide.

Figure 55 shows that for the optimized geometry, the resonator dispersion can be made anomalous in the wavelength range of interest for a range of film thickness (or waveguide height). For a ring

resonator of radius $20\,\mu$m, anomalous dispersion for the transverse-electric (TE) mode can be achieved in the $1400 - 1700\,$nm wavelength range for widths $800 - 900\,$nm and heights $500 - 1000\,$nm. In order to design the gap between the coupling waveguide and the ring resonator, 3D Finite-Difference Time Domain (FDTD) simulations (Lumerical) are used. For the above mentioned cross-sectional dimensions, gaps of $400 - 500\,$nm yield coupling Q-factors $Q_C > 5 \cdot 10^5$.

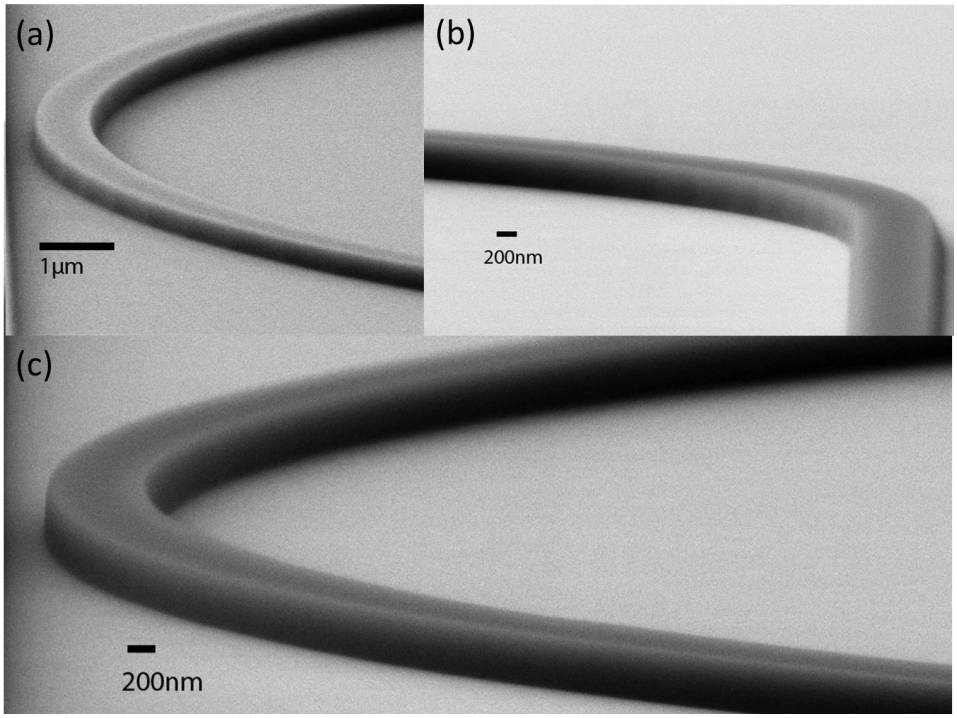

Figure 56: SEM micrographs of ring **(a)** and waveguide **(b)** mask sections that have periodic stripes due to EBL writing technique. **(c)** Improving the segmenting and order of EBL writing allows for smooth masks.

Using the designed parameters, waveguide integrated SCD ring

resonators of radii 20- and 30 μm are fabricated on a SiO_2/Si chip according to the method presented in chapter 8. Additionally, improvements in the EBL technique are pursued. The periodic lines observed in the ring and curved waveguide sections (see figure 56a,b and chapter 8 are assumed to cause an intermode splitting and limit the loaded Q factor. The origin of these lines lie in the way EBL segments and writes the device according to the prepared file for the tool. Improvements in the writing technique - while still not perfect - result in the absence of the segmenting of waveguide and ring resonator. Specifically, using a simple polyline in AutoCAD that has the linewdith of the ring/waveguide width segments the design into continuous ultra-small segments that prevent the occurrence of the periodic lines in the devices (Fig. 56c). Additionally, further improvements can be pursued using the Elionix compatible software Layout Beamer. Using the former method, we fabricated arrays of ring resonators (Fig. 57).

9.3 Results

Measurements are performed in a similar way as in section 8.3. The overall sample insertion loss is inferred to be ~ 8 dB (We note, that all data shown in this chapter was taken from the same device unless noted otherwise). First, transmission measurements are performed by

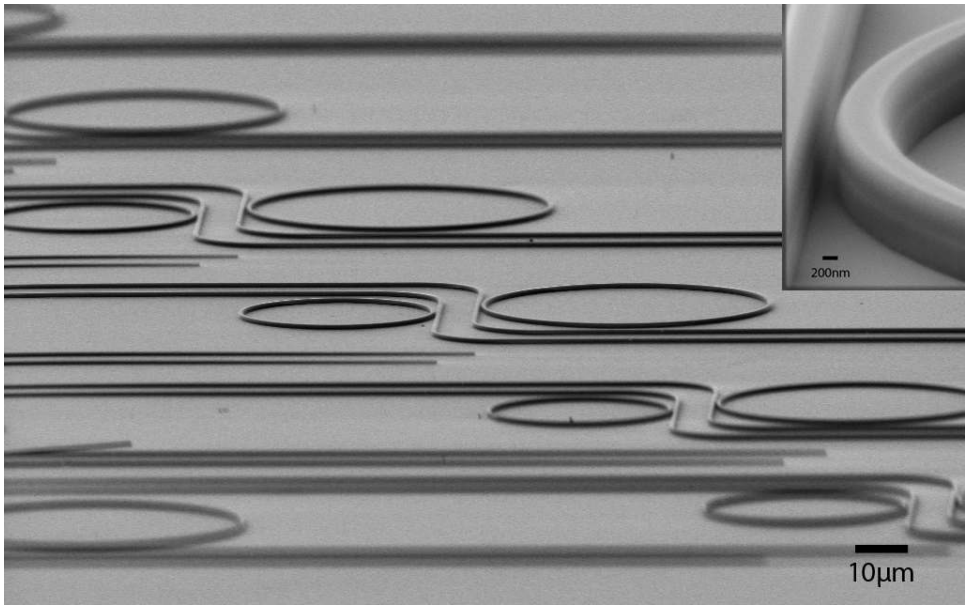

Figure 57: SEM image of an array of waveguide-coupled SCD ring resonators on a SiO_2/Si chip. Inset shows magnified view of the ring - waveguide coupling section.

sweeping a continuous - wave laser (Santec TSL-510) across the telecom wavelength range to measure the resonator Q-factors and the coupling of the bus - waveguide to the rings (Fig. 58a). Most devices are found to be slightly under-coupled. Loaded Q-factors (Q_L) as high as $1 \cdot 10^6$ are measured for the TE mode, with most devices having $Q_L > 2 \cdot 10^5$. To ensure an accurate resonance linewidth measurement, a radio-frequency (RF) phase modulation is imparted on the input light which generates sidebands around the main resonance (Fig. 58b). Comparing the measured distance between the dips with the applied RF frequency ($1 - 3\,\mathrm{GHz}$) allows for a precise calibration of the wavelength/frequency axis [40]. Using this method,

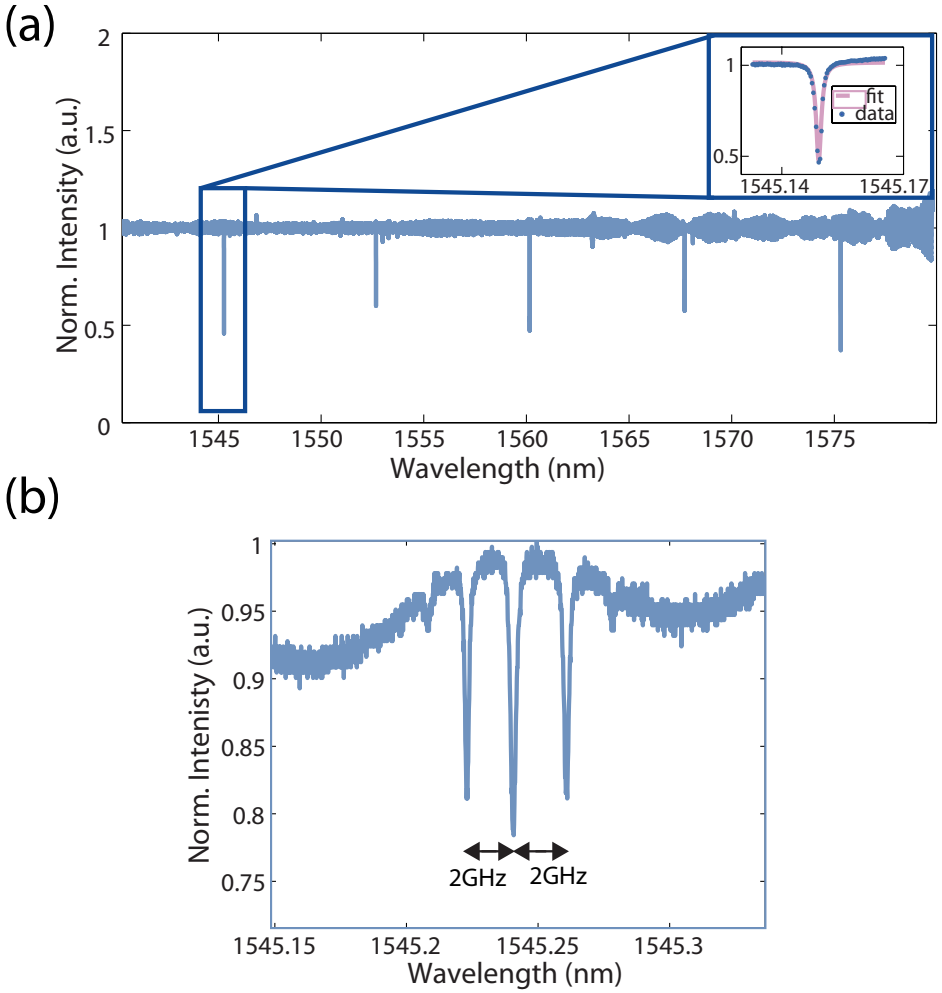

Figure 58: **a** Normalized transmission spectrum of a ring resonator reveals high Q-factor modes. The radius of the ring is $20\,\mu\mathrm{m}$, corresponding to a free-spectral range (FSR) of $\sim 7.5\,\mathrm{nm}$ ($\sim$925 GHz). Inset: A loaded Q-factor of $Q_L \sim 1 \cdot 10^6$ is inferred from a Lorentzian fit for the mode at $1545.1\,\mathrm{nm}$. **b** The input light from the continuous-wave laser scanning across the resonance is phase-modulated at $2\,\mathrm{GHz}$ to generate side-modes and calibrate the wavelength/frequency axis accurately, yielding an actual $Q_L \simeq 1.14 \cdot 10^6$ for the same mode.

we measure the highest Q to be $\sim 1.14 \cdot 10^6$.

Next, we describe the observation of optical parametric oscillation in the diamond ring resonators. The input laser is sent through an erbium-doped fiber amplifier (EDFA, Manlight) to obtain a high pump power. The EDFA was directly spliced to a lensed fiber (OZ Optics) that was fed through a input polarizer. The pump is initially tuned slightly blue to the resonance and then slowly moved into resonance. The power absorbed by the ring causes a thermal red - shift of the resonance potentially arising due to the heating of the silica cladding. While tuning the laser deeper into resonance, the output light is monitored on an optical spectrum analyzer (OSA, HP 70952B). As the detuning of the pump to the resonance minimum decreases, more power is transferred to the ring resonator, eventually resulting in the generation of pairs of new lines - at integer multiples of the resonator FSR - around the pump. The first sidebands are generated at mode numbers $|m| = \sqrt{\kappa/D \cdot (\sqrt{P_{in}/P_{th} - 1} + 1)}$ away from the pump [81], where κ represents the resonator linewidth (cavity decay rate), D is the resonator dispersion discussed earlier, P_{in} is the input pump power and P_{th} is the threshold pump power for parametric oscillation (Fig. 59). Tuning the pump deeper into resonance generates several new modes further away from the pump, finally resulting in a spectrum of multiple lines with a frequency spacing given by the FSR (Fig. 60). The pump power coupled into

the resonator is intrinsically stabilized during this entire process achieving a thermal 'soft-lock' [45], and stable oscillation is observed for up to $\sim 20\,\mathrm{min}$ (limited by stage drifts).

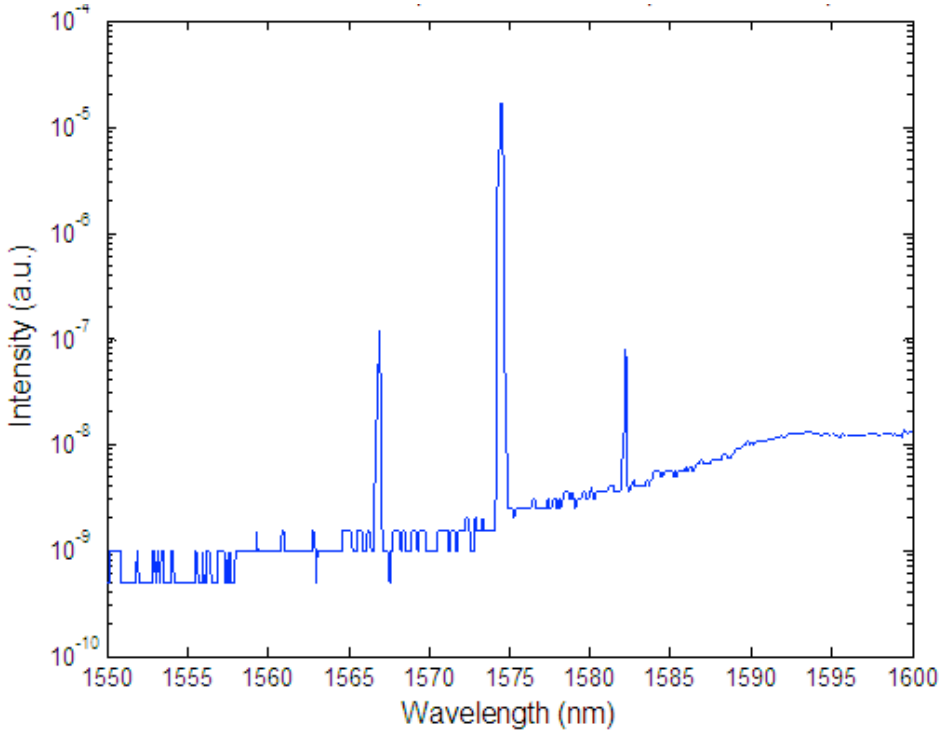

Figure 59: Onset of parametric oscillation is displayed for a pump power of $25\,\mathrm{mW}$ in the waveguide.

The performance of our diamond OPO device is studied as a function of pump wavelength. The same ring is pumped at two different resonances, first at $\sim 1553\,\mathrm{nm}$ (C-band) and then at $\sim 1599\,\mathrm{nm}$ (L-band), and their output spectra compared (Fig. 61). For the same pump power of $\sim 80\,\mathrm{mW}$ in the waveguide, the former

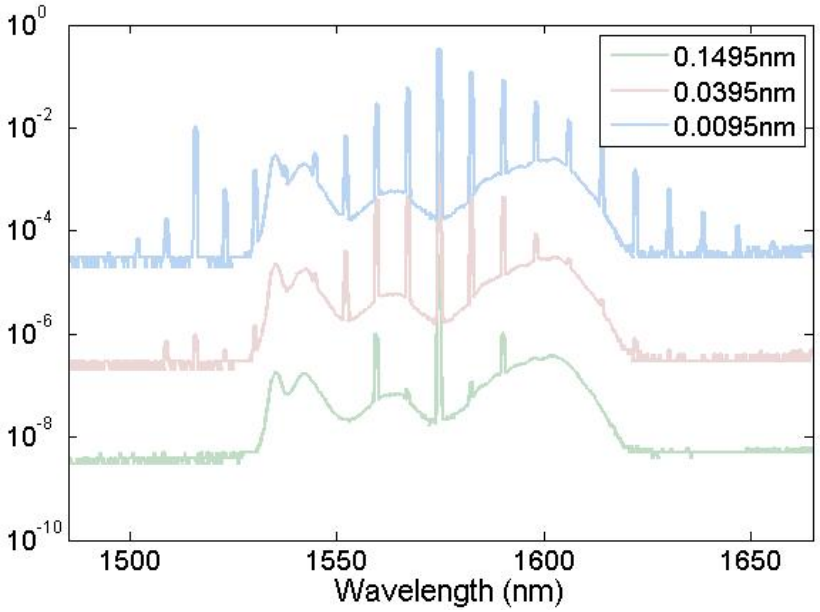

Figure 60: Optical parametric oscillation spectrum as a function of detuning from resonance minimum. New frequencies are generated in the spectrum as the pump wavelength is tuned towards the mode transmission minimum starting from a blue detuned position. Thermal red-shift of the resonance intrinsically provides stabilization of the pump power coupled into the resonator.

generates 10 new lines spanning a range of 75 nm while the latter generates 20 lines spanning a range of 165 nm. This effect can be explained by an increased power drop into the ring for a larger ring - waveguide coupling efficiency towards longer wavelengths in the case of under coupled devices. Additionally, this effect might be associated with better phase matching for longer wavelengths due to the dispersion of the device.

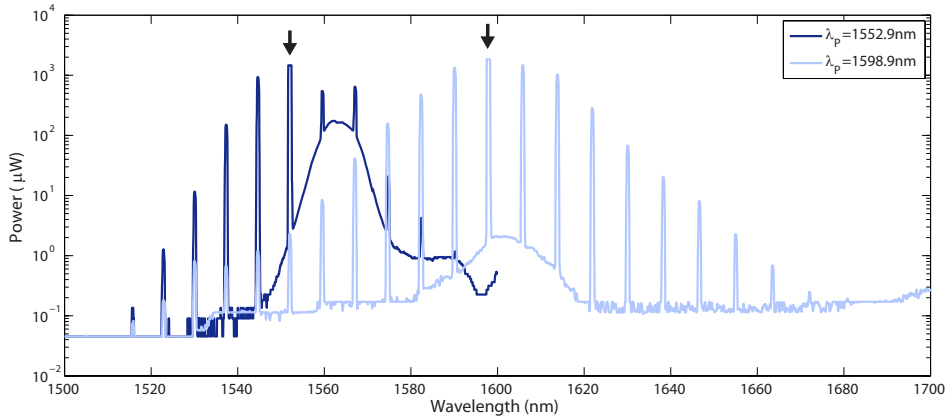

Figure 61: Optical parametric oscillation spectra for two different pump wavelengths. The generated spectrum from the same ring resonator for two different pump positions, 1553 nm and 1599 nm. The pump power is the same in each case (80 mW in the waveguide). A total of 20 new lines is observed for the 1599 nm pumping, while 10 lines are observed for the 1553 nm pumping. The trend can be explained by higher coupling efficiency between the bus-waveguide and the ring as well as better phase matching for longer wavelengths.

Finally, to determine the threshold for parametric oscillation, the output power in the first generated sideband is measured as a function of pump power. Fig. 62a shows the data for a device

pumped at a resonance near 1575 nm with $Q_L = 9.7 \cdot 10^5$, where we infer a P_{th} of only ~ 25 mW in the waveguide and a conversion slope efficiency of ∼2%. For pump powers above threshold, oscillation occurs into multiple new modes limiting the power converted to the first sideband. We infer the total power in a total of 19 generated modes combined to be 3.4 mW for an input pump power of 316 mW and hence an overall conversion efficiency of $\sim 1.1\%$.

The threshold power (P_{th}) for parametric oscillation arising from the third-order nonlinearity (FWM) can be also estimated from theory as [120]:

$$P_{th} \simeq 1.54 \left(\frac{\pi}{2}\right) \frac{Q_C}{2Q_L} \cdot \frac{n_0^2 V}{n_2 \lambda_P Q_L^2} \tag{9.1}$$

where λ_P is the pump wavelength, V is the resonator mode volume and n_0 is the linear refractive index (∼2.4 for diamond). By measuring P_{th} for various devices with different Q-factors, the nonlinear refractive index n_2 can be estimated in the wavelength range around the pump. The measured P_{th} for eight different devices on the same chip is depicted in figure 62b. From this data, we report the first measurement of the nonlinear refractive index of diamond in the telecom range as $n_2 = (8.2 \pm 3.5) \cdot 10^{-20}\,\mathrm{m^2/W}$. The value obtained for n_2 at telecom wavelengths is about a factor of 1.5 smaller than the value reported for visible wavelengths [26, 107], which is expected as per the theoretical prediction of the dispersion of the

nonlinear susceptibility (longer wavelengths being more off-resonant from the bandgap) [107]. Fig. 62b also shows that most of the devices measured are on the under-coupled side, consistent with the expectations form the transmission measurements.

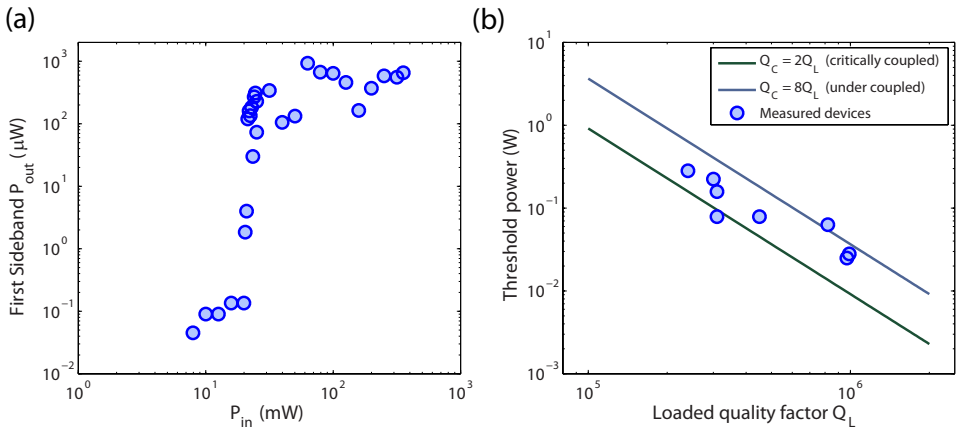

Figure 62: Parametric oscillation threshold and dependence on Q-factor. **a** Output power in the first generated side-mode as a function of input pump power (both estimated in the waveguide) for a device with $Q_L = 9.7 \cdot 10^5$. The threshold for oscillation is observed to be $25\,\mathrm{mW}$. **b** Threshold power for oscillation as a function of loaded quality factor Q_L. The data is measured for eight different devices (blue dots). Threshold powers roughly follow the theoretically predicted trend of being inversely proportional to Q_L^2, with most devices being slightly under-coupled i.e. $Q_C > 2Q_L$ (consistent with the transmission measurements). The black line denotes critical coupling (100% transmission dip on-resonance), while the blue line denotes under-coupled resonators (50% transmission dip on-resonance).

In summary, we demonstrate an on-chip OPO operating at telecom wavelengths based on a fully-integrated, monolithic, single-crystal diamond micro-resonator. The OPO uses the $\chi^{(3)}$-nonlinearity of diamond to realize FWM gain for side-modes around the pump

frequency. Ring resonators with Q-factors near one million enable oscillation threshold powers as low as 25 mW in the bus-waveguide, and 20 sidebands spanning a wavelength range of 165 nm are generated with pump powers less than 100 mW. We also report the first measurement of the nonlinear refractive index of diamond in the telecom wavelength range as $n_2 = (8.2 \pm 3.5) \cdot 10^{-20}\,\mathrm{m}^2/\mathrm{W}$. Coupling higher pump powers into the OPO device should enable the generation of broadband, high-repetition-rate optical frequency combs that are desirable for numerous applications [44, 60, 81, 97, 133, 153]. As with most other on-chip OPO's aiming for octave spanning comb generation, diamond has an inversion symmetry crystal inhibiting any $\chi^{(2)}$ processes so the on-chip generation of the second harmonic of an octave spanning comb is inherently inhibited and would need to be done either via a different $\chi^{(2)}$ material integrated on-chip (e.g. Lithium niobate, LBO, KTP etc.) or externally via a $\chi^{(2)}$ nonlinear crystal. Another unknown factor remaining is the nature of the carrier-envelope phase shift δ and how its feedback could be implemented on-chip.

The large thermal conductivity of diamond along with its small thermo-optic coefficient should enable the fabrication of robust devices capable of handling high powers. Given diamond's large transparency window from the UV to the IR, in addition to the absence of loss mechanisms like two-photon absorption and

free-carrier absorption plaguing other material systems for photons up to $\sim 2.75\,\mathrm{eV}$, this technology can be transferred to other wavelengths where on-chip devices have not yet been realized in other material systems, e.g. the visible range. Integrating these devices with sources of non-classical light, such as single-photon sources based on color-centres in diamond [55, 56, 76], is another intriguing possibility. Our work thus opens up an avenue for research into diamond nonlinear photonics, where all-optical information processing on-chip may be realized at both the classical and quantum level.

Part III

Third part: Le fin

Photons have mass? I didn t even know they were Catholic.

Woody Allen

10

Summary and outlook

In the past 5 years, diamond research has evolved from working with color centers in bulk material or nanocrystals to their controlled integration in nanodevices. Moreover the leap towards integrated nonlinear optics in diamond has been achieved which opens a new route for diamond photonics. However, while progress in the field has

been tremendous, there are outstanding challenges that still need to be addressed. In particular, the intriguing applications within the scope of quantum networks based on NV centers rely on their controlled integration in devices which likely necessitates the use of implanted NV centers. While initial results for diamond devices such as nanowires, plasmonic apertures and integrated devices have been demonstrated in this thesis and will be summarized in this chapter, challenges are pointed out for the next generation of diamond photonics.

Implantation of NV centers So far, a good NV center implantation throughput was observed in the case of shallow implanted NV centers in nanowires where up to 30% of nanowires contained single NV centers [116]. An outstanding challenge that needs to be resolved before advancing to more involved quantum optics studies of NV centers embedded in nanophotonic devices, is obtaining stable, narrow - ZPL NV centers embedded in nanodevices at low temperature.

Nanowires An order of magnitude more efficient exchange of pump and emitted single photons has been obtained in form of a NV center-coupled nanowire geometry ($\approx 2 \cdot 10^5$ CPS) compared to the emission in bulk ($\approx 2 \cdot 10^4$ CPS). Its single photon count level is also higher compared to nanocrystals that usually emit in the high

10^4 CPS range as well [20]. Since the nanowire provides directional emission, it could be integrated with a simple lensed fiber. Overall, the increased collection efficiency of the nanowire geometry facilitates optical studies of the NV center. Furthermore the scalability of making millions of nanowires on the same chip can be leveraged in entanglement measurements that rely on both high single photon flux as well as having identical ZPLs of NV centers which represents a statistical issue. For these measurements, a low temperature environment is necessary to resolve the ZPL of the NV centers. However, as mentioned before, low-temperature studies of implanted NV centers in diamond nanowires have not yet offered photo-stability and narrow ZPLs potentially due to surface effects originating from the etch procedure, surface termination and surface traps.

Plasmonic resonators A broadband enhancement of spontaneous emission has lead to a sixfold increase in the emission rate of NV centers placed in plasmonic ultra-small mode volume resonators. However, photon collection efficiency in the system remains limited by losses to surface plasmons as well as total-internal-reflection at the collection (bottom) facet of the diamond substrate, so that only about 5% of the total emitted photons are collected. A modified geometry where characterization is performed from above the sample should result in even larger Purcell effects [29]. Future developments thus include the addition of gratings

to coherently scatter surface plasmons into the critical cone to improve collection efficiency and potentially lead to beaming [109]. Potential applications of the diamond-plasmon system include improved optical readout for NV center-based nanoscale magnetometry [116], [151] and faster rates for quantum communication and computation processes based on either spin or photonic qubits (Fig. 3b). However, practical implementation of the device would require a sufficiently long spin coherence time as well as stable emission lines at low temperature for the shallow-implanted NV centers, which remain to be confirmed in experiments.

Planar integration Integrated diamond photonics has recently emerged as a promising platform for quantum science. Photonic crystal and ring cavities, as well as optical waveguides and gratings have been demonstrated using this approach. Furthermore, on-chip single photon routing has been achieved for NV centers in planar ring resonators coupled to waveguide. Small mode volume ($2(\lambda/n)^3$) PCCs have been sculptured from diamond having Q-factors as high as 6,000. An spontaneous emission rate enhancement of the NV center's ZPL of a factor of 7 has been inferred from low temperature measurements of natural NV centers. The approach used here allows for a large tuning range of 23 nm in irreversible blue tuning and 7 nm in reversible red tuning. Since PCCs provide a much higher Q/V ratio compared to the ring resonators (a factor of 15 merely due to

the smaller mode volume), much stronger light-matter interaction between NV centers and the cavity field may be achieved using this geometry. At the same time the likelihood of having an NV center coupled to the cavity region is reduced. Moreover, surface effects such as surface traps and functionalization have greater impact on implanted NV centers that are located in close proximity to the surface. Therefore, further studies and developments of surface treatments and annealing protocols are needed to enable wide-spread applications of diamond photonic crystal cavities. So far, Purcell enhancement into the ZPL up to 70 has been reported [56] which is up to 6 times higher than what has been achieved with ring resonators [55]. Potentially, novel techniques, based on bulk nanomachining of diamond [30] might further facilitate the developments in the field of quantum diamond photonics.

Nonlinear optics in diamond The field of nonlinear optics in integrated diamond devices has just been developed and requires further intense studies of the optical parametric oscillation processes. Initial results on optical parametric oscillations in butt coupled diamond ring resonator devices have been observed. However, the range over which lines can be generated still needs to be characterized to potentially allow for frequency comb generation. Exploring nonlinear processes in the visible wavelength range is another intriguing route, along with the integration and conversion of single

photons of diamond's color centers.

References

[1] P. P. Absil, J. V. Hryniewicz, B. E. Little, P. S. Cho, R. A. Wilson, L. G. Joneckis, and P.-T. Ho. Wavelength conversion in gaas micro-ring resonators. *Opt. Lett.*, 25 (8):554, 2000.

[2] I. Aharonovich, S. Castelletto, D. A. Simpson, A. Stacey, J. McCallum A. D. Greentree, and S. Prawer. Two-level ultrabright single photon emission from diamond nanocrystals. *Nano Lett.*, 9 (9):3191, 2009.

[3] I. Aharonovich, A. D. Greentree, and S. Prawer. Diamond photonics. *Nature Photon.*, 5:397, 2011.

[4] I. Aharonovich, J. C. Lee, A. P. Magyar, B. B. Buckley, C. G. Yale, D. D. Awschalom, and E. L. Hu. Homoepitaxial growth of single crystal diamond membranes for quantum information processing. *Adv. Matter.*, 24 (10):OP54, 2012.

[5] B.-H. Ahn, J.-H. Kang, M.-K. Kim, J.-H. Song, B. Min, K.-S. Kim, and Y.-H. Lee. One-dimensional parabolicbeam photonic crystal laser. *Opt. Exp.*, 18 (6):5654, 2010.

[6] A. V. Akimov, A. Mukherjee, C. L. Yu, D. E. Chang, A. S. Zibrov, P. R. Hemmer, H. Park, and M. D. Lukin. Generation of single optical plasmons in metallic nanowires coupled to quantum dots. *Nature*, 450:402–406, 2007.

[7] V. R. Almeida, R. R. Panepucci, and M. Lipson. Nanotaper for compact mode conversion. *Opt. Lett.*, 28 (15):1302–1304, 2003.

[8] Patent application. Synthetic diamond materials for quantum and optical applications and methods of making the same. 2013.

[9] D. K. Armani, T. J. Kippenberg, S. M. Spillane, and K. J. Vahala. Ultra-high-q toroid microcavity on a chip. *Nature*, 421: 925, 2003.

[10] T. M. Babinec, J. T. Choy, K. J. M. Smith, M. Khan, and M. Loncar. Design and focused ion beam fabrication of single crystal diamond nanobeam cavities. *J. Vac. Sci. Technol. B*, 29 (1):010601, 2010.

[11] T. M. Babinec, B. J. M. Hausmann, M. Khan, Y. Zhang, J. Maze, P. R. Hemmer, and M. Loncar. A diamond nanowire single photon source. *Nature Nanotech.*, 5:195–199, 2010.

[12] T.M. Babinec, B.M. Hausmann, J.T. Choy, M. Khan, P.R. Hemmer, and M. Loncar. Quantum photonics with diamond. *IEEE Photonics Society Newsletter*, 25:13, 2011.

[13] G. Balasubramanian, I. Y. Chan, R. Kolesov, M. Al-Hmoud, J. Tisler, C. Shin, C. Kim, A. Wojcik, P. R. Hemmer, A. Krueger, T. Hanke, A. Leitenstorfer, R. Bratschitsch, F. Jelezko, and J. Wrachtrup. Nanoscale imaging magnetometry with diamond spins under ambient conditions. *Nature*, 455 (7213):648–651, October 2008. ISSN 0028-0836. doi: 10.1038/nature07278. URL http://dx.doi.org/10.1038/nature07278.

[14] G. Balasubramanian, P. Neumann, D. Twitchen, M. Markham, R. Kolesov, N. Mizuochi, J. Isoya, J. Achard, J. Beck, J. Tissler, V. Jacques, P. R. Hemmer, F. Jelezko, and J. Wrachtrup. Ultralong spin coherence time in isotopically engineered diamond. *Nature Mater.*, 8:383, 2009.

[15] P. E. Barclay, K. Srinivasan, M. Borselli, and O. Painter. Probing the dispersive and spatial properties of photonic crystal waveguides via highly efficient coupling from fiber tapers. *Appl. Phys. Lett.*, 85 (1):4, 2004.

[16] P. E. Barclay, K.-M. C. Fu, C. Santori, and R. G. Beausoleil. Chip-based microcavities coupled to nitrogen-vacancy centers in single crystal diamond. *Appl. Phys. Lett.*, 95:191115, 2009.

[17] P. E. Barclay, K.-M. C. Fu, C. Santori, and R. G. Beausoleil. Chip-based microcavities coupled to nitrogen-vacancy centers in single crystal diamond. *Appl. Phy. Lett.*, 95:191115, 2009.

[18] I. Bayn, B. Meyler, A. Lahav, J. Salzman, R. Kalish, B. A. Fairchild, S. Prawer, M. Barth, O. Benson, T. Wolf, P. Siyushev, F. Jelezko, and J. Wrachtrup. Processing of photonic crystal nanocavity for quantum information in diamond. *Diam. Relat. Mater.*, 20 (7):937, 2011.

[19] H. Bernien, B. Hensen, W. Pfaff, G. Koolstra, M.S. Blok, L. Robledo, T.H. Taminiau, M. Markham, D.J. Twitchen, L. Childress, and R. Hanson. Heralded entanglement between solid-state qubits separated by 3 meters. *accepted to Nature*, 2013.

[20] A. Beveratos, R. Brouri, T. Gacoin, J.-P. Poizat, and P. Grangier. Nonclassical radiation from diamond nanocrystals. *Phys. Rev. A*, 64:061802(R), 2001.

[21] A. Beveratos, R. Brouri, T. Gacoin, A. Villing, J. P Poizat, and P. Grangier. Single photon quantum cryptography. *Phys. Rev. Lett*, 89:187901, 2002.

[22] K. M. Birnbaum, R. Miller A. Boca, A. D. Boozer, T. E. Northup, and H. J. Kimble. Photon blockade in an optical cavity with one trapped atom. *Nature*, 436:87, 2005.

[23] B. B. Blinov, D. L. Moehring, L.-M. Duan, and C. Monroe. Observation of entanglement between a single trapped atom and a single photon. *Nature*, 428:153, 2004.

[24] W. Bogaerts, P. De Heyn, T. Van Vaerenbergh, K. De Vos, S. Kumar Selvaraja, T. Claes, P. Dumon, P. Bienstman, D. Van Thourhout, and R. Baets. Silicon microring resonators. *Laser Photon. Rev.*, 6 (1):47, 2012.

[25] M. Borselli, T. J. Johnson, and O. Painter. Beyond the rayleigh scattering limit in high-q silicon microdisks: theory and experiment. *Opt. Exp.*, 13 (5):1515, 2005.

[26] R. W. Boyd. *Nonlinear Optics*. Academic Press, 2008.

[27] J. D.B. Bradley, C. C. Evans, J. Choy, O. Reshef, P. Deotare, F. Parsy, K. Phillips, M. Loncar, and E. Mazur. Submicrometer-wide amorphous and polycrystalline anatase tio2 waveguides for microphotonic devices. *Opt. Exp.*, 20:23821, 2012.

[28] R. Hanbury Brown and R. Q. Twiss. Correlation between photons in two coherent beams of light. *Nature*, 177:27–29, 1956.

[29] I. Bulu, T. M. Babinec, B. J. M. Hausmann, J. T. Choy, and M. Loncar. Plasmonic resonators for enhanced diamond nv-center single photon sources. *Opt. Express*, 19:5269, 2011.

[30] M.J. Burek, B.J. Shields, N. P. de Leon, B.M. Hausmann, Y. Chu, Q. Quan, M.D. Lukin, and M. Loncar. Angle-etched free-standing photonic crystal nanobeam cavities in single-crystal diamond. In *CLEO/QELS*, 2012.

[31] M. Cai, O. Painter, and K. J. Vahala. Observation of critical coupling in a fiber taper to a silica-microsphere whispering-gallery mode system. *Phys. Rev. Lett.*, 85 (1):74–77, 2000.

[32] D. E. Chang, A. S. S rensen, E. A. Demler, and M. D. Lukin. A single-photon transistor using nanoscale surface plasmons. *Nat. Phys.*, 3:807–812, 2007.

[33] C.-Y. Chao and L. J. Guo. Biochemical sensors based on polymer microrings with sharp asymmetrical resonance. *Appl. Phys. Lett.*, 83 (8):1527, 2003.

[34] H. Chew. Radiation and lifetimes of atoms inside dielectric particle. *Phys. Rev. A*, 38:3410, 1988.

[35] Y. Chi, G. Chen, F. Jelezko, E. Wu, and H. Zeng. Enhanced photoluminescence of single-photon emitters in nanodiamonds on a gold film. *IEEE Photon. Technol. Lett.*, 23 (6):374, 2011.

[36] L. Childress, J. M. Taylor, A. S. S rensen, and M. D. Lukin. Fault-tolerant quantum communication based on solid-state photon emitters. *Phys. Rev. Lett.*, 96:070504, 2006.

[37] L. I. Childress. *Coherent manipulation of single quantum systems in the solid state*. PhD thesis, The Department of Physics, Harvard University, 2007.

[38] J. T. Choy*, B. J. M. Hausmann*, T. M. Babinec*, I. Bulu*, M. Khan, P. Maletinsky, A. Yacoby, and M. Loncar. Enhanced single photon emission from a diamond-silver aperture. *Nature Photon.*, 5:738, 2011.

[39] Y. Chu and et. al. Coherent optical transitions from implanted nitrogen vacancy centers. 2013.

[40] L. Collot, V. Lefevre-Seguin, M. Brune, J. M. Raimond, and S. Haroche. Very high-q whispering-gallery mode resonances observed on fused silica microsphere. *Europhys. Lett.*, 23 (5): 327, 1993.

[41] J. I. Dadap, G. B. Focht, D. H. Reitze, and M. C. Downer. Two-photon absorption in diamond and its application to ultraviolet femtosecond pulse-width measurement. *Opt. Lett.*, 16 (7):499–501, 1991.

[42] G. de Lange, Z. H. Wang, D. Rist , V. V. Dobrovitski, and R. Hanson. Universal dynamical decoupling of a single solid-state spin from a spin bath. *Science*, 330:60, 2010.

[43] N. P. de Leon, B. J. Shields, C. L. Yu, D. E. Englund, A. V. Akimov, M. D. Lukin, and H. Park. Tailoring light-matter interaction with a nanoscale plasmon resonator. *Phys. Rev. Lett.*, 108:226803, 2012.

[44] P. Del'Haye, A. Schliesser, O. Arcizet, T. Wilken, R. Holzwarth, and T. J. Kippenberg. Optical frequency comb generation from a monolithic microresonator. *Nature*, 450:1214–1217, 2007.

[45] P. Del'Haye, O. Arcizet, A. Schliesser, R. Holzwarth, and T. J. Kippenberg. Full stabilization of a microresonator-based optical frequency comb. *Phys. Rev. Lett.*, 101:053903, 2008.

[46] A. A. Demidovich, A. S. Grabtchikov, V. A Orlovich, M. B Danailov, and W. Kiefer. Diode pumped diamond raman microchip laser. *Conf. Dig. Lasers and Electro-Optics Europe, (Optical Society of America, Washington DC)*, page 251, 2005.

[47] P. B. Deotare, I. Bulu, I. W. Frank, Q. Quan, Y. Zhang, R. Ilic, and M. Loncar. Broadband reconfiguration of optomechanical filters. *Nature Commun.*, 3:846, 2012.

[48] T. E. Derry, R. W. Fearick, and J. P. F. Sellschop. Ion channeling in natural diamond. minimum yields. *Phys. Rev. B*, 24 (7):3675, 1981.

[49] Martial Ducloy and Daniel Bloch. *Quantum Optics of Confined Systems*. Kluwer Academic Publishers, 1996.

[50] M. V. Gurudev Dutt, L. Childress, L. Jiang, E. Togan, J. Maze, F. Jelezko, A. S. Zibrov, P. R. Hemmer, and M. D. Lukin. Quantum register based on individual electronic and nuclear spin qubits in diamond. *Science*, 316:1312, 2007.

[51] T. W. Ebbesen, H. J. Lezec, H. F. Ghaemi, T. Thio, and P.A. Wolff. Extraordinary optical transmission through sub-wavelength hole arrays. *Nature*, 391:667, 1998.

[52] D. Englund, D. Fattal, E. Waks, G. Solomon, B. Zhang, T. Nakaoka Y. Arakawa, Y. Yamamoto, and J. Vuckovic. Controlling the spontaneous emission rate of single quantum dots in a two-dimensional photonic crystal. *Phys. Rev. Lett.*, 95: 013904, 2005.

[53] D. Englund, B. Shields, K. Rivoire, F. Hatami, J. Vuckovic, H. Park, and M. D. Lukin. Deterministic coupling of a single nitrogen vacancy center to a photonic crystal cavity. *Nano Lett.*, 10:3922, 2010.

[54] U. Fano. Effects of configuration interaction on intensities and phase shifts. *Phys. Rev. Lett.*, 124:1866, 1961.

[55] A. Faraon, P. E. Barclay, C. Santori, K.-M. C. Fu, and R. G. Beausoleil. Resonant enhancement of the zero-phonon emission

from a colour centre in a diamond cavity. *Nature Photon.*, 5: 301–305, 2011.

[56] A. Faraon, C. Santori, Z. Huang, V. M. Acosta, and R. G. Beausoleil. Coupling of nitrogen-vacancy centers to photonic crystal cavities in monocrystalline diamond. *Phys. Rev. Lett.*, 109:033604, 2012.

[57] J.-P. M. Feve, K. E. Shortoff, M. J. Bohn, and J. K. Brasseur. High average power diamond raman laser. *Opt. Exp.*, 19 (2):913, 2011.

[58] J. S. Foresi, P. R. Villeneuve, J. Ferrera, E. R. Thoen, G. Steinmeyer, S. Fan, J. D. Joannopoulos, L. C. Kimerling, Henry I. Smith, and E. P. Ippen. Photonic-bandgap microcavities in optical waveguides. *Nature*, 390:143, 1997.

[59] M. A. Foster, A. C. Turner, J. E. Sharping, B. S. Schmidt, M. Lipson, and A. L. Gaeta. Broad-band optical parametric gain on a silicon photonic chip. *Nature*, 441:960, 2006.

[60] M. A. Foster, J. S. Levy, O. Kuzucu, K. Saha, M. Lipson, and A. L. Gaeta. Silicon-based monolithic optical frequency comb source. *Opt. Exp.*, 19 (15):14233, 2011.

[61] I. Friedler, C. Sauvan, J. P. Hugonin, P. Lalanne, J. Claudon, and J. M. Gerard. Solid-state single photon sources: the nanowire antenna. *Opt. Exp.*, 17:2095, 2009.

[62] K.-M. C. Fu, C. Santori, P. E. Barclay, L. J. Rogers, N. B. Manson, and R. G. Beausoleil. Observation of the dynamic jahn-teller effect in the excited states of nitrogen-vacancy centers in diamond. *Phys. Rev. Lett.*, 330:60, 2009.

[63] G. D. Fuchs, V. V. Dobrovitski, D. M. Toyli, F. J. Heremans, C. D. Weis, T. Schenkel, and D. D. Awschalom. Excited-state spin coherence of a single nitrogen vacancy centre in diamond. *Nature Phys.*, 6:668, 2010.

[64] T. Gaebel, I. Popa, A. Gruber, M. Domhan, F. Jelezko, and J. Wrachtrup. Stable single-photon source in the near infrared. *New J. Phys.*, 6:98, 2004.

[65] M. Galli, S. L. Portalupi, M. Belotti, L. C. Andreani, L. O Faolain, and T. F. Krauss. Light scattering and fano resonances in high-q photonic crystal nanocavities. *Appl. Phy. Lett.*, 94:071101, 2009.

[66] A. Gonzalez-Tudela, D. Martin-Cano, E. Moreno, L. Martin-Moreno, C. Tejedor, and F. J. Garcia-Vidal. Entanglement of two qubits mediated by one-dimensional plasmonic waveguides. *Phys. Rev. Lett.*, 106:020501, 2011.

[67] M. L. Gorodetsky, A. D. Pryamikov, and V. S. Ilchenko. Rayleigh scattering in high-q microspheres. *J. Opt. Soc. Am. B.*, 17 (6):1051, 2000.

[68] M. S. Gorodetsky and V. S. Ilchenko. Thermal nonlinear effects in optical whispering-gallery microresonators. *Laser Phys. Rev.*, 2:1004, 1992.

[69] A. Gruber, A. Drabenstedt, C. Tietz, L. Fleury, J. Wrachtrup, and C. von Borczyskowski. Scanning confocal optical microscopy and magnetic resonance on single defect centers. *Science*, 276:2012, 1997.

[70] J. P. Hadden, J. P. Harrison, A. C. Stanley-Clarke, L. Marseglia, Y.-L. D. Ho, B. R. Patton, J. L. O Brien, and J. G. Rarity. Strongly enhanced photon collection from diamond defect centres under microfabricated integrated solid immersion lenses. *Appl. Phys. Lett.*, 97:241901, 2010.

[71] J. Hansryd, A. Andrekson, M. Westlund, J. Li, and P. Hedekvist. Fiber-based optical parametric amplifiers and their applications. *IEEE Select. Topics Quant. Electron.*, 8:506, 2002.

[72] B. J. M. Hausmann, M. Khan, T. Babinec, Y. Zhang, K. Martinick, M. McCutcheon, P. Hemmer, and M. Loncar. Fabrication of diamond nanowires for quantum information processing applications. *Diam. Relat. Mater.*, 19:621, 2010.

[73] B. J. M. Hausmann*, T. M. Babinec*, J. T. Choy*, J. S. Hodges, S. Hong, I. Bulu, A. Yacoby, M. Lukin, and M. Loncar.

Single-color centres implanted in diamond nanostructures. *New J. Phys.*, 13:045004, 2011.

[74] B. J. M. Hausmann, J.T. Choy, Q. Quan, M.W. McCutcheon, P. Maletinsky, T.M. Babinec, Y. Chu, A. Kubanek, A. Yacoby, M.D. Lukin, and M. Loncar. On-chip single crystal diamond resonators. In *CLEO/QELS 2011*, 2011.

[75] B. J. M. Hausmann, B. Shields, Q. Quan, J. T. Choy, M. W. McCutcheon, P. Maletinsky, T. M. Babinec, Y. Chu, A. Kubanek, A. Yacoby, M. D Lukin, and M. Loncar. A diamond quantum router of single photons at room temperature. In *MRS Fall meeting*, 2011.

[76] B. J. M. Hausmann, B. Shields Q. Quan, P. Maletinsky, M. McCutcheon, J. T. Choy, T. M. Babinec, A. Kubanek, A. Yacoby, M. D. Lukin, and M. Loncar. Integrated diamond networks for quantum nanophotonics. *Nano Lett.*, 12 (3):1578, 2012.

[77] B. J. M. Hausmann*, B. J. Shields*, Q. Quan, Y. Chu, N. P. de Leon, R. Evans, M. J. Burek, A. S. Zibrov, M. Markham, D. J. Twitchen, H. Park, M. D. Lukin, and M. Loncar. Coupling of nv centers to photonic crystal nanobeams in diamond. *Nano Lett.*, 13:5791, 2013.

[78] B. J. M. Hausmann, V. Venkataraman, I. Bulu, P. Deotare, and M. Loncar. Diamond nonlinear photonics. Accepted to Nature Photon., 2013.

[79] B.J.M. Hausmann, I. B. Bulu, P.B. Deotare, M.W. McCutcheon, V. Venkataraman, M.L. Markham, D.J. Twitchen, and M. Loncar. Integrated high quality factor optical resonators in diamond. *Nano Lett.*, 13 (5):1898, 2013.

[80] B.M. Hausmann, J.T. Choy, T. M. Babinec, B.J. Shields, I. Bulu, M.D. Lukin, and M. Loncar. Diamond nanophotonics and applications in quantum science and technology. *Phys. Status Sol. (a)*, 209:1619, 2012.

[81] T. Herr, K. Hartinger, J. Riemensberger, C. Y. Wang, E. Gavartin, R. Holzwarth, M. L. Gorodetsky, and T. J. Kippenberg. Universal formation dynamics and noise of kerr-frequency combs in microresonators. *Nature Photon.*, 8:480, 2012.

[82] M. P. Hiscocks, K. Ganesan, B. C. Gibson, S. T. Huntington, F. Ladouceur, and S. Prawer. Diamond waveguides fabricated by reactive ion etching. *Opt. Express*, 16 (24):19512–19519, 2009.

[83] A. Hoegele, C. Galland, M. Winger, and A. Imamoglu. Photon antibunching in the photoluminescence spectra of a single carbon nanotube. *Phys. Rev. Lett.*, 100:217401, 2008.

[84] E. S. Hosseini, S. Yegnanarayanan, A. H. Atabaki, M. Soltani, and A. Adibi. High quality planar silicon nitride microdisk resonators for integrated photonics in the visible wavelength range. *Opt. Exp.*, 17 (17):14543, 2009.

[85] A. Huck, S. Kumar, A. Shakoor, and U. L. Andersen. Controlled coupling of a single nitrogen-vacancy center to a silver nanowire. *Phys. Rev. Lett.*, 106:096801, 2011.

[86] J. Hwang, M. Pototschnig, R. Lettow, G. Zumofen, A. Renna, S. G tzinger, and V. Sandoghdar. A single-molecule optical transistor. *Nature*, 460:76–80, 2009.

[87] F. Jelezko and J. Wrachtrup. Single defect centres in diamond: A review. *Phys. Stat. Sol. (a)*, 203 (13):3207–3225, 2006.

[88] F. Jelezko, C. Tietz, A. Gruber, I. Popa, A. Nizovtsev, S. Kilin, and J. Wrachtrup. Spectroscopy of single n-v centers in diamond. *Single Mol.*, 2:255–260, 2001.

[89] F. Jelezko, I. Popa, A. Gruber, C. Tietz, J. Wrachtrup, A. Nizovtsev, and S. Kilin. Single spin states in a defect center resolved by optical spectroscopy. *Appl. Phys. Lett.*, 81 (12):2160, 2002.

[90] F. Jelezko, T. Gaebel, I. Popa, A. Gruber, and J. Wrachtrup. Observation of coherent oscillations in a single electron spin. *Phys. Rev. Lett.*, 92:076401, 2004.

[91] S. John. Strong localization of photons in certain disordered dielectric superlattices. *Phys. Rev. Lett.*, 58:2486, 1987.

[92] P. B. Johnson and R. W. Christy. Optical constants of the noble metals. *Phys. Rev. B*, 6:4370, 1972.

[93] H. J. Kimble. The quantum internet. *Nature*, 453:1023–1030, 2008.

[94] H. J. Kimble, M. Dagenais, and L. Mandel. Photon antibunching in resonance fluorescence. *Phys. Rev. Lett.*, 39:691, 1977.

[95] T. J. Kippenberg, S. M. Spillane, and K. J. Vahala. Modal coupling in traveling-wave resonators. *Opt. Lett.*, 27 (19):1669, 2002.

[96] T. J. Kippenberg, S. M. Spillane, and K. J. Vahala. Kerr-nonlinearity optical parametric oscillation in an ultrahigh-q toroid microcavity. *Phys. Rev. Lett.*, 93:083904, 2004.

[97] T. J. Kippenberg, R. Holzwarth, and S. A. Diddams. Microresonator-based optical frequency combs. *Science*, 332: 555, 2011.

[98] J. C. Knight, G. Cheung, F. Jacques, and T. A. Birks. Phase-matched excitation of whispering-gallery-mode resonances by a fiber taper. *Opt. Lett.*, 22 (15):1129, 1997.

[99] R. Kolesov, B. Grotz, G. Balasubramanian, R. J. St hr, A. A. L. Nicolet P. R. Hemmer, F. Jelezko, and J. Wrachtrup. Wave particle duality of single surface plasmon polaritons. *Nature Phys.*, 5:470–474, 2009.

[100] A. Ksendzov and Y. Lin. Integrated optics ring-resonator sensors for protein detection. *Opt. Exp.*, 30 (24):3344, 2005.

[101] C. Kurtsiefer, S. Mayer, P. Zarda, and H. Weinfurter. Stable solid-state source of single photons. *Phys. Rev. Lett.*, 85:290, 2000.

[102] F. Van Laere, G. Roelkens, M. Ayre, J. Schrauwen, D. Taillaert, D. Van Thourhout, T. F. Krauss, and R. Baets. Compact and highly efficient grating couplers between optical fiber and nanophotonic waveguides. *J. Lightwave Technol.*, 25 (1): 151–156, 2007.

[103] M. Larsson, K. N. Dinyari, and H. Wang. Composite optical microcavity of diamond nanopillar and silica microsphere. *Nano Lett.*, 9:1447, 2009.

[104] J. C. Lee, I. Aharonovich, P. Magyar A, F. Rol, and E. L. Hu. Coupling of silicon-vacancy centers to a single crystal diamond cavity. *Opt. Exp.*, 20 (8):8891, 2012.

[105] K. G. Lee, X. W. Chen, H. Eghlidi, P. Kukura, R. Lettow, A. Renn, V. Sandoghdar, and S. Goetzinger. A planar dielectric antenna for directional single-photon emission and near-unity collection efficiency. *Nature Photon.*, 5:166, 2011.

[106] S.Y. Lee, M. Widmann, T. Rendler, M. Doherty, T.M. Babinec, S. Yang, M. Eyer, P. Siyushev, B.M. Hausmann, M. Loncar, Z. Bodrog, A. Gali, N. Manson, H. Fedder, and J. Wrachtrup. Readout and control of a single nuclear spin with a meta-stable electron spin ancilla. *arXiv:1302.4608*, 2013.

[107] M. D. Levenson and N. Bloembergen. Dispersion of the nonlinear oyticai susceptibility tensor in centrosymmetric media. *Phys. Rev. B*, 10 (10):4447, 1974.

[108] J. S. Levy, A. Gondarenko, M. A. Foster, A. C. Turner-Foster, A. L. Gaeta, and M. Lipson. Cmos-compatible multiple-wavelength oscillator for on-chip optical interconnects. *Nature Photon.*, 4:37, 2009.

[109] H. J. Lezec, A. Degiron, E. Devaux, R. A. Linke, L. Martin-Moreno, F. J. Garcia-Vidal, and T. W. Ebbesen.

Beaming light from a subwavelength aperture. *Science*, 297 (5582):820, 2002.

[110] B.E. Little, J.S. Foresi, G. Steinmeyer, E.R. Thoen, S.T. Chu, H. Haus, E.P. Ippen, L.C. Kimerling, and W. Greene. Ultra-compact si-sio2 microring resonator optical channel dropping filters. *Photon. Technol. Lett. IEEE*, 10 (4):549, 1998.

[111] M. Loncar, T. M. Babinec, J. T. Choy, B. J. M. Hausmann, I. Bulu, Y. Zhang, M. Khan, and M. W. McCutcheon. Diamond nanophotonics and quantum optics. In *Artificial Atoms in Diamond: From Quantum Physics to Applications*, 2010.

[112] B. Lounis and W. E. Moerner. Single photons on demand from a single molecule at room temperature. *Nature*, 407:491, 2000.

[113] L.-W. Luo, G. S. Wiederhecker, J. Cardenas, C. Poitras, and M. Lipson. High quality factor etchless silicon photonic ring resonators. *Opt. Exp.*, 19 (7):6284, 2011.

[114] A. P. Magyar, J. C. Lee, A. M. Limarga, I. Aharonovich, F. Rol, D. R. Clarke, M. Huang, and E. L. Hu. Fabrication of thin, luminescent, single-crystal diamond membranes. *Appl. Phys. Lett.*, 99:081913, 2011.

[115] I. S. Maksymov, M. Besbes, J. P. Hugonin, J. Yang, A. Beveratos, I. Sagnes, I. Robert-Philip, and P. Lalanne. Metal-coated nanocylinder cavity for broadband nonclassical light emission. *Phys. Rev. Lett.*, 105:180502, 2010.

[116] P. Maletinsky, S. Hong, M.S. Grinolds, B. J. M. Hausmann, M.D.Lukin, R.-L. Walsworth, M. Loncar, and A. Yacoby. A robust, scanning quantum system for nanoscale sensing and imaging. *Nature Nanotech.*, 7:320, 2012.

[117] N. B. Manson, J. P. Harrison, and M. J. Sellars. Nitrogen-vacancy center in diamond: model of the electronic structure and associated dynamics. *Phys. Rev. B*, 74:104303, 2006.

[118] Park group Mark Polking. Correspondence 2013.

[119] A. V. Maslov and C. Z. Ning. Far-field emission of a semiconductor nanowire laser. *Opt. Lett.*, 29 (6):572–575, 2004.

[120] A. B. Matsko, A. A. Savchenkov, D. Strekalov, V. S. Ilchenko, and L. Maleki. Optical hyperparametric oscillations in a whispering-gallery-mode resonator: Threshold and phase diffusion. *Phys. Rev. A*, 71:033904, 2005.

[121] J. R. Maze, P. L. Stanwix, J. S. Hodges, S. Hong, J. M. Taylor, P. Cappellaro, L. Jiang, M. V. Gurudev Dutt, E. Togan, A. S. Zibrov, A. Yacoby, R. L. Walsworth, and M. D. Lukin. Nanoscale magnetic sensing with an individual electronic spin in diamond. *Nature*, 455:644, 2008.

[122] J. McKeever, A. Boca, A. D. Boozer, R. Miller, J. R. Buck, A. Kuzmich, and H. J. Kimble. Deterministic generation of single photons from one atom trapped in a cavity. *Science*, 303: 1992, 2004.

[123] J. Meijer, B. Burchard, M. Domhan, C. Wittmann, T. Gaebel, I. Popa, F. Jelezko, and J. Wrachtrup. Generation of single color centers by focused nitrogen implantation. *Appl. Phys. Lett.*, 87:261909, 2005.

[124] J. Meijer, S. Pezzagna, T. Vogel, B. Burchard, H.H. Bukow, I.W. Rangelow, Y. Sarov, H. Wiggers, I. Pluemel, F. Jelezko, J. Wrachtrup, F. Schmidt-Kaler, W. Schnitzler, and K. Singer. Towards the implanting of ion and positioning of nanoparticles with nm spatial resolution. *Appl. Phys. Lett.*, 91:567, 2008.

[125] R. P. Mildren, J. E. Butler, and J. R. Rabeau. Cvd-diamond external cavity raman laser at 573nm. *Opt. Express*, 16 (23): 18950, 2008.

[126] S. Mosor, J. Hendrickson, B. C. Richards, J. Sweet, G. Khitrova, H. M. Gibbs, T. Yoshie, A. Scherer, O. B. Shchekin, and D. G. Deppe. Scanning a photonic crystal slab nanocavity by condensation of xenon. *Appl. Phys. Lett.*, 87:142205, 2005.

[127] B. Naydenov, R. Kolesov, A. Batalov, J. Meijer, S. Pezzagna2, D. Rogalla, F. Jelezko, and J. Wrachtrup. Engineering single

photon emitters by ion implantation in diamond. *Appl. Phys. Lett.*, 95:181109, 2009.

[128] C. Nebel and J. Ristein. *Semiconductors and Semimetals: Thin-Film Diamond I.* Elsevier Academic Press, 2004.

[129] P. Neumann, N. Mizuochi, F. Rempp, P. Hemmer, H. Watanabe, S. Yamasaki, V. Jacques, T. Gaebel, F. Jelezko, and J. Wrachtrup. Multipartite entanglement among single spins in diamond. *Science*, 320:1326, 2008.

[130] P. Neumann, J. Beck, M. Steiner, F. Rempp, H. Fedder, P. R. Hemmer, J. Wrachtrup, and F. Jelezko. Single-shot readout of a single nuclear spin. *Science*, 329:542, 2010.

[131] P. Neumann, R. Kolesov, B. Naydenov, J. Beck, F. Rempp, M. Steiner, V. Jacques, G. Balasubramanian, M. L. Markham, D. J. Twitchen, S. Pezzagna, J. Meijer, J. Twamley, F. Jelezko, and J. Wrachtrup. Quantum register based on coupled electron spins in a room-temperature solid. *Nature Phys.*, 6:249, 2010.

[132] J. L. O'Brien. Optical quantum computing. *Science*, 318:1567, 2007.

[133] Y. Okawachi, K. Saha, J. S. Levy, Y. H. Wen, M. Lipson, and A. L. Gaeta. Octave-spanning frequency comb generation in a silicon nitride chip. *Opt. Lett.*, 36 (17):3398, 2011.

[134] P. Olivero, S. Rubanov, P. Reichart, B. C. Gibson, S. T. Huntington, J. Rabeau, A. D. Greentree, J. Salzman, D. Moore, D. N. Jamieson, and S. Prawer. Ion-beam-assisted lift-off technique for three-dimensional micromachining of freestanding single-crystal diamond. *Adv. Mater.*, 17:2427–2430, 2005.

[135] N. R. Parikh, J. D. Hunn E. McGucken, M. L. Swanson, C. W. White, R. A. Rudder, D. P. Malta, J. B. Posthill, and R. J. Markunas. Single crystal diamond plate liftoff achieved by ion implantation and subsequent annealing. *Appl. Phys. Lett.*, 61: 3124, 1992.

[136] Y.-S. Park, A. K. Cook, and H. Wang. Cavity qed with diamond nanocrystals and silica microspheres. *Nano Lett.*, 6:2075, 2006.

[137] W. Pfaff, T. H. Taminiau, L. Robledo, H. Bernien, M. L. Markham, D. J. Twitchen, and R. Hanson. Demonstration of entanglement-by-measurement of solid state qubits. *arXiv:1206.2031v1*, 2012.

[138] S. Prawer and A. D. Greentree. Diamond for quantum computing. *Science*, 320:1601, 2008.

[139] K. Preston, B. Schmidt, and M. Lipson. Polysilicon photonic resonators for large-scale 3d integration of optical networks. *Opt. Exp.*, 15 (25):17283, 2007.

[140] E. M. Purcell. Spontaneous emission probabilities at radio frequencies. *Phys. Rev.*, 69:681, 1946.

[141] Q. Quan and M. Loncar. Deterministic design of wavelength scale, ultra-high q photonic crystal nanobeam cavities. *Opt. Exp.*, 19 (19):18529, 2011.

[142] Q. Quan, P.B. Deotare, and M. Loncar. Photonic crystal nanobeam cavity strongly coupled to the feeding waveguide. *Appl. Phys. Lett.*, 96:203102, 2010.

[143] J. R. Rabeau, P. Reichert, G. Tamanyan, D. N. Jamieson, S. Prawer, F. Jelezko, T. Gaebel, I. Popa, M. Domhan, and J. Wrachtrup. Implantation of labelled single nitrogen vacancy centers in diamond using 15n. *Appl. Phys. Lett.*, 88:023113, 2006.

[144] L. Razzari, D. Duchesne, M. Ferrera, R. Morandotti, S. Chu, B. E. Little, and D. J. Moss. Cmos-compatible integrated optical hyper-parametric oscillator. *Nature Photon.*, 4:41, 2009.

[145] J. P. Reithmaier, G. Sek, A. Loeffler, C. Hofmann, S. Kuhn, S. Reitzenstein, L. V. Keldysh, V. D. Kulakovskii, T. L. Reinecke, and A. Forchel. Strong coupling in a single quantum dot semiconductor microcavity system. *Nature*, 432:197, 2004.

[146] J. Riedrich-Moeller, L. Kipfstuhl, C. Hepp, E. Neu, C. Pauly, F. Muecklich, A. Baur andM. Wandt, S. Wolff, M. Fischer, S. Gsell, M. Schreck, and C. Becher. One- and two-dimensional

photonic crystal microcavities in single crystal diamond. *Nature Nanotech.*, 7:69, 2012.

[147] H. Rigneault, J. Capoulade, J. Dintinger, J. Wenger, N. Bonod, E. Popov, T. W. Ebbesen, and P.-F. Lenne. Enhancement of single-molecule fluorescence detection in subwavelength apertures. *Phys. Rev. Lett.*, 95:117401, 2005.

[148] L. Robledo*, L. Childress*, H. Bernien, B. Hensen, P. F. A. Alkemade, and R. Hanson. High-fidelity projective read-out of a solid-state spin quantum register. *Nature*, 477:574, 2011.

[149] H. Rong, R. Jones, A. Liu, O. Cohen, D. Hak, A. Fang, and M. A. Paniccia. A continuous-wave raman silicon laser. *Nature*, 433:725, 2005.

[150] H. Rong, S. Xu, Y.-H. Kuo, V. Sih, O. Cohen, O. Raday, and M. Paniccia. Low-threshold continuous-wave raman silicon laser. *Nature Photon.*, 1:232, 2007.

[151] D. Le Sage, L. M. Pham, N. Bar-Gill, C. Belthangady, M. D. Lukin, A. Yacoby, and R. L. Walsworth. Efficient photon detection from color centers in a diamond optical waveguide. *Phys. Rev. B*, 85:121202(R), 2012.

[152] C. Santori, P. E. Barclay, K.-M. C. Fu, R. G. Beausoleil, S. Spillane, and M. Fisch. Nanophotonics for quantum optics using nitrogen-vacancy centers in diamond. *Nanotechnology*, 21 (27):274008, 2010.

[153] A. A. Savchenkov, A. B. Matsko, W. Liang, V. S. Ilchenko, D. Seidel, and L. Maleki. Kerr combs with selectable central frequency. *Nature Photon.*, 5:293, 2011.

[154] A. W. Schell, G. Kewes, T. Hanke, A. Leitenstorfer, R. Bratschitsch, O. Benson, and T. Aichele. Single defect centers in diamond nanocrystals as quantum probes for plasmonic nanostructures. *Opt. Exp.*, 19 (8):7914, 2011.

[155] S. Schietinger, M. Barth, T. Aichele, and O. Benson. Plasmon enhanced single photon emission from a nanoassebled

metal-diamond hybrid structure at room temperature. *Nano Lett.*, 9 (4):1694–1698, 2009.

[156] T. Schr der, F. G deke, M. J. Banholzer, and O. Benson. Ultrabright and efficient single-photon generation based on nitrogen-vacancy centres in nanodiamonds on a solid immersion lens. *New J. Phys.*, 13:055017, 2011.

[157] O. Schwelb. Transmission, group delay, and dispersion in single-ring optical resonators and add/drop filters - a tutorial overview. *J. Lightwave Technol.*, 22 (5):1380, 2004.

[158] R. Shankar, I. Bulu, R. Leijssen, and M. Loncar. Study of thermally-induced optical bistability and the role of surface treatments in si-based mid-infrared photonic crystal cavities. *Opt. Exp.*, 19 (24):24828, 2011.

[159] T. Shoji, T. Tsuchizawa, T. Watanabe, K. Yamada, and H. Morita. Low loss mode size converter from 0.3pm square si wire waveguides to singlemode fibres. *Electron. Lett.*, 38 (25): 1669–1670, 2002.

[160] P. Siyushev, F. Kaiser, V. Jacques, I. Gerhardt, S. Bischof, H. Fedder, J. Dodson, M. Markham, D. Twitchen, F. Jelezko, and J. Wrachtrup. Monolithic diamond optics for single photon detection. *Appl. Phys. Lett.*, 97:241902, 2010.

[161] P. Siyushev, H. Pinto, A. Gali, F. Jelezko, and J. Wrachtrup. Low temperature studies of charge dynamics of nitrogen-vacancy defect in diamond. *arXiv:1204.4898*, 2012.

[162] H. Soda, K. Iga, C. Kitahara, and Y. Suematsu. Gainasp/inp surface emitting injection lasers. *Jpn. J. Appl. Phys.*, 18:2329, 1979.

[163] S. M. Spillane, T. J. Kippenberg, and K. J. Vahala. Ultralow-threshold raman laser using a spherical dielectric microcavity. *Nature*, 415:621, 2002.

[164] K. Srinivasan, P. E. Barclay, M. Borselli, and O. Painter. Optical-fiber-based measurement of an ultrasmall volume high-q photonic crystal microcavity. *Phys. Rev. B*, 70:081306, 2004.

[165] M.-C. Tien, J. F. Bauters, M. J. R. Heck, D. T. Spencer, D. J. Blumenthal, and J. E. Bowers. Ultra-high quality factor planar si3n4 ring resonators on si substrates. *Opt. Exp*, 19 (14):13551, 2011.

[166] E. Togan, Y. Chu, A. S. Trifonov, L. Jiang, J. Maze, L. Childress, M. V. G. Dutt, A. S. S rensen, P. R. Hemmer, A. S. Zibrov, and M. D. Lukin. Quantum entanglement between an optical photon and a solid-state spin qubit. *Nature*, 466: 730–734, 2010.

[167] D. M. Toyli, C. D. Weis, G. D. Fuchs, T. Schenkel, and D. D. Awschalom. Chip-scale nanofabrication of single spins and spin arrays in diamond. *Nano Lett.*, 10:3168, 2010.

[168] A. C. Turner, M. A. Foster, A. L. Gaeta, and M. Lipson. Ultra-low power parametric frequency conversion in a silicon microring resonator. *Opt. Exp.*, 16 (7):4881, 2008.

[169] D. J. Twitchen, M. E. Newton, J. M. Baker, T. R. Anthony, and W. F. Banholzer. Electron-paramagnetic-resonance measurements on the divacancy defect center r4/w6 in diamond. *Phys. Rev. B*, 59 (20):900, 1999.

[170] T. Udem, R. Holzwarth, and T. W. H nsch. Optical frequency metrology. *Nature*, 416:233, 2002.

[171] T. van der Sar, J. Hagemeier, W. Pfaff, E. C. Heeres, S. M. Thon, H. Kim, P. M. Petroff, T. H. Oosterkamp, D. Bouwmeester, and R. Hanson. Deterministic nanoassembly of a coupled quantum emitter photonic crystal cavity system. *Appl. Phys. Lett.*, 98:193103, 2011.

[172] J. Vuckovic and Y. Yamamoto. Photonic crystal microcavities for cavity quantum electrodynamics with a single quantum dot. *Appl. Phys. Lett.*, 82(15):2374, 2003.

[173] C. Wang, C. Kurtsiefer, H. Weinfurter, and B. Burchard. Single photon emission from siv centres in diamond produced by ion implantation. *J. Phys. B: At. Mol. Opt. Phys.*, 39:37, 2006.

[174] C. Wang, C. Kurtsiefer, H. Weinfurtner, and B. Burchard. Single photon emission from siv centers in diamond produced by ion implantation. *J. Phys. B: At. Mol. Opt. Phys.*, 39:37, 2006.

[175] C. F. Wang and E. L. Hu. Fabrication of suspended single crystal diamond devices by electrochemical etch. *J. Vac. Sci. Technol. B*, 25 (3):730–733, 2007.

[176] C. F. Wang, Y-S. Choi, J. C. Lee, E. L. Hu, J. Yang, and J. E. Butler. Observation of whispering gallery modes in nanocrystalline diamond microdisks. *Appl. Phy. Lett.*, 90: 081110, 2007.

[177] C. F. Wang, R. Hanson, D. D. Awschalom, and E. L. Hu. Fabrication and characterization of two-dimensional photonic crystal microcavities in nanocrystalline diamond. *Appl. Phy. Lett.*, 91:201112, 2007.

[178] J. R. Weber, W. F. Koehl, J. B. Varley, A. Janotti, B. B. Buckley, C. G. Van de Walle, and D. D. Awschalom. Quantum computing with defects. *Proc. Natl. Acad. Sci.*, 107:8513, 2010.

[179] R.G. Wilson. Depth distributions and range parameters for elements implanted into single-crystal diamonds and chemically vapor-deposited polycrystal diamond films. *Sur. Coat. Technol.*, 47 (1-3):559, 1991.

[180] J. Wolters, N. Sadzak, A. W. Schell, T. Schroeder, and O. Benson. Ultrafast spectral diffusion measurement on nitrogen vacancy centers in nanodiamonds using correlation interferometry. *arXiv:1206.0852v1*, 2012.

[181] J. Wrachtrup and F. Jelezko. Processing quantum information in diamond. *J. Phys.: Condens. Matter*, 18:807–824, 2006.

[182] Q. Xu, B. Schmidt, S. Pradhan, and M. Lipson. Micrometre-scale silicon electro-optic modulator. *Nature*, 435: 325, 2005.

[183] E. Yablonovitch. Inhibited spontaneous emission in solid-state physics and electronics. *Phys. Rev. Lett.*, 58 (20):2059, 1987.

[184] A. Yariv and P. Yeh. *Photonics*. Oxford University Press, 2007.

[185] T. Yoshie, A. Scherer, Hendrickson, G. Khitrova, H. M. Gibbs, G. Rupper, C. Ell, O. B. Shchekin, and D. G. Deppe. Vacuum rabi splitting with a single quantum dot in a photonic crystal nanocavity. *Nature*, 432:200, 2004.

[186] A. M. Zaitsev. *Optical Properties of Diamond: A Data Handbook*. Springer-Verlag, 2001.

[187] X.W. Zhang, H.-G. Boyen, P. Ziemann, M. Ozawa, F. Banhart, and M. Schreck. Growth mechanism for epitaxial cubic boron nitride films on diamond substrates by ion beam assisted deposition. *Diam. Relat. Mater.*, 13 (4-8):1144, 2004.

[188] Y. Zhang and M. Loncar. Ultra-high quality factor optical resonators based on semiconductor nanowires. *Opt. Express*, 16: 17400, 2008.

[189] M. Zhi, X. Wang, and A. V. Sokolov. Broadband coherent light generation in diamond driven by femtosecond pulses. *Opt. Exp.*, 16 (16):12139, 2008.

Colophon

This thesis was typeset using LaTeX, originally developed by Leslie Lamport and based on Donald Knuth's TeX. The body text is set in 11 point Arno Pro, designed by Robert Slimbach in the style of book types from the Aldine Press in Venice, and issued by Adobe in 2007. A template, which can be used to format a PhD thesis with this look and feel, has been released under the permissive MIT (X11) license, and can be found online at github.com/suchow/ or from the author at suchow@post.harvard.edu.